

# 000 001 002 003 004 005 006 007 008 009 010 011 012 013 014 015 016 017 018 019 020 021 022 023 024 025 026 027 028 029 030 031 032 033 034 035 036 037 038 039 040 041 042 043 044 045 046 047 048 049 050 051 052 053 MULTIHEAD MIXTURE OF EXPERTS FOR CLASSIFICATION OF GIGAPIXEL PATHOLOGY IMAGES

Anonymous authors

Paper under double-blind review

## ABSTRACT

Multiple Instance Learning (MIL) is the predominant paradigm for classifying gigapixel whole-slide images in computational pathology. MIL follows a sequence of 1) extracting patch features, 2) applying a linear layer to obtain task-specific patch features, and 3) aggregating the patches into a slide feature for classification. While substantial efforts have been devoted to optimizing patch feature extraction and aggregation, none have yet addressed the second point, the critical layer which transforms general-purpose features into task-specific features. We hypothesize that this layer constitutes an overlooked performance bottleneck and that stronger representations can be achieved with a low-rank transformation tailored to each patch’s phenotype, yielding synergistic effects with existing MIL approaches. To this end, we introduce MAMMOTH, a parameter-efficient, multi-head mixture of experts module designed to improve the performance of any MIL model with minimal alterations to the total number of parameters. Across 8 MIL methods and 19 different tasks, we find that this improvement to the task-specific transformation [yields higher performance gains than changing to the most effective aggregator](#). Additionally, we identify Instance-Gradient Interference (IGI)—a limitation where heterogeneous instances produce conflicting gradients when processed by a single linear layer—and show that MAMMOTH effectively mitigates IGI by decoupling gradient flows between experts, yielding consistent performance gains in [130 of the 152 examined configurations](#).

## 1 INTRODUCTION

The technical advancements in computational pathology (CPath) have significantly transformed analysis of whole-slide images (WSIs), enabling machine learning models to achieve pathologist-level precision in diverse clinical tasks (Song et al., 2023; Bejnordi et al., 2017; Campanella et al., 2019; Bulten et al., 2022). However, unique challenges arise when analyzing gigapixel WSIs due to their immense size and morphological heterogeneity that spans diverse tissue structures, cellular formations, and spatially distributed pathological characteristics (Saltz et al., 2018; Abdul Jabbar et al., 2020; Marusyk & Polyak, 2010). In this context, multiple instance learning (MIL) frameworks have emerged as the cornerstone approach to distill gigapixel images into condensed slide-level representations for accurate downstream performance (Chen et al., 2024b; Lu et al., 2021; Shao et al., 2021; Wagner et al., 2023; Li et al., 2021). The MIL framework consists of three stages: 1) Dividing a WSI into a set of smaller image patches, which are encoded into general-purpose features with a patch feature encoder, 2) transforming the *general-purpose* features into *task-specific* features with a linear layer, and 3) aggregating the feature set into a slide-level representation. The first and last stages have been studied substantially, through histopathology foundation models that produce features encompassing diverse histomorphological concepts (Wang et al., 2022; Xu et al., 2024; Chen et al., 2024a; Wang et al., 2024; Lu et al., 2024a) and aggregation architectures that yield task-optimized slide representations (Ilse et al., 2018; Lu et al., 2021; Shao et al., 2021; Campanella et al., 2024).

However, the critical intermediate step of encoding task-specific patch features remains unexplored. Most MIL models obtain task-specific representation by applying the same linear layer to all patch embeddings, regardless of their morphological content. We hypothesize that applying a single transformation to all patches limits the model’s ability to capture diverse morphological features, ultimately reducing the quality of slide-level predictions. In breast cancer lesion subtyping, for example, diverse concepts such as epithelial cell morphology, spatial arrangement, and stromal layer

054 architectures are collectively important factors for diagnosis (Brancati et al., 2021). This diversity  
 055 suggests that the task-specific transformation would ideally separate patch embeddings into clusters  
 056 corresponding to distinct morphological concepts; while in practice, the output of the linear  
 057 layer forms a relatively continuous embedding space (**Fig. 1A**). As a result, MIL aggregation may  
 058 struggle to distinguish between the array of morphological concepts necessary for a comprehensive  
 059 slide-level representation.

060 These insights warrant a more flexible archi-  
 061 tecture that can adapt its transformations based  
 062 on the morphological content of each patch.  
 063 Mixture of experts (Jacobs et al., 1991; Jor-  
 064 dan & Jacobs, 1994; Eigen et al., 2013) (MoE)  
 065 presents a promising solution by maintaining a  
 066 collection of specialized linear layers, known  
 067 as *experts*, each optimized to process a differ-  
 068 ent morphological pattern. A dynamic routing  
 069 mechanism directs each patch to the most ap-  
 070 propriate expert, enabling more nuanced fea-  
 071 ture transformations than those of a single lin-  
 072 ear layer (Eigen et al., 2013; Shazeer et al.,  
 073 2017; Cai et al., 2024). However, a critical  
 074 challenge of MoE is training instability: the  
 075 hard assignments of experts to inputs lead to  
 076 poor gradient flow, leading to imbalanced ex-  
 077 pert utilization, with certain experts receiving  
 078 most inputs (Cai et al., 2024). Learning an  
 079 effective hard assignment is particularly chal-  
 080 lenging in CPath due to the massive number of  
 081 patch features ( $\approx 10,000$  per sample) and the  
 082 small number of training samples ( $< 1,000$  pa-  
 083 tients) compared to traditional MoE tasks. MIL  
 084 models also frequently suffer from poor generalizability: adding more experts can exacerbate these  
 085 problems, increasing the risk of overfitting due to the expanded parameter count (Shao et al., 2025).

086 To address these challenges, we propose MAMMOTH, a MoE module that replaces the task-specific  
 087 linear layer for learning specialized patch feature transformations. MAMMOTH is a plug-and-play  
 088 module that can be integrated into any MIL model to improve downstream performance (**Fig. 1B**),  
 089 operating with the same parameter budget as the linear layer. Instead of hard expert assignments that  
 090 lead to training instability, MAMMOTH leverages soft expert assignment where each expert processes  
 091 a different linear combination of all patch embeddings, improving gradient flow and expert utiliza-  
 092 tion (Puigcerver et al., 2024; Liu et al., 2024). Building on this foundation, MAMMOTH introduces  
 093 several model designs uniquely suited to addressing the challenges of CPath slide classification.  
 094 First, we partition each patch embedding into multiple embedding heads, with each smaller em-  
 095 bedding processed in parallel by different MoE heads. This multihead approach not only provides  
 096 fine-grained control over the patch embedding subspace but also handles larger patch embedding  
 097 size ( $> 1,024$ ) compared to that of typical input token in natural images (196 or 256). Next, we em-  
 098 ploy low-rank decomposition in expert layers and weight sharing for parameter efficiency, enabling  
 099 MAMMOTH to replace the original linear layer without altering the model size. Finally, MAMMOTH  
 100 produces a compact set of output embeddings from the large input patch embedding set ( $> 25 \times$   
 101 reduction). This distills the large, noisy input set to a compact set of representative morphological  
 102 aggregates, akin to prototype-based aggregation (Vu et al., 2023; Song et al., 2024a;b).

103 Our work demonstrates that applying multiple small, specialized transformations to each patch em-  
 104 bedding via MAMMOTH substantially outperforms the conventional approach of using a single,  
 105 larger transformation for all patch embeddings (**Fig. 1B**). Our key contributions are as follows:

- 106 • We propose MAMMOTH, a general-purpose MoE layer designed for gigapixel WSI classi-  
 107 fication that can be easily integrated into any MIL framework.

- 108 • We identify the task-specific linear layer as a critical performance bottleneck, showing  
109 that MAMMOTH improves performance in 130 out of the 152 examined configurations and  
110 allows simple MIL methods to outperform sophisticated MIL methods at baseline.
- 111 • Interpretability analyses confirm that MAMMOTH experts learn to specialize in distinct  
112 morphological concepts.
- 113 • Extensive ablations reveal that MAMMOTH surpasses other MoE adaptations in CPath.

## 115 2 RELATED WORKS

117 **Mixture of Experts (MoE):** MoE processes the input with *experts*, each tailored to different input  
118 spaces, resulting in embeddings that generalize across diverse tasks. While Sparse MoE, which per-  
119 forms hard assignment of inputs to experts (Cai et al., 2024; Shazeer et al., 2017), is popular due  
120 to favorable model size scaling and handling of token heterogeneity (Cai et al., 2024), it often suf-  
121 fers from representation collapse (Chi et al., 2022) and under-utilization of experts (Shazeer et al.,  
122 2017; Lepikhin et al., 2020). Among efforts to balance expert utilization (Fedus et al., 2022; Du  
123 et al., 2022; Riquelme et al., 2021), Soft MoE stands out by providing a differentiable gating mech-  
124 anism that routes weighted combinations of inputs across multiple experts (Puigcerver et al., 2024).  
125 Consequently, each input receives contributions from several experts, leading to stable training dy-  
126 namics (Liu et al., 2024; Puigcerver et al., 2024). Another approach is sparse multihead MoE (Wu  
127 et al., 2024a) that enables more granular expert specialization, by distributing partitioned inputs to  
128 multi-head experts.

129 Despite its success in improving classification performance for small images ( $256 \times 256$  pixels),  
130 the suitability of MoE for the challenging tasks of classifying gigapixel WSIs in CPath remains  
131 unclear. To this end, MAMMOTH builds on the foundations of Soft and multihead MoE to achieve  
132 morphological specialization for slide-level classification tasks.

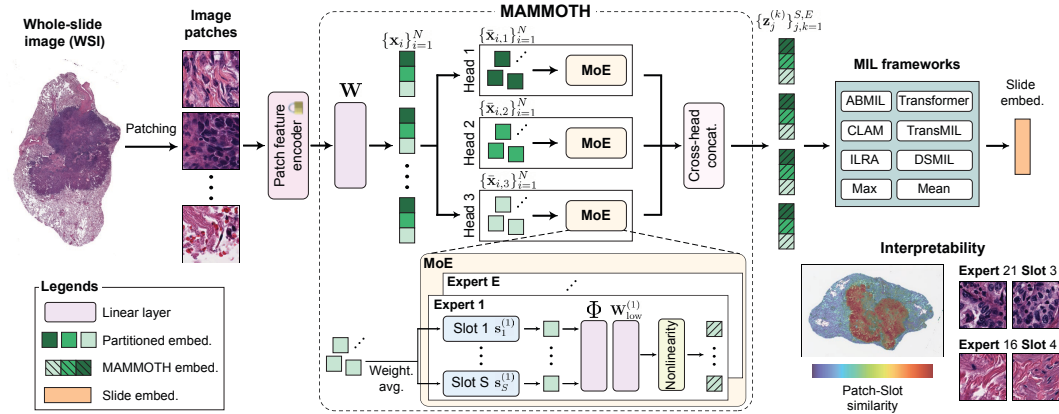
133 **Parameter-efficient MoE:** Increasing the number of experts or heads for MoE can lead to substan-  
134 tial growth in model size, and ultimately model overfitting (Cai et al., 2024). Recent works have  
135 explored lightweight experts by leveraging low-rank adaptors (Zadouri, 2024; Wu et al., 2024b),  
136 smaller experts (He, 2024), or matrix factorization (Oldfield et al., 2024; Gao et al., 2022) to re-  
137 duce parameter count while preserving representational quality. Specifically, matrix factorization  
138 decomposes the expert layer weights into a series of low-rank matrices, enabling models to scale  
139 the number of experts without substantially increasing the parameters (Wu et al., 2024b). Weight  
140 sharing across experts also offers efficiency by reusing weight matrices between experts (Tan et al.,  
141 2023; Wu et al., 2024b; Jawahar et al., 2024). MAMMOTH combines these ideas to enable a larger  
142 number of experts within the same parameter budget as the linear layer it replaces.

143 **MoE for computational pathology:** Despite the popularity of MoE in machine learning literature,  
144 it remains relatively unexplored for computational pathology. Existing works either use a mixture  
145 of attention-based MIL experts to perform multitask mutation prediction (Li et al., 2024) with each  
146 expert corresponding to a single task, or train separate CNNs to detect tissue artifacts and weigh  
147 each model’s prediction through the MoE formulation (Kanwal et al., 2024). However, these are  
148 highly tailored to specific tasks, and are not readily extensible to a large suite of MIL models.  
149 Recently, a pathology-aware sparse routing mechanism (PaMOE) was proposed to use pre-extracted  
150 patch prototypes to encourage experts to specialize in different pathologic contents, replacing the  
151 feedforward layers in the transformer encoder block with a standard sparse MoE (Wu et al., 2025).  
152 In contrast, MAMMOTH is a highly flexible plug-and-play MoE module built to replace the initial  
153 linear layer that universally exists in MIL frameworks (Ilse et al., 2018; Campanella et al., 2024).

154 **Pre-aggregation modules:** Recent works have explored two primary avenues for processing patch-  
155 level features prior to the aggregation layer. The first approach samples a subset of patch features  
156 for subsequent aggregation based on certain criteria (Neidlinger et al., 2025; Zhu et al., 2025), as a  
157 means of regularization or inference-time efficiency. The second approach introduces an additional  
158 module to re-embed these patch features in a spatially-aware manner, either with a regional Trans-  
159 former which is trained along with the aggregation module to produce task-optimized features (Tang  
160 et al., 2024), or by performing local self-attention among collections of neighboring patches (Guo  
161 et al., 2025). Unique to these approaches, MAMMOTH fuses global information based on feature  
162 similarity rather than spatial proximity, while also performing MoE-based processing without re-  
163 quiring increased parameter counts.

### 162 3 METHODS

164 We present MAMMOTH, a **M**atrix-factorized **M**ixture of **M**ultihead Experts for learning task-  
 165 specific WSI patch representations in CPath. MAMMOTH can easily replace the standard linear  
 166 layer of any MIL architecture with a mixture of small, specialized experts, leading to improved  
 167 downstream performance with the same parameter count (**Fig. 2**).  
 168



183 **Figure 2: MAMMOTH architecture** MAMMOTH replaces the initial linear layer of MIL models,  
 184 transforming generic patch features into task-optimized features with a multiheaded soft MoE.  
 185 Patch features are routed to different combinations of slots and experts for task- and morphology-specific  
 186 processing. The MoE outputs are concatenated and fed into the MIL model.

187 To obtain a set of embeddings for MIL, each WSI is divided into  $256 \times 256$  pixel patches, each  
 188 of which is encoded into an embedding ( $\approx 1,024$  dim) by a pretrained histopathology patch feature  
 189 encoder (Campanella et al., 2024). This results in a set of patch embeddings  $\mathbf{X} = \{\mathbf{x}_i\}_{i=1}^N$ ,  $\mathbf{x}_i \in \mathbb{R}^D$   
 190 for  $N$  patches of a given WSI ( $N \approx 10,000$ ). A standard MIL framework,  $f_{\text{MIL}}(\cdot)$ , which converts  
 191  $\mathbf{X}$  into the slide-level embedding  $\mathbf{x}_{\text{WSI}} \in \mathbb{R}^{D'}$ , can be decomposed into the aggregator  $f_{\text{MIL}}^{\text{agg.}}$  and the  
 192 linear layer  $f_{\text{MIL}}^{\text{linear}}$ ,

$$\mathbf{x}_{\text{WSI}} = f_{\text{MIL}}(\{\mathbf{x}_i\}_{i=1}^N) = f_{\text{MIL}}^{\text{agg.}}(\{f_{\text{MIL}}^{\text{linear}}(\mathbf{x}_i)\}_{i=1}^N). \quad (1)$$

194 MAMMOTH replaces  $f_{\text{MIL}}^{\text{linear}}(\cdot)$  with following operations: (1) input partitioning into multiple  
 195 segments (**Section 3.1**), (2) a slot-based pooling module based on a set of patch prototypes  
 196 (**Section 3.2**), (3) a low-rank projection with matrix factorization (**Section 3.3**), and (4) concatenation  
 197 of processed partitions to form output (**Section 3.4**).  
 198

#### 199 3.1 MULTI-HEAD PROCESSING OF INPUT EMBEDDINGS

201 To enhance the expressivity of the input patch embeddings, we employ multi-head processing, where  
 202 each head accounts for a different partition of the embedding. Specifically, each head consists of  
 203 a MoE architecture comprised of  $E$  experts, each with  $S$  slots. After applying linear layer  $\mathbf{W} \in$   
 204  $\mathbb{R}^{(P \cdot H) \times D}$  to reduce the size of the embedding, it is divided into  $H$  non-overlapping partitions, with  
 205 the  $h^{\text{th}}$  head processing the  $h^{\text{th}}$  partition. The  $h^{\text{th}}$  partition  $\bar{\mathbf{x}}_{i,h}$  is given as

$$\bar{\mathbf{x}}_{i,h} = (\mathbf{W}\mathbf{x}_i)[(h-1)P+1:hP] \in \mathbb{R}^P. \quad (2)$$

207 Each set of partitioned embeddings  $\{\bar{\mathbf{x}}_{i,h}\}_{i=1}^N$  is independently processed by a distinct MoE, prior  
 208 to the head-level concatenation at the last stage. For notational decluttering, we drop the subscript  $h$   
 209 for **Sections 3.2** and **3.3**, noting that the same operations are performed on all heads. This is different  
 210 from Multihead MoE (Wu et al., 2024a), which flattens the partitioned embeddings into a larger set  
 211 of  $N \cdot H$  embeddings and processes them with a shared pool of experts.

#### 212 3.2 SLOT-BASED POOLING

213 We apply slot-based pooling to obtain linear combinations of  $\{\bar{\mathbf{x}}_i\}_{i=1}^N$ , with each slot representing  
 214 a unique morphological concept. For a given expert  $k$ , we pool the embeddings  $\{\bar{\mathbf{x}}_i\}_{i=1}^N$  to  $S$  slots

via weighted averaging, based on the similarity of each input embedding to slot-specific trainable and randomly initialized prototypes  $\{\mathbf{s}_j^{(k)}\}_{j=1}^S$  with  $\mathbf{s}_j^{(k)} \in \mathbb{R}^P$ . The similarity score of an input embedding with each prototype is computed with the inner product, normalized with a softmax operation across  $N$  embeddings. The score  $\alpha_{j,i}^{(k)}$  represents the similarity of the  $i^{\text{th}}$  embedding to slot  $j$  of expert  $k$ , and is used to compute the slot embedding  $\mathbf{u}_j^{(k)} \in \mathbb{R}^P$ ,

$$\alpha_{j,i}^{(k)} = \frac{\exp(\langle \bar{\mathbf{x}}_i, \mathbf{s}_j^{(k)} \rangle)}{\sum_{i'=1}^N \exp(\langle \bar{\mathbf{x}}_{i'}, \mathbf{s}_j^{(k)} \rangle)}, \quad \mathbf{u}_j^{(k)} = \sum_{i=1}^N \alpha_{j,i}^{(k)} \cdot \bar{\mathbf{x}}_i, \quad (3)$$

where  $\langle \cdot, \cdot \rangle$  denotes the inner product and  $\mathbf{u}_j^{(k)}$  is computed as the average of input embeddings weighted by the similarity scores. The non-zero score  $\alpha_{j,i}^{(k)}$  forms the basis of soft expert assignment, by allowing all patch embeddings to contribute to every slot and consequently to every expert. In this context, each weighted average can be interpreted as a summary of a distinct histomorphological feature in the WSI, as demonstrated in **Figures 3** and **A3-A7**.

### 3.3 LOW-RANK EXPERTS

With each slot aggregating a distinct morphological concept, we introduce experts to perform feature transformations tailored to each slot. For each expert, MoE typically uses an MLP to process the slot embedding,  $\mathbf{z}_j^{(k)} = \text{LayerNorm}(\text{ReLU}(\mathbf{W}_{\text{full}}^{(k)} \mathbf{u}_j^{(k)}))$ , where  $\mathbf{W}_{\text{full}}^{(k)} \in \mathbb{R}^{(D'/H) \times P}$  represent the linear transformations and the ReLU and layer normalization represent additional nonlinearity.

The dense matrix  $\mathbf{W}_{\text{full}}^{(k)}$ , however, presents a scaling challenge as the parameter count increases proportionally with the number of experts. To alleviate this undesirable scaling property, we approximate  $\mathbf{W}_{\text{full}}^{(k)}$  as a composition of light-weight expert-specific  $\mathbf{W}_{\text{low}}^{(k)} \in \mathbb{R}^{(D'/H) \times Q}$  and shared  $\Phi \in \mathbb{R}^{Q \times P}$  weight matrices. The low-rank expert output,  $\mathbf{z}_j^{(k)} \in \mathbb{R}^{D'/H}$ , is given as

$$\mathbf{z}_j^{(k)} = \text{LayerNorm}(\text{ReLU}(\mathbf{W}_{\text{low}}^{(k)} \cdot \Phi \mathbf{u}_j^{(k)})). \quad (4)$$

Such low-rank decomposition (Hu et al., 2021; Handschutter et al., 2020),  $\mathbf{W}_{\text{full}}^{(k)} \simeq \mathbf{W}_{\text{low}}^{(k)} \cdot \Phi$ , allows us to scale the number of experts while maintaining a fixed parameter budget.

### 3.4 MAMMOTH OUTPUT FOR DOWNSTREAM TASKS

The low-rank expert output  $\mathbf{z}_{j,h}^{(k)}$ , corresponding to head  $h$ , is concatenated across all heads to form the final MAMMOTH output,  $\mathbf{z}_j^{(k)} = \text{Concat}([\mathbf{z}_{j,1}^{(k)}, \dots, \mathbf{z}_{j,H}^{(k)}]) \in \mathbb{R}^{D'}$ . Consequently, the output set  $\{\mathbf{z}_j^{(k)}\}_{j,k=1}^{S \cdot E}$ , instead of the original embedding set  $\{\mathbf{x}_i\}_{i=1}^N$ , is processed by  $f_{\text{MIL}}^{\text{agg.}}$ . This differs from Soft MoE (Puigcerver et al., 2024) which returns the updated patch embeddings  $\{\hat{\mathbf{x}}_i\}_{i=1}^N$  of the same set size as the input, computed as a linear combination of  $\{\mathbf{z}_j^{(k)}\}_{j,k=1}^{S \cdot E}$ . In contrast, MAMMOTH condenses morphological information into a smaller set of  $S \cdot E \ll N$  task-specific embeddings. This reduced number of input embeddings for  $f_{\text{MIL}}^{\text{agg.}}$  facilitates stable model training by simplifying the aggregation step, similar to prototype-based approaches (Vu et al., 2023; Song et al., 2024a;b).

## 4 EXPERIMENTS

### 4.1 DATASETS

**Morphological Tasks:** We evaluate on six morphological classification tasks: EBRAINS fine-grained (EBRAINS-F,  $C = 30$  classes) and coarse-grained subtyping (EBRAINS-C,  $C = 12$ ) for rare brain cancer ( $n = 2,319$  slides) (Roetzer-Pejrimovsky et al., 2022); Non-Small Cell Lung Carcinoma (NSCLC,  $C = 2$ ) subtyping with 5-fold cross validation on TCGA ( $n = 1,041$ ), with external validation on the CPTAC ( $n = 1,091$ ) and NLST ( $n = 1,008$ ) (Campbell et al., 2016); ISUP grading based on the PANDA prostate cancer challenge ( $C = 6$ ,  $n = 10,616$ ) (Bulten et al., 2022); BRACS breast carcinoma subtyping with coarse (BRACS-C,  $C = 3$ ) and fine (BRACS-F,  $C = 7$ ) granularity ( $n = 547$ ) (Brancati et al., 2021).

270 **Molecular biomarker prediction:** We evaluate MAMMOTH on 13 molecular biomarker status prediction tasks: glioma IDH1 mutation prediction (GBMLGG-C,  $C = 2$ ) and histomolecular subtyping (GBMLGG-F,  $C = 5$ ) on TCGA GBMLGG ( $n = 1,123$ ) with external evaluation on EBRAINS cases with IDH1 status ( $n = 849$ ) (Roetzer-Pejrimovsky et al., 2022), 5-fold cross-validation on TCGA lung mutation status for TP53, KRAS, STK11, and EGFR ( $C = 2, n = 524$ ), TCGA breast cancer mutation status for HER2, ER, PIK3CA, and PR ( $C = 2, n = 1,034$ ), and 10-fold cross-validation on breast core needle biopsy (BCNB) (Xu et al., 2021) for ER, PR, and HER2 ( $C = 2, n = 1,058$ ).

278 We use AUC for binary tasks and balanced accuracy for multiclass tasks, with weighted  $\kappa$  for the  
279 grading task. We use official dataset splits or splits presented in UNI (Chen et al., 2024a) otherwise.  
280 For tasks with external cohorts, we report the macro-averaged performance between each cohort.

281 **Survival prediction:** We evaluate on four survival prediction tasks, using overall survival as the  
282 clinical outcome: 5-fold site-stratified cross validation on TCGA breast cancer (BRCA,  $n=1,041$ ,  
283 WSI=1,111), Colorectal cancer (Surgen,  $n=427$ , WSI=427), TCGA lung adenocarcinoma (LUAD,  
284  $n=456$ , WSI=1,024), and TCGA lung squamous cell carcinoma (LUSC,  $n=471$ , WSI=505). For  
285 LUAD and LUSC, we also perform external validation using CPTAC (LUAD,  $n=185$ , WSI=486;  
286 LUSC,  $n=98$ , WSI=227) and NLST (LUAD,  $n=244$ , WSI=686; LUSC,  $n=118$ , WSI=322). We use  
287 concordance index (c-index) as the evaluation metric, which assesses the concordance between the  
288 rankings of true and predicted risks.

## 290 4.2 EVALUATION

292 **Baselines:** We evaluate MAMMOTH by replacing the initial linear layer for ABMIL (Ilse et al.,  
293 2018), CLAM (Lu et al., 2021), TransMIL (Shao et al., 2021), Transformer (Wagner et al., 2023;  
294 Vaswani, 2017), ILRA (Xiang & Zhang, 2023), DSMIL (Li et al., 2021), MeanMIL, and MaxMIL.  
295 We use the published hyperparameter values for all models. Additional details are in **Section A1**.

296 **Implementation:** WSIs at 20 $\times$  magnification (0.5  $\mu\text{m}/\text{pixel}$ ) were tessellated into 256 $\times$ 256  
297 patches. We extracted features using UNI (Chen et al., 2024a), a ViT-L/16 DINoV2-based model  
298 (Oquab et al., 2024) pretrained on 10<sup>5</sup> internal histology slides. We use  $E = 30$  experts,  $H = 16$   
299 heads, and  $S = 9$  slots per expert. We set  $P = 256/H$ , and  $Q = \lfloor \frac{DD' - DPH}{HP + ED'} \rfloor$  to keep the number  
300 of trainable parameters close to that of the original linear layer. Additional details are in **Section A2**.  
301

## 303 5 RESULTS

### 306 5.1 DOWNSTREAM CLINICAL TASK PERFORMANCE

308 **Morphological Classification:** Morphological classification results are presented in **Table 1**.  
309 Across all six tasks, eight testing cohorts, and eight MIL methods, MAMMOTH yields an average  
310 percent change of +7.36%. Overall, 46 out of the 48 evaluated configurations showed a performance  
311 increase. We find that both cases of decrease occur in NSCLC subtyping, a relatively simple binary  
312 task with high average performance, which may not benefit as extensively from the morphological  
313 specialization by MAMMOTH.

314 **Molecular biomarker prediction:** Average performance across biomarkers within each dataset is  
315 shown in **Table 2**. At the dataset-level, we find that MAMMOTH improves the average performance  
316 in every configuration. At the individual biomarker level (**Table A2**), MAMMOTH improves per-  
317 formance in 84 out of the 104 total configurations, with an average percent change of +2.1%. For  
318 challenging tasks with lower baseline AUC performance (e.g., BRCA PIK3CA and Lung KRAS),  
319 improvements with MAMMOTH were variable compared to tasks with overall higher AUC. Unlike  
320 tissue subtyping which is classified according to morphology, the ground truth for biomarker status  
321 is not determined by H&E, but instead molecular tests or supplemental stains. Consequently, these  
322 biomarkers with low baseline performance may lack adequate signal to reliably identify from mor-  
323 phology alone (Kather et al., 2020; Fu et al., 2020), and may not benefit as consistently from MoE  
324 as a result. Nonetheless, average performance increased across all tasks, underscoring MAMMOTH’s  
325 adaptability to diverse tasks and organs.

324 **Table 1: Tissue subtyping.** MIL performance with and without MAMMOTH. The number of classes  
 325 ( $C$ ) is indicated below each task, with its evaluation metric in parentheses. Standard deviation across  
 326 1,000 bootstrap trials is reported in parentheses. Trans., Transformer.

Task	Status	ABMIL	CLAM	TransMIL	Trans.	ILRA	Mean	Max	DSMIL	Avg.
BRACS-C	Base	67.10(1.2)	56.16(1.0)	66.80(2.7)	63.40(2.8)	63.27(1.8)	65.13(1.7)	64.54(2.4)	62.64(2.4)	63.63
$C = 3$	+Ours	72.70(1.4)	73.41(0.2)	70.52(3.1)	71.11(3.6)	74.05(2.9)	72.37(1.4)	67.21(1.6)	68.48(2.8)	71.23
(Bal. acc.)	$\Delta$	<b>+5.60</b>	<b>+17.25</b>	<b>+3.72</b>	<b>+7.71</b>	<b>+10.78</b>	<b>+7.25</b>	<b>+2.67</b>	<b>+5.84</b>	<b>+7.60</b>
BRACS-F	Base	42.84(2.5)	32.26(2.5)	32.10(2.7)	35.70(1.9)	32.65(2.4)	33.68(1.4)	33.90(2.4)	36.48(4.2)	34.95
$C = 7$	+Ours	46.12(2.4)	46.82(0.6)	38.32(1.0)	38.95(2.0)	42.50(1.9)	43.55(2.9)	35.52(0.5)	39.72(0.5)	41.44
(Bal. acc.)	$\Delta$	<b>+3.28</b>	<b>+14.56</b>	<b>+6.22</b>	<b>+3.25</b>	<b>+9.85</b>	<b>+9.87</b>	<b>+1.62</b>	<b>+3.24</b>	<b>+6.49</b>
EBRAINS-C	Base	86.10(1.1)	87.85(1.0)	87.86(1.1)	86.94(0.6)	83.41(1.7)	86.70(0.7)	84.55(1.2)	86.37(2.0)	86.22
$C = 12$	+Ours	89.98(0.7)	91.32(0.2)	88.23(1.2)	90.45(0.9)	91.68(0.8)	89.42(1.1)	85.14(0.1)	89.17(0.3)	89.43
(Bal. acc.)	$\Delta$	<b>+3.88</b>	<b>+3.47</b>	<b>+0.37</b>	<b>+3.51</b>	<b>+8.27</b>	<b>+2.72</b>	<b>+0.59</b>	<b>+2.81</b>	<b>+3.20</b>
EBRAINS-F	Base	67.20(1.0)	69.77(0.6)	65.20(0.5)	69.07(1.7)	64.64(1.2)	70.30(1.4)	64.94(1.0)	63.87(1.7)	66.87
$C = 30$	+Ours	72.40(1.2)	72.51(0.6)	74.22(0.2)	69.73(0.1)	70.23(0.3)	72.89(0.2)	68.22(0.3)	69.40(0.4)	71.20
(Bal. acc.)	$\Delta$	<b>+5.20</b>	<b>+2.74</b>	<b>+9.02</b>	<b>+0.66</b>	<b>+5.59</b>	<b>+2.59</b>	<b>+3.28</b>	<b>+5.53</b>	<b>+4.33</b>
NSCLC	Base	94.68(0.1)	91.73(0.0)	93.90(0.1)	94.69(0.1)	93.25(0.1)	91.44(0.1)	94.86(0.1)	94.08(0.1)	93.58
$C = 2$	+Ours	94.68(0.1)	93.72(0.0)	93.99(0.1)	94.04(0.1)	93.87(0.1)	93.91(0.1)	94.44(0.1)	94.43(0.1)	94.14
(AUROC)	$\Delta$	<b>+0.00</b>	<b>+1.99</b>	<b>+0.10</b>	<b>-0.65</b>	<b>+0.62</b>	<b>+2.47</b>	<b>+0.42</b>	<b>+0.35</b>	<b>+0.56</b>
PANDA	Base	93.12(0.2)	92.60(0.1)	90.75(0.7)	91.39(0.5)	91.89(0.4)	92.67(0.3)	88.79(0.3)	92.78(0.2)	91.75
$C = 6$	+Ours	94.28(0.2)	93.26(0.1)	93.68(0.3)	91.90(0.8)	94.07(0.5)	93.52(0.2)	92.34(0.2)	92.96(0.1)	93.25
(Weighted $\kappa$ )	$\Delta$	<b>+1.15</b>	<b>+0.65</b>	<b>+2.93</b>	<b>+0.51</b>	<b>+2.18</b>	<b>+0.85</b>	<b>+3.55</b>	<b>+0.19</b>	<b>+1.50</b>

340 **Table 2: Molecular Biomarker Prediction Averages** MIL model performance with the standard  
 341 linear layer (Base) and MAMMOTH (Ours). Each biomarker is a separate task, and results are aver-  
 342 aged across tasks within each dataset. Balanced accuracy is reported for GBMLGG-F, and AUROC  
 343 is reported otherwise. Propagated standard error specified in parentheses.

Dataset	Status	ABMIL	CLAM	TransMIL	Trans.	ILRA	Mean	Max	DSMIL	Avg.
	Base	81.97(0.2)	83.10(0.3)	80.76(0.4)	80.36(0.3)	81.03(0.3)	82.69(0.1)	82.91(0.3)	81.30(0.3)	81.76
BCNB	+Ours	84.26(0.2)	84.98(0.1)	82.97(0.2)	83.74(0.1)	83.27(0.2)	84.46(0.1)	84.00(0.2)	82.73(0.1)	83.80
(3 tasks)	$\Delta$	<b>+2.29</b>	<b>+1.89</b>	<b>+2.21</b>	<b>+3.38</b>	<b>+2.24</b>	<b>+1.78</b>	<b>+1.09</b>	<b>+1.44</b>	<b>+2.04</b>
	Base	71.97(0.3)	71.93(0.3)	71.38(0.7)	71.35(0.4)	70.40(0.5)	71.34(0.4)	72.47(0.7)	71.92(0.3)	71.59
BRCA	+Ours	73.65(0.3)	72.27(0.2)	73.41(0.3)	73.20(0.2)	71.68(0.4)	73.60(0.3)	72.87(0.2)	73.18(0.2)	72.98
(4 tasks)	$\Delta$	<b>+1.68</b>	<b>+0.34</b>	<b>+2.04</b>	<b>+1.85</b>	<b>+1.28</b>	<b>+2.26</b>	<b>+0.40</b>	<b>+1.26</b>	<b>+1.39</b>
	Base	67.04(0.5)	66.36(0.3)	65.25(0.7)	64.94(0.7)	65.27(0.9)	66.24(0.4)	65.50(1.2)	65.02(0.6)	65.70
Lung	+Ours	68.41(0.6)	66.89(0.3)	65.95(0.6)	67.46(0.4)	65.32(0.4)	69.17(0.4)	67.35(0.4)	66.03(0.4)	67.07
(4 tasks)	$\Delta$	<b>+1.37</b>	<b>+0.53</b>	<b>+0.70</b>	<b>+2.53</b>	<b>+0.05</b>	<b>+2.94</b>	<b>+1.85</b>	<b>+1.00</b>	<b>+1.37</b>
	Base	71.85(0.7)	72.08(0.7)	73.32(0.8)	72.00(1.3)	71.64(0.5)	72.01(0.5)	72.83(0.6)	72.21(1.2)	72.24
GBMLGG	+Ours	74.20(0.9)	72.78(0.2)	73.98(0.7)	74.40(0.6)	73.00(0.4)	73.48(0.7)	73.63(0.3)	72.74(0.4)	73.53
(2 tasks)	$\Delta$	<b>+2.35</b>	<b>+0.70</b>	<b>+0.65</b>	<b>+2.41</b>	<b>+1.36</b>	<b>+1.47</b>	<b>+0.80</b>	<b>+0.53</b>	<b>+1.28</b>

354 The average performance of MAMMOTH across all morphological and molecular tasks is shown  
 355 in **Fig. 1B.**. We observe that MAMMOTH-based models consistently outperform MIL approaches,  
 356 with even the lowest-performing model (MaxMIL, 73.9%) with MAMMOTH exceeding the strongest  
 357 baseline (ABMIL, 73.6%). Interestingly, MAMMOTH allows simple non-parametric approaches,  
 358 mean pooling and max pooling, to surpass the strong ABMIL baseline by 2.0% and 0.3%, respec-  
 359 tively. These results **suggest** that the linear layer is a bottleneck for performance, with the inclusion  
 360 of MAMMOTH leading to larger improvements, compared to changing MIL architectures.

361 **Survival prediction:** We observe that MAMMOTH also improves the prognostication performance  
 362 over the baselines in 30/32 configurations (**Table 3**), yielding an average improvement of +2.78  
 363 percentage points on the C-index. These results, taken together with the previous classification  
 364 results, underscore the versatility of MAMMOTH for both diagnostic and prognostic tasks.

366 **Table 3: Survival prediction.** MIL model performance with the standard linear layer (Base) and  
 367 MAMMOTH (Ours) using overall survival as the clinical outcome. For LUAD and LUSC, the results  
 368 are averaged across TCGA, CPTAC, and NLST cohorts. Concordance index is reported. Standard  
 369 deviation is reported in parentheses.

Task	State	ABMIL	CLAM	TransMIL	Trans.	ILRA	Mean	Max	DSMIL	Avg.
	Base	58.56(4.5)	61.91(4.1)	58.86(3.9)	56.90(4.1)	57.26(5.2)	58.27(8.5)	56.69(5.1)	59.31(4.3)	58.68
BRCA	+Ours	63.98(4.9)	64.36(3.3)	65.02(5.4)	65.23(4.2)	63.94(4.1)	63.18(3.9)	62.70(5.3)	60.43(4.4)	63.48
	$\Delta$	<b>+5.42</b>	<b>+2.45</b>	<b>+6.16</b>	<b>+8.33</b>	<b>+6.68</b>	<b>+4.91</b>	<b>+6.01</b>	<b>+1.12</b>	<b>+4.80</b>
	Base	63.67(4.7)	63.93(4.1)	57.94(3.2)	60.59(4.8)	62.29(4.5)	64.03(5.2)	56.53(4.4)	60.17(5.4)	61.14
SURGEN	+Ours	65.64(4.5)	64.99(5.3)	63.10(3.9)	63.91(4.9)	64.80(5.2)	64.97(5.2)	59.31(4.6)	65.11(4.7)	63.98
	$\Delta$	<b>+1.97</b>	<b>+1.06</b>	<b>+5.16</b>	<b>+3.32</b>	<b>+2.51</b>	<b>+0.94</b>	<b>+2.78</b>	<b>+4.94</b>	<b>+2.84</b>
	Base	58.70(3.6)	58.97(3.4)	56.76(4.1)	58.31(5.1)	57.24(4.1)	59.11(3.6)	55.95(4.7)	58.14(4.6)	57.90
LUAD	+Ours	60.12(3.7)	61.89(2.8)	60.97(2.3)	60.49(3.4)	58.10(4.5)	60.56(3.1)	57.18(4.4)	57.99(3.3)	59.66
	$\Delta$	<b>+1.42</b>	<b>+2.92</b>	<b>+4.21</b>	<b>+2.18</b>	<b>+0.86</b>	<b>+1.46</b>	<b>+1.23</b>	<b>-0.15</b>	<b>+1.60</b>
	Base	56.62(4.0)	55.63(4.7)	52.53(4.5)	55.11(5.1)	54.44(5.8)	56.04(5.0)	49.39(2.8)	51.26(3.7)	53.88
LUSC	+Ours	59.32(4.8)	58.91,2,1	53.48(2.8)	55.68(5.3)	54.48(3.9)	58.30(5.1)	50.12(3.3)	55.69(2.6)	55.75
	$\Delta$	<b>+2.70</b>	<b>+3.28</b>	<b>+0.94</b>	<b>-0.44</b>	<b>+0.03</b>	<b>+2.26</b>	<b>+0.73</b>	<b>+4.43</b>	<b>+1.87</b>

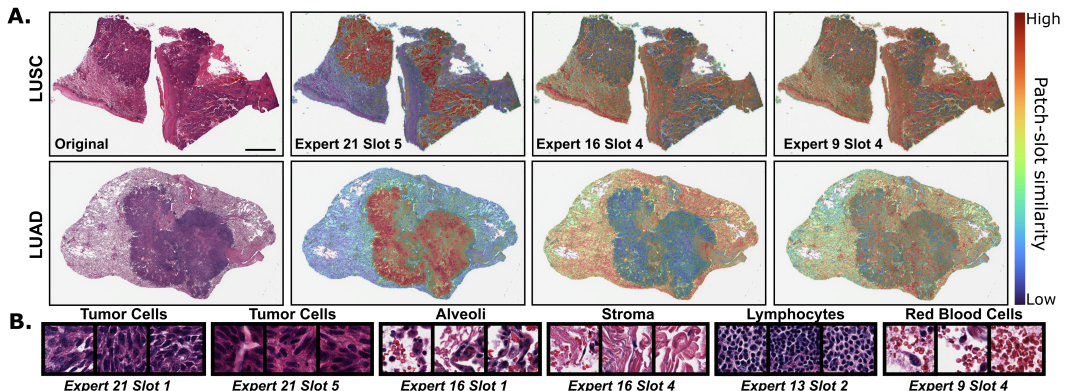
378  
379

## 5.2 INTERPRETABILITY

380 The primary motivation for using MoE with WSIs is to process distinct morphologic phenotypes  
 381 with specialized experts. To assess whether the routing mechanism led to expert specialization of  
 382 distinct morphological concepts, two board-certified pathologists examined the routing scores be-  
 383 tween each slot and patch embedding (Fig. 3B and Section A3), finding that the model consolidates  
 384 morphologically similar patches into the same slot. For instance, the patches with high weights  
 385 routed to slot 5 of expert 21 (Fig. 3C) overlap heavily with the tumor region of both LUAD and  
 386 LUSC slides. The routing scheme consistently routed different morphologies into distinct slots,  
 387 such as stroma and alveoli to Expert 16, and lymphocytes and red blood cells to Expert 9. These re-  
 388 sults suggest that the slot aggregation enables expert specialization by grouping the similar patches  
 389 across a variety of concepts. Additional examples are in Figs. A3- A7. In addition, we quantify ex-  
 390 pert specialization at the dataset-level using the vision-language model MUSK (Xiang et al., 2025)  
 391 to label each patch according to its similarity to a set of histologic terms, confirming that experts  
 392 differentially prioritize concepts such as tumor cells, alveoli, stroma, and lymphocytes (Fig. A9).

393 **Mechanism of specialization:** Additionally, we investigated the origins of specialization by track-  
 394 ing the training dynamics of slots identified as specialized experts at model convergence. We ob-  
 395 served that these slots exhibit higher routing weights for their target concepts even at initializa-  
 396 tion, followed by a sharp increase and stabilization within the first epoch (Fig. A9). We hypoth-  
 397 esize that, because foundation model embeddings already cluster similar morphological concepts  
 398 together (Chen et al., 2024a; Lu et al., 2024b; Xiang et al., 2025), the slot embeddings are able to  
 399 implicitly group semantically similar patches together at initialization (Figs A11- A12).

400 **Instance-Gradient Interference:** Lastly, we find that heterogeneous instances yield conflicting  
 401 gradient updates in standard linear layers (Fig. A10A-B), which we name **Instance Gradient In-  
 402 terference (IGI)**. We observe that MAMMOTH mitigates IGI by routing heterogeneous instances to  
 403 distinct experts, enabling decoupled updates and increased gradient similarity (Fig. A10C), provid-  
 404 ing insight into the rapid specialization observed at the start of training.



405  
 406  
 407  
 408  
 409  
 410  
 411  
 412  
 413  
 414  
 415  
 416  
 417  
 418 **Figure 3: Visualization of patch routing** **A.** WSI images of LUSC and LUAD for NSCLC subtyp-  
 419 ing task, with heatmap of routing weights from patches to three different slots. **B.** Highest similarity  
 420 patches for each slot among patches from LUSC slide and LUAD slide. Morphological clusters are  
 421 annotated by two board-certified pathologists, indicating that morphologically similar patches are  
 422 collected within a single slot. Scale bars: **A.** 500  $\mu$ m, **B.** 20  $\mu$ m.

423  
424 5.3 ABLATION STUDIES  
425

426 **Model design ablations:** We first investigate how different components of MAMMOTH affect down-  
 427 stream performance by removing each design component. Performance is measured with ABMIL  
 428 averaged across six tasks: BRACS C/F, EBRAINS C/F, and GBMLGG C/F. The key ablations  
 429 are as follows. **(1) MoE method:** We replace MAMMOTH with various related methods: Soft  
 430 MoE (Puigcerver et al., 2024) and sparse Multiheaded MoE (Wu et al., 2024a), two popular sparse  
 431 MoE methods (softmax-based MoE (Shazeer et al., 2017) and sinkhorn-based MoE (Tay et al.,  
 432 2020)), the pathology-specific routing method, PaMoE, and the original linear layer. **(2) Num.**

**heads:** We investigate the effect of removing the multihead component of MAMMOTH by setting  $H = 1$ . **(3) Slot transformation:** We use an expert-specific dense transformation  $\mathbf{W}_{\text{full}}^{(k)}$ , instead of its low-rank approximation,  $\mathbf{W}_{\text{low}}^{(k)}\Phi$ . **(4) Shared  $\Phi$ :** We replace the shared low-rank projection,  $\Phi$ , with an expert-specific projection to assess the effect of weight-sharing. **(5) Initial projection with  $\mathbf{W}$ :** We replace the initial projection  $\mathbf{W}$  with an identity matrix. This results in higher-dimensional slot representations and increased model size. **(6) MAMMOTH output:** Following Soft MoE, we update the patch embeddings  $\{\bar{\mathbf{x}}_i\}_{i=1}^N$  as a linear combination of slot outputs  $\{\mathbf{z}_j^{(k)}\}_{j,k=1}^{S \cdot E}$  and feed these updated patch embeddings into the MIL module. **(7) Pre-aggregation module:** We replace MAMMOTH with other approaches that modify the set of patch features prior to MIL aggregation such as patch feature re-embedding (Tang et al., 2024), local self-attention (Guo et al., 2025), or sampling (Zhu et al., 2025). Further details are provided in Section A4. **MoE Target:** We evaluate a pathology-specific MoE method which replaces the full MIL aggregation layer with a mixture of ABMIL-based experts (Li et al., 2024), rather than targeting only the linear layer.

Table 4: **Ablation studies over design components.** (a) Ablations for model design components. (b) Inference efficiency comparison. Metrics are measured on random inputs of shape  $10,000 \times 1,024$  averaged over 1,000 forward passes. Best performance among MoE methods shown in **bold**, second best underlined. (c) Performance with GigaPath, Musk, and Virchow, averaged across ABMIL, TransMIL, MaxMIL, and CLAM. Lin., linear; Sp., Sparse; MH, multihead; soft., softmax; sink., sinkhorn.

(a) Model design ablations			(b) Inference efficiency for MoEs			
Ablation	Model	Avg.	Architecture	Latency (MS)	GPU (MB)	GFLOPs
Full model	Ours	<b>71.6</b>	Linear	0.6	74.0	5.3
MoE method	Ours $\Rightarrow$ Lin. layer	68.1 (-4.9%)	Sp. Soft	19.2	140.9	10.8
	Ours $\Rightarrow$ Soft MoE	66.9 (-6.6%)	Sp. Sink.	27.5	141.2	10.8
	Ours $\Rightarrow$ Sp. MH	69.1 (-3.5%)	Sp. MH	194.0	2169.6	20.3
	Ours $\Rightarrow$ Sp. soft.	67.8 (-5.3%)	Soft	<b>4.8</b>	<u>119.6</u>	<b>0.8</b>
	Ours $\Rightarrow$ Sp. sink.	67.6 (-5.6%)	PaMoE	24.8	610.8	125.9
	Ours $\Rightarrow$ PaMoE	69.2 (-3.4%)	Ours	<u>19.5</u>	<b>89.2</b>	<u>2.8</u>
Num. heads	16 $\Rightarrow$ 1	67.7 (-5.4%)				
Slot transform	$\mathbf{W}_{\text{low}}^{(k)}\Phi$ $\Rightarrow$ $\mathbf{W}_{\text{full}}^{(k)}$	69.0 (-3.6%)				
$\Phi$	Shared $\Rightarrow$ Per-expert	70.6 (-1.4%)				
$\mathbf{W}$	Learned $\Rightarrow$ Identity	68.2 (-4.7%)				
Output	Slots $\Rightarrow$ Patches	68.2 (-4.7%)				
Pre-Aggregation Module	MoE $\Rightarrow$ RRT	69.5 (-2.9%)				
		MIL Drop	69.6 (-2.8%)			
		Querent	68.9 (-3.8%)			
MoE Target	Lin. layer $\Rightarrow$ Aggregator (M4)	67.4 (-5.9%)				

(c) Ablation for feature encoders				
Task	State	GigaPath	Musk	Virchow
EBRAINS-C	Base	86.03	81.90	84.03
	+Ours	87.13	84.50	86.30
	$\Delta$	<b>+1.10</b>	<u>+2.60</u>	<b>+2.27</b>
EBRAINS-F	Base	66.78	65.28	66.88
	+Ours	79.02	76.02	77.78
	$\Delta$	<b>+12.24</b>	<u>+10.74</u>	<b>+10.90</b>
BRACS-C	Base	61.28	58.90	60.60
	+Ours	66.75	66.82	69.55
	$\Delta$	<b>+5.47</b>	<u>+7.92</u>	<b>+8.95</b>
BRACS-F	Base	35.05	35.15	35.20
	+Ours	41.50	43.28	41.50
	$\Delta$	<b>+6.45</b>	<u>+8.13</u>	<b>+6.30</b>

The results in Table 4a show that each design element contributes to MAMMOTH’s efficacy. Using alternative single-head MoE methods leads to an average  $-5.4\%$  change in performance. For both sparse MoE and MAMMOTH, adding a multihead component improves performance, though the benefits of using multiple heads is particularly pronounced in MAMMOTH, in which removing the multihead component leads to a  $-5.4\%$  change (Num. heads: 16  $\Rightarrow$  1), while changing the architecture from sparse multihead to sparse MoE leads to a  $-2.4\%$  change (Sp. soft  $\Rightarrow$  Sp. MH), emphasizing the confluent benefits of using multiple heads with soft assignments. Replacing MAMMOTH with the pathology-specific PaMoE leads to a  $-3.4\%$  change in performance. This degradation in performance is present across all 8 MIL methods, with PaMoE exhibiting an average  $-4.0$  decrease in absolute performance compared to MAMMOTH (Table A5). Performance within each dataset and parameter count for each MoE method are indicated in Tables A3 and A4.

Using dense expert-specific transformation  $\mathbf{W}_{\text{full}}^{(k)}$ , removing weight sharing  $\Phi$ , and removing initial dimensionality reduction layer  $\mathbf{W}$  all lead to performance decrease, highlighting the importance of our parameter-efficient design. The Soft MoE approach of using  $N$  updated patch representations rather than our proposed  $S$  slot-level outputs leads to a  $4.7\%$  performance increase, indicating the benefits of consolidating similar patches for downstream aggregation. While other pre-aggregation feature modification approaches indeed increase the performance over the original linear layer, they

486 still lag behind MAMMOTH, with even the best performing feature re-embedding approach (RRT)  
 487 2.9% worse than MAMMOTH. We report the complete comparison across all classification tasks and  
 488 MIL methods in **Tables A6, A7, and A8**. Similarly, the MoE-based MIL method, M4, exhibits a  
 489 sharp drop of -5.9% performance, highlighting the value of targetting the initial task-specific trans-  
 490 formation. Performance of M4 across all tasks is shown in **Table A9**.

491 **Inference-time efficiency:** We evaluate inference-time efficiency for various task-specific trans-  
 492 formation layers according to peak GPU memory, per-sample latency, and per-sample GFLOPS  
 493 in **Table 4b**. The per-sample metrics are averaged over 1,000 forward passes of random samples  
 494 shaped  $10,000 \times 1,024$ . As anticipated, the linear layer achieves the lowest latency and GPU usage.  
 495 However, MAMMOTH is both *faster* and more *lightweight* than all Sparse MoE methods. Consider-  
 496 ing that MAMMOTH also outperformed Soft MoE and the linear layer in downstream tasks, we  
 497 conclude that MAMMOTH effectively balances performance and efficiency.

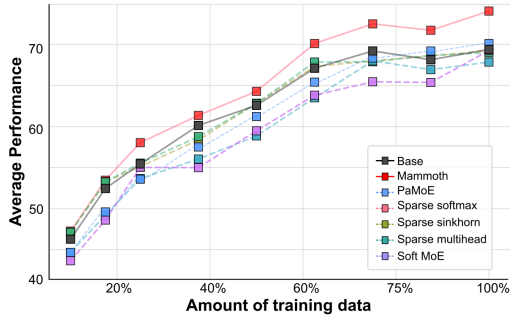
498 **Patch Encoder:** With new CPath feature encoders continuously emerging, we evaluate performance  
 499 using GigaPath (Xu et al., 2024), Musk (Xiang et al., 2025), and Virchow (Vorontsov et al., 2024)  
 500 as patch encoders on EBRAINS C/F and BRACS C/F. Across the four MIL methods investigated  
 501 (ABMIL, CLAM, TransMIL, MaxMIL), MAMMOTH leads to an average improvement in balanced  
 502 accuracy of +3.52% (GigaPath), +5.36% (MUSK), and +5.24% (Virchow) (**Tables 4c** and **A1**),  
 503 indicating that MAMMOTH is robust to feature encoder choice.

504 **Data efficiency:** A core design principle of MAMMOTH is to facilitate stable training in the  
 505 data-scarce regimes common in CPath. We test this hypothesis by training ABMIL and Trans-  
 506 MIL on different fractions of the training dataset (**Fig. 4**), on EBRAINS-C/F, BRACS-C/F, and  
 507 GBMLGG-C. This is repeated over three independently sampled training data subsets. MAM-  
 508 MOTH attains the highest overall performance across all fractions compared to other MoE meth-  
 509 ods. Notably, other MoE methods consistently underperform compared to the linear layer (base)  
 510 at lower data fractions, highlighting the limitations of traditional MoE approaches for CPath.

511 **Key hyperparameters:** We perform ablations  
 512 over the key hyperparameters,  $H$ ,  $E$ , and  $S$ .  
 513 First, we assess the effect of varying  $H$  and  
 514  $E$  for EBRAINS-F, LUNG TP53, and BRCA  
 515 HER2 tasks with ABMIL and TransMIL. We  
 516 find that with a low number of heads ( $H \in$   
 517  $\{2, 4\}$ ), performance depends on the number  
 518 of experts selected, with high expert counts  
 519 ( $E \in \{72, 96\}$ ) showing low overall perfor-  
 520 mance (**Fig. A1**). Meanwhile, increasing the  
 521 number of heads ( $H \in \{8, 16, 32\}$ ) stabilizes  
 522 performance, with high expert counts ( $E \in$   
 523  $\{72, 96\}$ ) converging with lower expert counts  
 524 ( $E \in \{4, 8\}$ ). Additionally, we observe that 8-  
 525 48 experts with  $H \in \{16, 32\}$  achieve the high-  
 526 est overall performance. We hypothesize that,  
 527 because increasing the number of experts leads  
 528 to a lower rank for  $Q$ , this intermediate expert  
 529 count is a “sweet spot” that balances repres-  
 530 entation capacity with morphological specializa-  
 531 tion. We conduct a similar experiment varying the total  
 532 slots, finding that low expert ( $E \in \{2, 4\}$ ) counts reach perform best with low total slots (50 – 100),  
 533 while higher expert counts (24-96 experts) tend to perform better with 200-400 total slots (**Fig. A2**).

## 532 6 CONCLUSION AND LIMITATIONS

533 We introduced MAMMOTH, a multihead soft MoE module designed to enhance slide-level perfor-  
 534 mance in computational pathology. MAMMOTH consistently improves classification performance  
 535 by leveraging a large set of specialized, low-rank feedforward layers, without substantially alter-  
 536 ing the total parameter count. Limitations include the use of a fixed configuration of experts, slots,  
 537 and heads for each task. Future works could investigate dynamically selecting these hyperparam-  
 538 eters, initializing the slot embeddings with prototype learning-based approaches, and broadening to  
 539 multimodal inputs.



534 **Figure 4: Data efficiency of MAMMOTH.** MoE  
 535 performance with varying training samples aver-  
 536 aged across tasks EBRAINS-C/F, BRACS-C/F,  
 537 GBMLGG-C, models ABMIL and TransMIL, and  
 538 3 randomly sampled subsets of the training data.

540 ETHICS STATEMENT  
541

542 This work utilizes datasets derived from publicly available images of tissues collected from  
543 anonymized human subjects. No personally identifiable information was accessible to the authors  
544 at any stage of this study. The analysis did not examine model performance across patient demo-  
545 graphic subgroups; we acknowledge that further research is needed to ensure algorithmic fairness,  
546 particularly with respect to underrepresented populations.

548 REPRODUCIBILITY STATEMENT  
549

550 To promote reproducibility, we have submitted the codebase to initialize MAMMOTH, as well as  
551 examples for how to equip two popular MIL models, ABMIL and TransMIL, with MAMMOTH. We  
552 have described the training details for MAMMOTH in **Sections A1** and **A2** and key ablations in  
553 **Sections 5.3, A3.1, A4**. Details for interpretability experiments are described in **Section A3**. All  
554 datasets used were publicly available and described in **Sections 4** and **A4.5**.

556 REFERENCES  
557

558 Khalid Abdul Jabbar, Shan E Ahmed Raza, Rachel Rosenthal, Mariam Jamal-Hanjani, Selvaraju  
559 Veeriah, et al. Geospatial immune variability illuminates differential evolution of lung adenocar-  
560 cinoma. *Nature Medicine*, pp. 1–9, 2020.

561 Babak Ehteshami Bejnordi, Mitko Veta, Paul Johannes Van Diest, Bram Van Ginneken, Nico  
562 Karssemeijer, et al. Diagnostic assessment of deep learning algorithms for detection of lymph  
563 node metastases in women with breast cancer. *JAMA*, 318(22):2199–2210, 2017.

564 Nadia Brancati, Anna Maria Anniciello, Pushpak Pati, Daniel Riccio, Giosuè Scognamiglio, et al.  
565 BRACS: A Dataset for BReAst Carcinoma Subtyping in H&E Histology Images, November  
566 2021. arXiv:2111.04740 [cs, eess, q-bio].

567 Cameron W. Brennan, Roel G. W. Verhaak, Aaron McKenna, Benito Campos, and Houtan et al.  
568 Noushmehr. The Somatic Genomic Landscape of Glioblastoma. *Cell*, 155(2):462–477, October  
569 2013. ISSN 0092-8674. doi: 10.1016/j.cell.2013.09.034.

570 Wouter Bulten, Hans Pinckaers, Hester van Boven, Robert Vink, Thomas de Bel, et al. Automated  
571 deep-learning system for gleason grading of prostate cancer using biopsies: a diagnostic study.  
572 *The Lancet Oncology*, 21(2):233–241, 2020.

573 Wouter Bulten, Kimmo Kartasalo, Po-Hsuan Cameron Chen, Peter Ström, Hans Pinckaers, et al.  
574 Artificial intelligence for diagnosis and gleason grading of prostate cancer: the panda challenge.  
575 *Nature Medicine*, 28(1):154–163, 2022.

576 Weilin Cai, Juyong Jiang, Fan Wang, Jing Tang, Sunghun Kim, and Jiayi Huang. A Survey on  
577 Mixture of Experts, August 2024. arXiv:2407.06204.

578 Gabriele Campanella, Matthew G Hanna, Luke Geneslaw, Allen Miraflor, Werneck Krauss Silva,  
579 et al. Clinical-grade computational pathology using weakly supervised deep learning on whole  
580 slide images. *Nature medicine*, 25(8):1301–1309, 2019.

581 Gabriele Campanella, Shengjia Chen, Ruchika Verma, Jennifer Zeng, Aryeh Stock, Matt Croken,  
582 Brandon Veremis, Abdulkadir Elmas, Kuan lin Huang, Ricky Kwan, Jane Houldsworth, Adam J.  
583 Schoenfeld, and Chad Vanderbilt. A clinical benchmark of public self-supervised pathology foun-  
584 dation models, 2024.

585 Joshua D. Campbell, Anton Alexandrov, Jaegil Kim, Jeremiah Wala, Alice H. Berger, et al. Distinct  
586 patterns of somatic genome alterations in lung adenocarcinomas and squamous cell carcinomas.  
587 *Nature Genetics*, 48(6):607–616, June 2016. ISSN 1546-1718. doi: 10.1038/ng.3564. URL  
588 <https://www.nature.com/articles/ng.3564>. Publisher: Nature Publishing Group.

594 Cancer Genome Atlas Research Network, Daniel J. Brat, Roel G. W. Verhaak, Kenneth D. Aldape,  
 595 W. K. Alfred Yung, et al. Comprehensive, Integrative Genomic Analysis of Diffuse Lower-Grade  
 596 Gliomas. *The New England Journal of Medicine*, 372(26):2481–2498, June 2015. ISSN 1533-  
 597 4406. doi: 10.1056/NEJMoa1402121.

598 Richard J. Chen, Tong Ding, Ming Y. Lu, Drew F. K. Williamson, Guillaume Jaume, Andrew H.  
 599 Song, Bowen Chen, Andrew Zhang, Daniel Shao, et al. Towards a general-purpose foundation  
 600 model for computational pathology. *Nature Medicine*, 2024a.

601 Shengjia Chen, Gabriele Campanella, Abdulkadir Elmas, Aryeh Stock, Jennifer Zeng, et al. Bench-  
 602 marking Embedding Aggregation Methods in Computational Pathology: A Clinical Data Per-  
 603 spective, July 2024b. arXiv:2407.07841.

604 Zewen Chi, Li Dong, Shaohan Huang, Damai Dai, Shuming Ma, et al. On the Representation  
 605 Collapse of Sparse Mixture of Experts, October 2022. arXiv:2204.09179.

606 Aidan Clark, Diego de las Casas, Aurelia Guy, Arthur Mensch, Michela Paganini, et al. Unified  
 607 Scaling Laws for Routed Language Models, February 2022. arXiv:2202.01169.

608 Nan Du, Yanping Huang, Andrew M. Dai, Simon Tong, Dmitry Lepikhin, et al. GLaM: Efficient  
 609 Scaling of Language Models with Mixture-of-Experts, August 2022. arXiv:2112.06905.

610 David Eigen, Marc’Aurelio Ranzato, and Ilya Sutskever. Learning factored representations in a deep  
 611 mixture of experts. *arXiv preprint arXiv:1312.4314*, 2013.

612 William Fedus, Barret Zoph, and Noam Shazeer. Switch Transformers: Scaling to Trillion Parameter  
 613 Models with Simple and Efficient Sparsity, June 2022. arXiv:2101.03961.

614 Yu Fu, Alexander W. Jung, Ramon Viñas Torne, Santiago Gonzalez, Harald Vöhringer, et al. Pan-  
 615 cancer computational histopathology reveals mutations, tumor composition and prognosis. *Nature  
 616 Cancer*, 1(8):800–810, August 2020. ISSN 2662-1347. Publisher: Nature Publishing Group.

617 Ze-Feng Gao, Peiyu Liu, Wayne Xin Zhao, Zhong-Yi Lu, and Ji-Rong Wen. Parameter-  
 618 Efficient Mixture-of-Experts Architecture for Pre-trained Language Models, October 2022.  
 619 arXiv:2203.01104.

620 Michael A. Gillette, Shankha Satpathy, Song Cao, Saravana M. Dhanasekaran, Suhas V. Vasaikar,  
 621 et al. Proteogenomic Characterization Reveals Therapeutic Vulnerabilities in Lung Adenocarci-  
 622 noma. *Cell*, 182(1):200–225.e35, July 2020. ISSN 0092-8674. doi: 10.1016/j.cell.2020.06.013.

623 Zhengrui Guo, Qichen Sun, Jiabo Ma, Lishuang Feng, Jinzhuo Wang, and Hao Chen. Context  
 624 matters: Query-aware dynamic long sequence modeling of gigapixel images. *arXiv preprint  
 625 arXiv:2501.18984*, 2025.

626 Pierre De Handschutter, Nicolas Gillis, and Xavier Siebert. Deep matrix factorizations, October  
 627 2020. URL <http://arxiv.org/abs/2010.00380>. arXiv:2010.00380.

628 Xu Owen He. Mixture of A Million Experts, July 2024. arXiv:2407.04153.

629 Edward J. Hu, Yelong Shen, Phillip Wallis, Zeyuan Allen-Zhu, Yuanzhi Li, Shean Wang, Lu Wang,  
 630 and Weizhu Chen. LoRA: Low-Rank Adaptation of Large Language Models, October 2021.  
 631 arXiv:2106.09685.

632 Maximilian Ilse, Jakub Tomczak, and Max Welling. Attention-based deep multiple instance learn-  
 633 ing. In *International conference on machine learning*, pp. 2127–2136. PMLR, 2018.

634 Robert A Jacobs, Michael I Jordan, Steven J Nowlan, and Geoffrey E Hinton. Adaptive mixtures of  
 635 local experts. *Neural computation*, 3(1):79–87, 1991.

636 Ganesh Jawahar, Haichuan Yang, Yunyang Xiong, Zechun Liu, Dilin Wang, et al. Mixture-of-  
 637 Supernets: Improving Weight-Sharing Supernet Training with Architecture-Routed Mixture-of-  
 638 Experts, August 2024. arXiv:2306.04845.

639 Michael I Jordan and Robert A Jacobs. Hierarchical mixtures of experts and the em algorithm.  
 640 *Neural computation*, 6(2):181–214, 1994.

648 Neel Kanwal, Farbod Khoraminia, Umay Kiraz, Andres Mosquera-Zamudio, Carlos Monteagudo,  
 649 et al. Equipping Computational Pathology Systems with Artifact Processing Pipelines: A Show-  
 650 case for Computation and Performance Trade-offs, May 2024. arXiv:2403.07743.

651

652 Jakob Nikolas Kather, Lara R. Heij, Heike I. Grabsch, Chiara Loeffler, Amelie Echle, et al. Pan-  
 653 cancer image-based detection of clinically actionable genetic alterations. *Nature Cancer*, 1(8):  
 654 789–799, August 2020. ISSN 2662-1347. doi: 10.1038/s43018-020-0087-6. URL <https://www.nature.com/articles/s43018-020-0087-6>. Publisher: Nature Publishing  
 655 Group.

656

657 Dmitry Lepikhin, HyoukJoong Lee, Yuanzhong Xu, Dehao Chen, Orhan Firat, et al. GShard:  
 658 Scaling Giant Models with Conditional Computation and Automatic Sharding, June 2020.  
 659 arXiv:2006.16668.

660

661 Bin Li, Yin Li, and Kevin W Eliceiri. Dual-stream multiple instance learning network for whole slide  
 662 image classification with self-supervised contrastive learning. In *Proceedings of the IEEE/CVF*  
 663 *conference on computer vision and pattern recognition*, pp. 14318–14328, 2021.

664

665 Junyu Li, Ye Zhang, Wen Shu, Xiaobing Feng, Yingchun Wang, et al. M4: Multi-Proxy Multi-Gate  
 666 Mixture of Experts Network for Multiple Instance Learning in Histopathology Image Analysis,  
 667 July 2024. arXiv:2407.17267.

668

669 Tianlin Liu, Mathieu Blondel, Carlos Riquelme, and Joan Puigcerver. Routers in Vision Mixture of  
 670 Experts: An Empirical Study, April 2024. arXiv:2401.15969.

671

672 Ming Y. Lu, Drew F. K. Williamson, Tiffany Y. Chen, Richard J. Chen, Matteo Barbieri, and Faisal  
 673 Mahmood. Data-efficient and weakly supervised computational pathology on whole-slide images.  
 674 *Nature Biomedical Engineering*, 5(6):555–570, June 2021. ISSN 2157-846X. doi: 10.1038/  
 675 s41551-020-00682-w. Number: 6 Publisher: Nature Publishing Group.

676

677 Ming Y. Lu, Bowen Chen, Drew F. K. Williamson, Richard J. Chen, Ivy Liang, et al. A visual-  
 678 language foundation model for computational pathology. *Nature Medicine*, 30(3):863–874,  
 679 March 2024a. ISSN 1546-170X. Publisher: Nature Publishing Group.

680

681 Ming Y Lu, Bowen Chen, Drew FK Williamson, Richard J Chen, Ivy Liang, Tong Ding, Guillaume  
 682 Jaume, Igor Odintsov, Long Phi Le, Georg Gerber, et al. A visual-language foundation model for  
 683 computational pathology. *Nature Medicine*, pp. 1–12, 2024b.

684

685 Andriy Marusyk and Kornelia Polyak. Tumor heterogeneity: causes and consequences. *Biochimica  
 686 et biophysica acta*, 1805(1):105, January 2010. ISSN 0006-3002. doi: 10.1016/j.bbcan.2009.11.  
 687 002.

688

689 Peter Neidlinger, Tim Lenz, Sebastian Foersch, Chiara ML Loeffler, Jan Clusmann, Marco Gustav,  
 690 Lawrence A Shaktah, Rupert Langer, Bastian Dislich, Lisa A Boardman, et al. A deep learning  
 691 framework for efficient pathology image analysis. *arXiv preprint arXiv:2502.13027*, 2025.

692

693 James Oldfield, Markos Georgopoulos, Grigoris G. Chrysos, Christos Tzelepis, Yannis Panagakis,  
 694 Mihalis A. Nicolaou, Jiankang Deng, and Ioannis Patras. Multilinear Mixture of Experts: Scalable  
 695 Expert Specialization through Factorization, October 2024. URL <http://arxiv.org/abs/2402.12550>. arXiv:2402.12550.

696

697 Maxime Oquab, Timothée Darcet, Théo Moutakanni, Huy V. Vo, and et al. Marc Szafraniec. DI-  
 698 NOv2: Learning robust visual features without supervision. *Transactions on Machine Learning  
 699 Research*, 2024. ISSN 2835-8856.

700

701 Joan Puigcerver, Carlos Riquelme, Basil Mustafa, and Neil Houlsby. From Sparse to Soft Mixtures  
 702 of Experts, May 2024. arXiv:2308.00951 [cs].

703

704 Carlos Riquelme, Joan Puigcerver, Basil Mustafa, Maxim Neumann, Rodolphe Jenatton, André Su-  
 705 sano Pinto, Daniel Keysers, and Neil Houlsby. Scaling Vision with Sparse Mixture of Experts,  
 706 June 2021.

702 Thomas Roetzer-Pejrimovsky, Anna-Christina Moser, Baran Atli, Clemens Christian Vogel, Petra A  
 703 Mercea, Romana Priboda, Ellen Gelpi, Christine Haberler, Romana Höftberger, Johannes A Hain-  
 704 fellner, et al. The digital brain tumour atlas, an open histopathology resource. *Scientific Data*, 9  
 705 (1):55, 2022.

706 Joel Saltz, Rajarsi Gupta, Le Hou, Tahsin Kurc, Pankaj Singh, Vu Nguyen, Dimitris Samaras, Ken-  
 707 neth R Shroyer, Tianhao Zhao, Rebecca Batiste, et al. Spatial organization and molecular corre-  
 708 lation of tumor-infiltrating lymphocytes using deep learning on pathology images. *Cell reports*,  
 709 23(1):181–193, 2018.

710 Shankha Satpathy, Karsten Krug, Pierre M. Jean Beltran, Sara R. Savage, Francesca Petralia,  
 711 et al. A proteogenomic portrait of lung squamous cell carcinoma. *Cell*, 184(16):4348–  
 712 4371.e40, August 2021. ISSN 0092-8674. doi: 10.1016/j.cell.2021.07.016. URL <https://www.sciencedirect.com/science/article/pii/S0092867421008576>.

713 Daniel Shao, Richard J Chen, Andrew H Song, Joel Runevic, Ming Y Lu, Tong Ding, and Faisal  
 714 Mahmood. Do multiple instance learning models transfer? In *Forty-second International Con-  
 715 ference on Machine Learning*, 2025.

716 Zuchen Shao, Hao Bian, Yang Chen, Yifeng Wang, Jian Zhang, Xiangyang Ji, et al. Transmil:  
 717 Transformer based correlated multiple instance learning for whole slide image classification. *Ad-  
 718 vances in Neural Information Processing Systems*, 34:2136–2147, 2021.

719 Noam Shazeer, Azalia Mirhoseini, Krzysztof Maziarz, Andy Davis, Quoc Le, Geoffrey Hinton,  
 720 and Jeff Dean. Outrageously large neural networks: The sparsely-gated mixture-of-experts layer.  
 721 *arXiv preprint arXiv:1701.06538*, 2017.

722 Andrew H Song, Guillaume Jaume, Drew FK Williamson, Ming Y Lu, Anurag Vaidya, Tiffany R  
 723 Miller, and Faisal Mahmood. Artificial intelligence for digital and computational pathology. *Na-  
 724 ture Reviews Bioengineering*, 1(12):930–949, 2023.

725 Andrew H. Song, Richard J. Chen, Tong Ding, Drew F. K. Williamson, Guillaume Jaume, and  
 726 Faisal Mahmood. Morphological Prototyping for Unsupervised Slide Representation Learning in  
 727 Computational Pathology, May 2024a. arXiv:2405.11643.

728 Andrew H Song, Richard J Chen, Guillaume Jaume, Anurag Jayant Vaidya, Alexander Baras, and  
 729 Faisal Mahmood. Multimodal prototyping for cancer survival prediction. In *Forty-first Interna-  
 730 tional Conference on Machine Learning*, 2024b.

731 Shawn Tan, Yikang Shen, Zhenfang Chen, Aaron Courville, and Chuang Gan. Sparse Universal  
 732 Transformer, October 2023. arXiv:2310.07096.

733 Wenhao Tang, Fengtao Zhou, Sheng Huang, Xiang Zhu, Yi Zhang, and Bo Liu. Feature Re-  
 734 Embedding: Towards Foundation Model-Level Performance in Computational Pathology, July  
 735 2024. URL <http://arxiv.org/abs/2402.17228>. arXiv:2402.17228 [cs].

736 Yi Tay, Dara Bahri, Liu Yang, Donald Metzler, and Da-Cheng Juan. Sparse Sinkhorn Attention,  
 737 February 2020.

738 A Vaswani. Attention is all you need. *Advances in Neural Information Processing Systems*, 2017.

739 Eugene Vorontsov, Alican Bozkurt, Adam Casson, George Shaikovski, Michal Zelechowski, Kristen  
 740 Severson, Eric Zimmermann, James Hall, Neil Tenenholz, Nicolo Fusi, et al. A foundation model  
 741 for clinical-grade computational pathology and rare cancers detection. *Nature medicine*, pp. 1–12,  
 742 2024.

743 Quoc Dang Vu, Kashif Rajpoot, Shan E Ahmed Raza, and Nasir Rajpoot. Handcrafted histological  
 744 transformer (h2t): Unsupervised representation of whole slide images. *Medical image analysis*,  
 745 85:102743, 2023.

746 Sophia J. Wagner, Daniel Reisenbüchler, Nicholas P. West, Jan Moritz Niehues, and et al. Zhu,  
 747 Jiefu. Transformer-based biomarker prediction from colorectal cancer histology: A large-scale  
 748 multicentric study. *Cancer Cell*, 41(9):1650–1661.e4, September 2023. ISSN 15356108. doi:  
 749 10.1016/j.ccr.2023.08.002.

756 Xiyue Wang, Sen Yang, Jun Zhang, Minghui Wang, Jing Zhang, Wei Yang, Junzhou Huang, and  
 757 Xiao Han. Transformer-based unsupervised contrastive learning for histopathological image clas-  
 758 sification. *Medical image analysis*, 81:102559, 2022.

759

760 Xiyue Wang, Junhan Zhao, Eliana Marostica, Wei Yuan, Jietian Jin, Jiayu Zhang, Ruijiang Li,  
 761 Hongping Tang, Kanran Wang, and et al. Li, Yu. A pathology foundation model for cancer  
 762 diagnosis and prognosis prediction. *Nature*, 634(8035):970–978, October 2024. ISSN 1476-  
 763 4687. Publisher: Nature Publishing Group.

764 Junxian Wu, Minheng Chen, Xinyi Ke, Tianwang Xun, Xiaoming Jiang, Hongyu Zhou, Lizhi  
 765 Shao, and Youyong Kong. Learning heterogeneous tissues with mixture of experts for gigapixel  
 766 whole slide images. In *Proceedings of the Computer Vision and Pattern Recognition Conference*  
 767 (CVPR), pp. 5144–5153, June 2025.

768 Xun Wu, Shaohan Huang, Wenhui Wang, and Furu Wei. Multi-Head Mixture-of-Experts, April  
 769 2024a. arXiv:2404.15045 [cs].

770

771 Xun Wu, Shaohan Huang, and Furu Wei. Mixture of LoRA Experts, April 2024b. arXiv:2404.13628.

772 Jinxi Xiang and Jun Zhang. Exploring low-rank property in multiple instance learning for whole  
 773 slide image classification. In *The Eleventh International Conference on Learning Representations*,  
 774 2023.

775

776 Jinxi Xiang, Xiyue Wang, Xiaoming Zhang, Yinghua Xi, Feyisope Eweje, et al. A vision–language  
 777 foundation model for precision oncology. *Nature*, 638(8051):769–778, February 2025. ISSN  
 778 1476-4687.

779 Feng Xu, Chuang Zhu, Wenqi Tang, Ying Wang, Yu Zhang, et al. Predicting Axillary Lymph  
 780 Node Metastasis in Early Breast Cancer Using Deep Learning on Primary Tumor Biopsy Slides.  
 781 *Frontiers in Oncology*, 11:759007, October 2021. ISSN 2234-943X. arXiv:2112.02222 [physics].

782

783 Hanwen Xu, Naoto Usuyama, Jaspreet Bagga, Sheng Zhang, Rajesh Rao, Tristan Naumann, Cliff  
 784 Wong, Zelalem Gero, Javier González, Yu Gu, et al. A whole-slide foundation model for digital  
 785 pathology from real-world data. *Nature*, pp. 1–8, 2024.

786 Ted Zadouri. PUSHING MIXTURE OF EXPERTS TO THE LIMIT: EXTREMELY PARAMETER  
 787 EFFICIENT MOE FOR INSTRUCTION TUNING. 2024.

788

789 Wenhui Zhu, Peijie Qiu, Xiwen Chen, Zhangsihao Yang, Aristeidis Sotiras, Abolfazl Razi, and  
 790 Yalin Wang. How effective can dropout be in multiple instance learning? *arXiv preprint*  
 791 arXiv:2504.14783, 2025.

792

793

794

795

796

797

798

799

800

801

802

803

804

805

806

807

808

809

810 A APPENDIX  
811812 A1 MULTIPLE INSTANCE LEARNING IMPLEMENTATION  
813

814 All Multiple instance learning (MIL) models are adapted according to their official implementation,  
815 using the default hyperparameters provided by their official codebases. For **MeanMIL**, we obtain  
816 a slide-level prediction by feeding the average of task-specific embeddings through a classification  
817 head. For **MaxMIL**, we feed each task-specific embedding through a classification head, and select  
818 the patch with the single highest logit as the final slide-level prediction. For the baseline of every  
819 model, we apply the following linear layer to the pretrained features,  $f(x) = \text{ReLU}(\mathbf{W}\mathbf{x})$ , where  
820  $\mathbf{W} \in \mathbb{R}^{D' \times D}$  and input features  $\mathbf{x} \in \mathbb{R}^D$ . We note that **ILRA** does not natively include an initial  
821 task-specific linear layer. Following the architecture of all other MIL examined, which apply a linear  
822 layer to the frozen patch embeddings, we introduce this linear layer prior to the ILRA aggregation  
823 step.

824  
825 A2 TRAINING DETAILS  
826

827 We train all models with the AdamW optimizer with a learning rate of  $1 \times 10^{-4}$ , a cosine decay  
828 scheduler, and mixed precision according to PyTorch’s native implementation. For datasets with a  
829 validation set, we train with a maximum of 20 epochs with an early stopping patience of 5 epochs  
830 for a minimum of 10 epochs. For datasets without a validation set, we train for 10 epochs. We use  
831 cross-entropy loss with random class-weighted sampling and a batch size of 1. For regularization,  
832 we use a weight decay of  $1 \times 10^{-5}$ , a dropout of 0.25 at every feedforward layer, and a dropout of  
833 0.1 on the features from the pretrained encoder. Experiments were performed on one NVIDIA RTX  
834 A4000.

835  
836 A3 INTERPRETABILITY  
837

838 We generate interpretable heatmaps by examining the normalized routing scores obtained in **Eq. 3.2**.  
839 We average the routing scores across all heads to obtain the slot-patch routing scores shown in **Figures 3** and **A3**. Assessment of the heatmaps and routing scores from two board-certified patholo-  
840 gists reveals that MAMMOTH learned to direct patches with similar morphology to the same slots.  
841 We note that the ability for slots to collect patches with similar morphologies is a necessary condition  
842 for allowing MAMMOTH experts to specialize in specific morphologic phenotypes. For instance, we  
843 show in **Fig. 3** that Expert 9 has likely specialized in processing patches with cells of low diagnostic  
844 importance, as one of its slots specializes in patches with lymphocytes, and another one of its patches  
845 specializes in red blood cells. Similarly, Expert 21 has three slots which specialize in aggregating  
846 both LUSC and LUAD tumor cells. We observe a similar pattern in our BRACS subtyping model,  
847 in which patches with ductal hyperplasia are closest in embedding space to slot 2 of expert 4, while  
848 patches with ductal carcinoma are strongly routed to slot 5 of expert 4. In this example, expert 4 has  
849 likely specialized in processing patches of high diagnostic relevance.

850 Lastly, the routing scores within different heads of a single slot are shown in **Fig. A7**. Interestingly,  
851 we observe that, while the highest-scoring patches routed to each head primarily reside in the tumor  
852 region, the distribution of routing scores are highly variable between heads of a single slot. These  
853 results, combined with the empirical improvement in performance when the number of heads is  
854 set to be  $\geq 16$ , suggest that our use of multiple heads allows MAMMOTH fine-grained control by  
855 partitioning the slot representations into a large number of embedding subspaces.

856  
857 A3.1 ABLATIONS  
858

859 For all ablation experiments, we train for a maximum of 10 epochs with an early stopping patience  
860 of 5 epochs, and a minimum of 5 epochs. For our experiments evaluating different configurations of  
861 experts and heads in **Section 5.3**, we roughly fix the number of *total* slots across varying numbers  
862 of experts by setting the number of slots per expert,  $S$ , to

$$863 S = \max(\lfloor (\frac{T}{E}) \rfloor, 1) \quad 0$$

864 where  $T$  is the target number of total slots, and  $E$  is the number of experts.  
 865

## 866 A4 MIXTURE OF EXPERTS IMPLEMENTATION DETAILS 867

868 For comparison with MAMMOTH, we implemented sparsely-gated MoE with softmax and sinkhorn  
 869 routing (Shazeer et al., 2017; Clark et al., 2022), sparsely-gated multihead MoE (Wu et al., 2024a),  
 870 soft MoE (Puigcerver et al., 2024), and pathology-aware MoE (Wu et al., 2025) using 5 experts  
 871 rather than 30 experts for all benchmark MoE methods in order to prevent model capacity from  
 872 overly expanding.  
 873

### 874 A4.1 SPARSE MOE 875

876 We implement Softmax MoE according to a PyTorch transcription of the official Tensorflow im-  
 877 plementation from GSHard (Lepikhin et al., 2020)(<https://github.com/lucidrains/mixture-of-experts>), using top 2 gating for each patch, alongside an expert capacity fac-  
 878 tor of 1.25 for training and 2.0 for inference to balance expert utilization. For Sinkhorn MoE, we  
 879 replace the softmax-based routing mechanism with the Sinkhorn-Knopp algorithm, as described in  
 880 (Clark et al., 2022). We use 5 experts, with each expert consisting of a  $D \times D'$ -dimensional linear  
 881 layer with ReLU activation.  
 882

### 883 A4.2 SPARSE MULTIHEAD MOE 884

885 We implement sparse multihead MoE from the official implementation (<https://github.com/yushuiwx/MH-MoE>), using 16 heads for all experiments. Following the paper’s architec-  
 886 ture, we let each expert consist of a 2-layer feedforward network with ReLU activation and set the  
 887 expert capacity to equal that of the  $D \times D'$ -dimensional sparse MoE expert layer described above,  
 888 resulting in a hidden dimension of  $\frac{HDD'}{D+D'}$ .  
 889

### 890 A4.3 SOFT MOE 891

892 We use the Soft MoE implementation from <https://github.com/lucidrains/soft-moe-pytorch>. Mirroring the hyperpameters used in MAMMOTH, we use 200 total slots  
 893 for morphological classification and 400 total slots for molecular classification tasks. We use 5  
 894 experts, with each expert consisting of a  $D \times D'$ -dimensional linear layer with ReLU activation.  
 895

### 896 A4.4 PAMOE 897

898 We use the official PaMoE implementation from <https://github.com/wjx-error/PAMoE>. Following the paper’s suggested configuration, we use 6 total experts, with 2 free ex-  
 899 perts and 4 experts initialized according to the matching organ of the evaluation task. For instance,  
 900 we use the TCGA GBMLGG initialization to evaluate on EBRAINS and GBMLGG. Similarly, we  
 901 use the TCGA BRCA initialization to evaluate on BRCA and BRACS tasks.  
 902

### 903 A4.5 DATASETS 904

905 We briefly describe the datasets that were used to evaluate MAMMOTH.  
 906

#### 907 A4.5.1 MORPHOLOGICAL SUBTYPING 908

909 **EBRAINS** (Roetzer-Pejrimovsky et al., 2022): We perform coarse-grained (12 classes) and fine-  
 910 grained (30 classes) classification of brain tumor subtypes. The dataset consisted 2,319 Hematoxylin  
 911 and Eosin (H&E) Formalin-fixed and paraffin-embedded (FFPE) Whole Slide Images (WSIs). We  
 912 use label-stratified train/val/test splits (50% / 25% / 25%) provided by UNI (Chen et al., 2024a). We  
 913 evaluate performance using balanced accuracy.  
 914

915 **NSCLC**: The non-small cell lung carcinoma (NSCLC) subtyping task was a binary classifica-  
 916 tion problem for distinguishing lung adenocarcinoma (LUAD) and lung squamous cell carcinoma  
 917 (LUSC). The training data consisted of publicly available H&E WSIs from TCGA ( $n = 1,041$

918 slides). We used 5-fold site-stratified cross validation on the TCGA dataset for training and internal  
 919 validation, and evaluated the trained model on two external datasets: the Clinical Proteomic Tumor  
 920 Analysis Consortium (CPTAC,  $n = 1,091$  slides) and the National Lung Screening Trial (NLST,  
 921  $n = 1,008$  slides) (Campbell et al., 2016; Satpathy et al., 2021; Gillette et al., 2020). We report  
 922 average AUROC across the five folds for performance on this binary classification task. We report  
 923 the performance averaged across the TCGA, NLST, and CPTAC datasets in **Table 1**.

924 **PANDA** (Bulcen et al., 2022; 2020): We used prostate cancer core needle biopsies ( $n = 10,616$ )  
 925 from the Prostate Cancer Grade Assessment (PANDA) challenge to perform 6-class classification  
 926 according to the prostate cancer grade. We use the same train/val/test folds (80% / 10 % / 10%) as  
 927 UNI, and evaluate using Cohen’s quadratic weighted Kappa  $\kappa$  metric.

928 **BRACS** (Brancati et al., 2021): The BRACS subtyping task consisted of a 3-class coarse-grained  
 929 classification task to distinguish benign, malignant, and atypical breast carcinoma H&E slides, as  
 930 well as a fine-grained 7-class classification task that classifies benign tumors into three subtypes,  
 931 atypical tumors into two subtypes, and malignant tumors as two subtypes. We use the official  
 932 train/val/test folds (72% / 12% / 16%), with the same folds for both coarse- and fine-grained tasks.  
 933 We evaluate performance using balanced accuracy.

#### 935 A4.5.2 BIOMARKER PREDICTION

936 **Lung cancer biomarkers**: We conduct 5-fold cross-validation on H&E-stained WSIs for the binary  
 937 classification task of predicting mutation status of TP53, KRAS, STK11, and EGFR in TCGA lung  
 938 cancer cases ( $n = 524$  slides) (Cancer Genome Atlas Research Network et al., 2015), with each task  
 939 site- and label-stratified into an approximate train/val/test splits (60% / 20% / 20%). We evaluate  
 940 performance using AUROC.

941 **Breast cancer biomarkers**: We conduct 5-fold cross-validation for the binary classification tasks  
 942 of predicting mutation status of ER, PR, HER2, and PIK3CA on H&E-stained WSIs from TCGA  
 943 breast cancer (BRCA) cases ( $n = 1,034$ ), each site-stratified and label-stratified in an approximate  
 944 train/val/test splits (60% / 20% / 20%). Additionally, we perform 10-fold cross-validation on breast  
 945 cancer core needle biopsies (BCNB,  $n = 1,058$ ) (Xu et al., 2021)) for ER, PR, and HER2. We  
 946 evaluate performance using AUROC.

947 **GBMLGG mutational subtyping** (Brennan et al., 2013; Roetzer-Pejrimovsky et al., 2022): These  
 948 tasks include binary coarse-grained mutation prediction of IDH1 status using the TCGA GBMLGG  
 949 dataset (1,123 slides), and 5-class fine-grained histomolecular subtyping. The 5-class histomolec-  
 950 ular subtyping task was separated into the categories of Astrocytoma, IDH1-mutant, Glioblas-  
 951 toma, IDH1-mutant, Oligodendrogloma, IDH1-mutant and 1p/19q codeleted, Astrocytoma, IDH1-  
 952 wildtype, and Glioblastoma, IDH1-wildtype. For training and evaluation of both tasks, we use the  
 953 UNI splits, which label-stratified TCGA-GBMLGG into a train/val/test fold with a 47:22:31 ratio.  
 954 Additionally, we perform external validation on the held-out EBRAINS cohort ( $n = 873$  slides) for  
 955 the cases with known IHD1 status. We evaluate GBMLGG-C with AUROC, and GBMLGG-F with  
 956 balanced accuracy.

#### 957 A4.6 SOFT MOE PATCH OUTPUT FORMULATION

958 Here, we describe the process for returning updated patch representations according to Soft  
 959 MoE (Puigcerver et al., 2024) for the model design ablation **MAMMOTH output**. Let  $\{\bar{x}_i\}_{i=1}^N$   
 960 be the set of patch embeddings and  $\{\mathbf{z}_j^{(k)}\}_{j,k=1}^{S,E}$  be the slot outputs for MAMMOTH across  $H$  heads,  
 961  $E$  experts, and  $S$  slots per expert. The linear weights are normalized weighted combination over the  
 962 routing scores of each slot, where for any head, the weight between patch  $i$  and the output of expert  
 963  $k$ , slot  $j$  is given by:

$$\alpha_{j,i}^{(k)} = \frac{\exp(\langle \bar{x}_i, \mathbf{z}_j^{(k)} \rangle)}{\sum_{k=1}^E \sum_{j=1}^S \exp(\langle \bar{x}_i, \mathbf{z}_j^{(k)} \rangle)} \quad 0$$

964 and the updated representation  $\hat{x}_i$  is the weighted combination

$$\hat{x}_i = \sum_{j,k=1}^{S,E} \alpha_{j,i}^{(k)} \mathbf{z}_j^{(k)} \quad 0$$

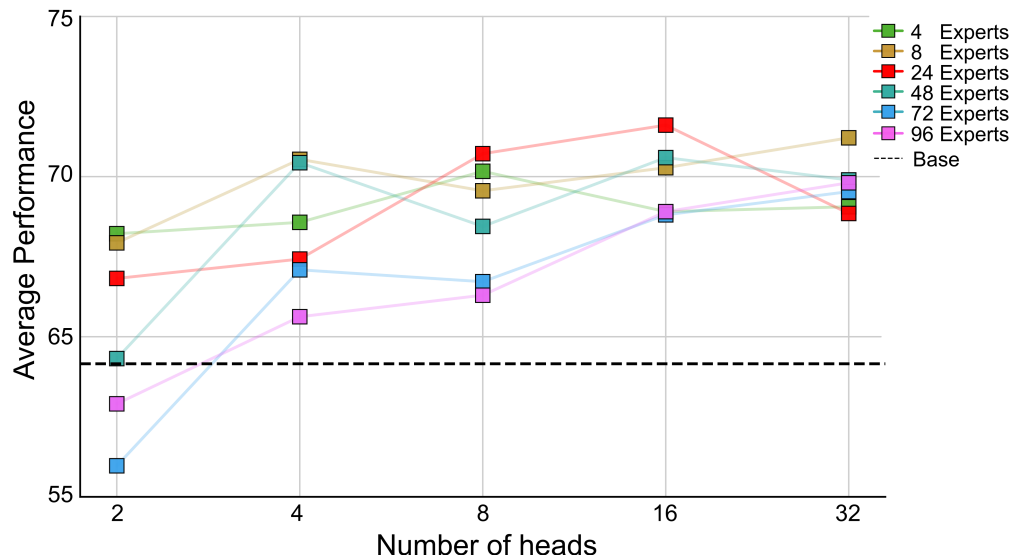
972 A5 INTERPRETABILITY AND VISUALIZATION PROTOCOLS  
973974 A5.1 DETERMINISTIC EXPERT-SLOT SELECTION PROTOCOL  
975976 To ensure rigorous interpretability of MAMMOTH, we implemented a fully deterministic protocol to  
977 identify and visualize the semantic specialization of expert slots. This process aligns histological  
978 concepts with model routing behaviors through the following steps:

979

1. **Key Term Generation:** A set of  $N = 30$  organ-specific histologic terms was generated  
980 using the Gemini 2.5 Pro large language model.
2. **Vision-Language Embedding:** Text embeddings for each histologic term,  $x_{\text{text}}$ , were gen-  
981 erated using the MUSK vision-language pathology foundation model Xiang et al. (2025).  
982 Similarly, patch-level image embeddings,  $X = \{x_i\}_{i=1}^N$ , were extracted for all Whole Slide  
983 Images (WSIs) in the evaluation dataset using the MUSK image encoder.
3. **Semantic Relatedness Scoring:** For every patch in the dataset, we computed a “related-  
984 ness” score to each histologic term via the cosine similarity between the patch embedding  
985 and the term embedding:

$$S(p, t) = \cos(x_i, x_{\text{text}}^{(t)}) \quad (0)$$

4. **Routing-Weighted Attribution:** To determine the specialization of specific expert slots, we calculated a weighted attribution score. For each expert-slot pair and histologic term, we computed the sum of the semantic relatedness scores ( $S$ ), weighted by the router’s probability assignment (routing score) of that patch to the specific slot.
5. **Selection and Visualization:** For each histologic term, the expert-slot pair yielding the highest accumulated weighted score was selected for visualization.

997 A5.2 ADDITIONAL VISUALIZATIONS  
9981017 Figure A1: **Performance with varying heads and experts.** ABMIL and TransMIL performance  
1018 with MAMMOTH and varying numbers of heads and experts, averaged across EBRAINS-C and  
1019 3-fold cross-validation of LUNG TP53 and BRCA HER2. Performance is most stable with interme-  
1020 diate number of experts and high number of heads.  
1021

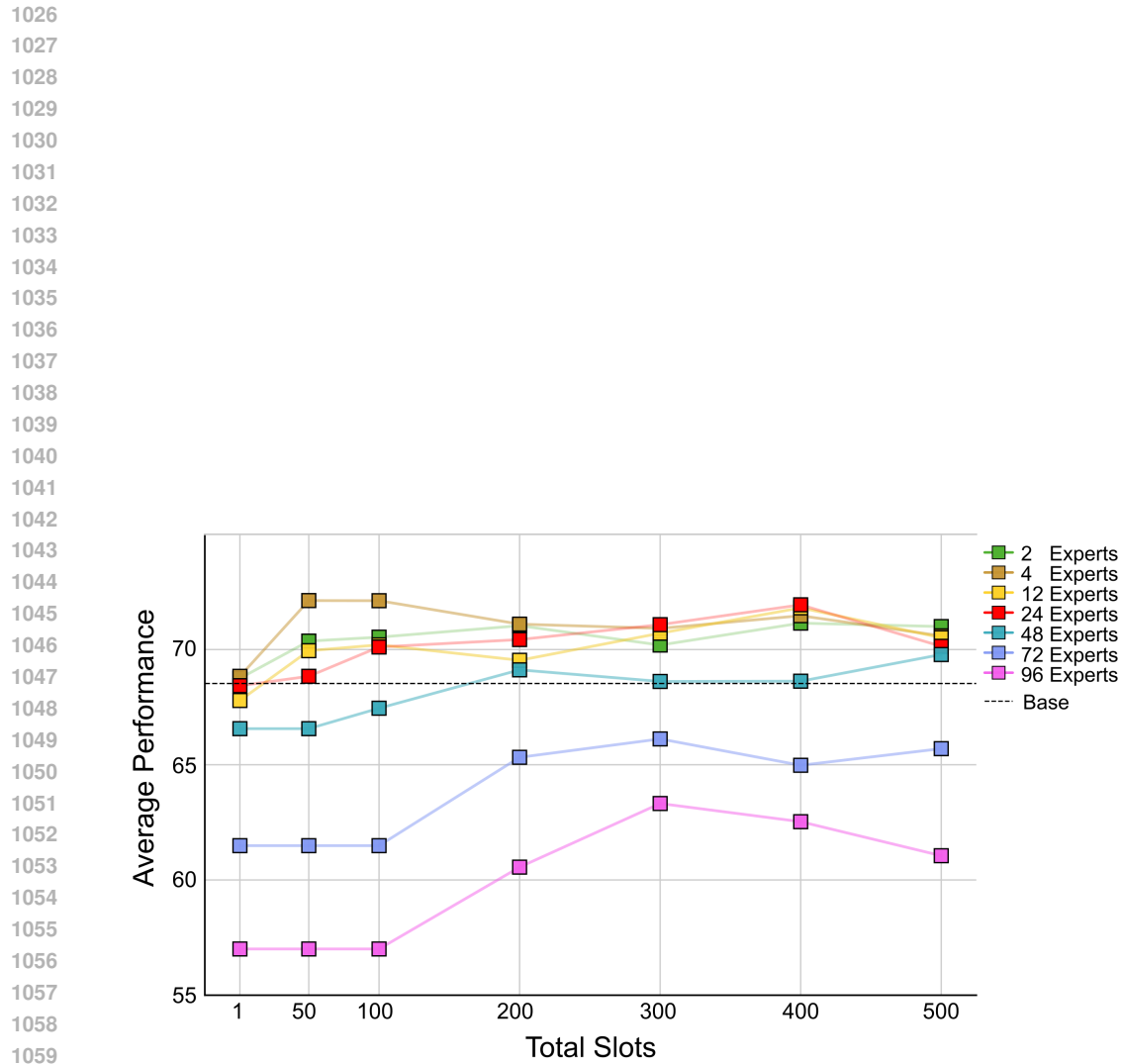


Figure A2: **Performance with varying total slots.** ABMIL trained on EBRAINS-F with varying experts and total slots. Results are averaged across head counts  $H \in \{2, 4, 8, 16, 32\}$ . Slots per expert are set as  $S = \lfloor \frac{\text{Total Slots}}{E} \rfloor$ . Low expert counts ( $E \in \{2, 4\}$ ) reach highest performance with low total slots, while high expert counts ( $E \in \{2, 4\}$ ) reach highest performance with 200-400 total slots.

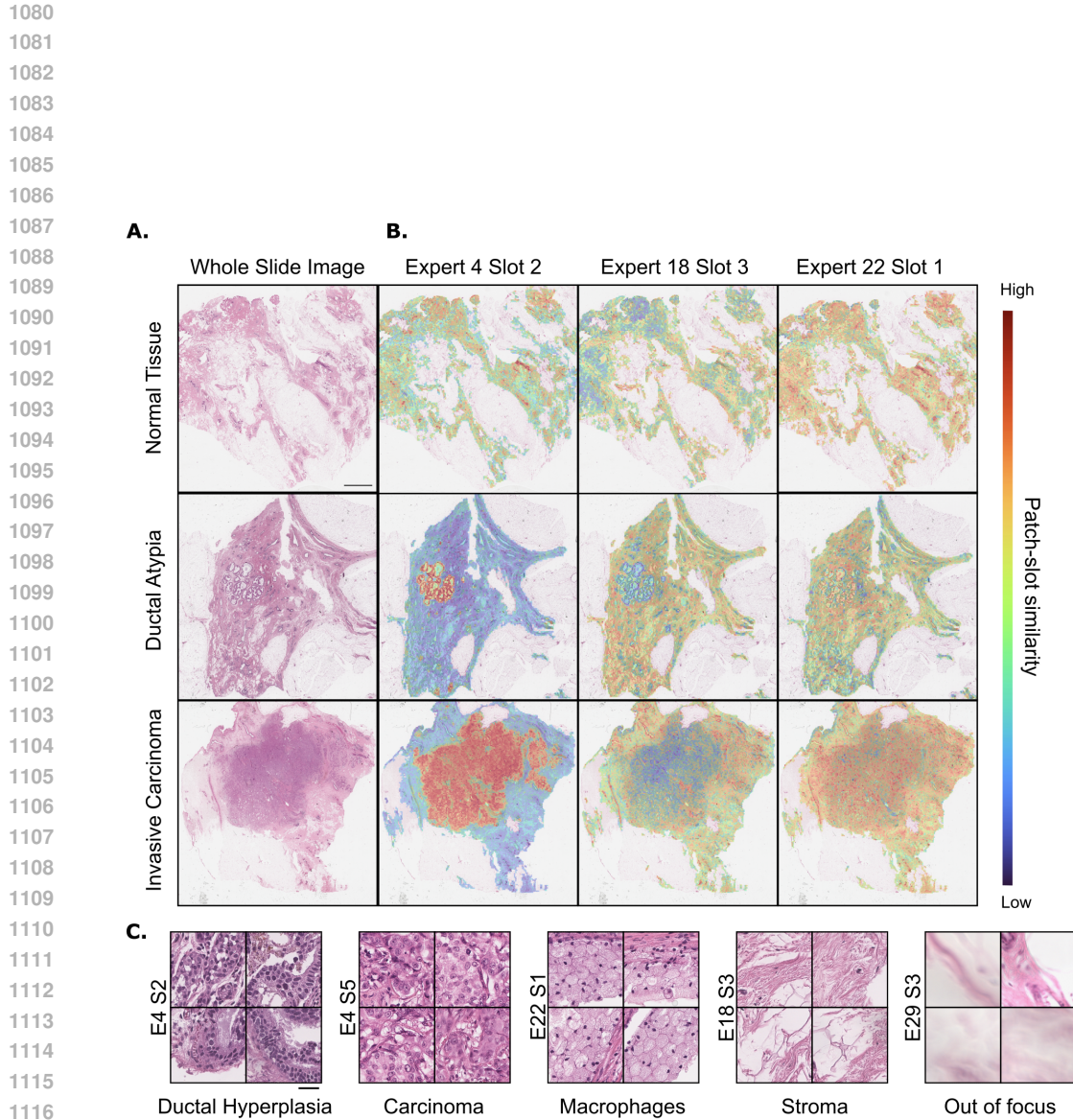


Figure A3: **Slot routing scores on BRACS subtyping.** Slot routing scores for an ABMIL model trained on BRACS coarse-grained subtyping. **(A)** Whole slide image for normal tissue, ductal atypia, and invasive carcinoma. **(B)** Softmax-normalized routing scores between each patch and slots of different experts. Expert 4 Slot 2 (E4 S2) places high routing scores on the key diagnostic regions for normal tissue, ductal atypia, and invasive carcinoma. Stroma had high routing scores allocated to Expert 18 Slot 3. Expert 22 Slot 1 (E22 S1) had diffusely distributed routing scores throughout the tissue. **(C)** Patches from slides in **(A)** with the highest routing scores for select expert-slot pairs. Top patches routed to different slots have clear morphological phenotypes: the top patches for E4 S2 contain diagnostically relevant cells with ductal hyperplasia, and the top patches for E4 S5 contains invasive carcinoma, while the top patches for E18 S3 consist primarily of stroma, those of E22 S1 consist of macrophages, and those of E29 S3 consist of blurry tissue. Scale bars: **A-B.** 500  $\mu$ m, **C.** 20  $\mu$ m.

1134  
 1135  
 1136  
 1137  
 1138  
 1139 **Glioblastoma and Lower Grade Glioma**  
 1140  
 1141  
 1142  
 1143  
 1144  
 1145  
 1146  
 1147  
 1148  
 1149  
 1150  
 1151  
 1152  
 1153  
 1154  
 1155  
 1156  
 1157  
 1158  
 1159  
 1160  
 1161  
 1162  
 1163  
 1164  
 1165  
 1166  
 1167  
 1168  
 1169  
 1170  
 1171  
 1172  
 1173  
 1174  
 1175  
 1176  
 1177  
 1178  
 1179  
 1180  
 1181  
 1182  
 1183  
 1184  
 1185  
 1186  
 1187

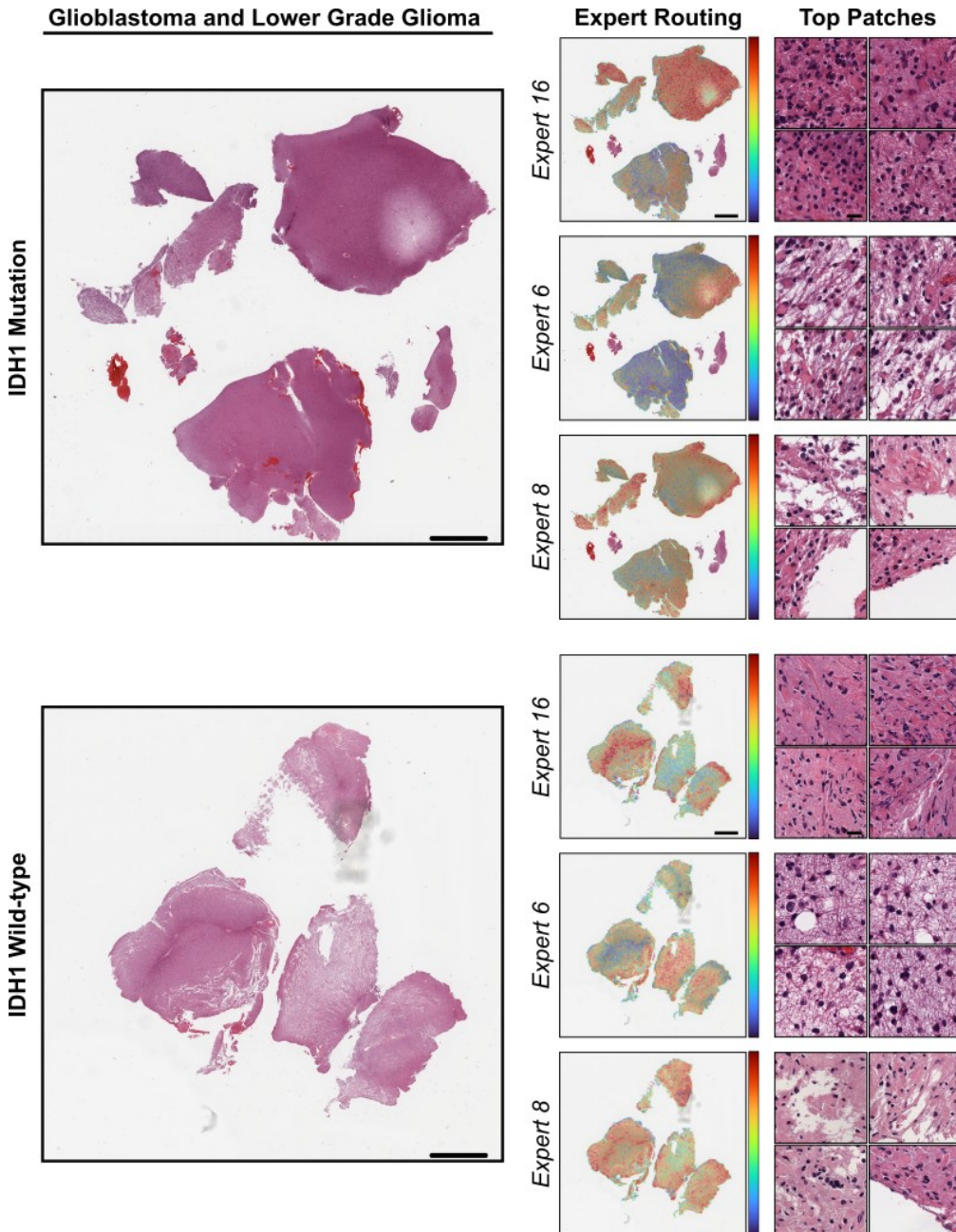


Figure A4: **Expert routing scores in GBMLGG C.** Total routing scores from each patch to each expert, averaged across the slots and heads of each expert. In both mutant and wild-type IDH1 WSIs, we find that Expert 16 specializes in dense tumor cells with tightly-packed neuropil. Expert 6 specializes in dense tumor cells with loose neuropil. Expert 8 specializes in diffuse tumor cells with loose neuropil. Scale bars: WSI; 500  $\mu$ m, Expert Routing; 500  $\mu$ m, Top Patches; 10  $\mu$ m

1188  
 1189  
 1190  
 1191  
 1192  
 1193 **Breast Cancer**  
 1194  
 1195  
 1196  
 1197  
 1198  
 1199  
 1200  
 1201  
 1202  
 1203  
 1204  
 1205  
 1206  
 1207  
 1208  
 1209  
 1210  
 1211  
 1212  
 1213  
 1214  
 1215  
 1216  
 1217  
 1218  
 1219  
 1220  
 1221  
 1222  
 1223  
 1224  
 1225  
 1226  
 1227  
 1228  
 1229  
 1230  
 1231  
 1232  
 1233  
 1234  
 1235  
 1236  
 1237  
 1238  
 1239  
 1240  
 1241

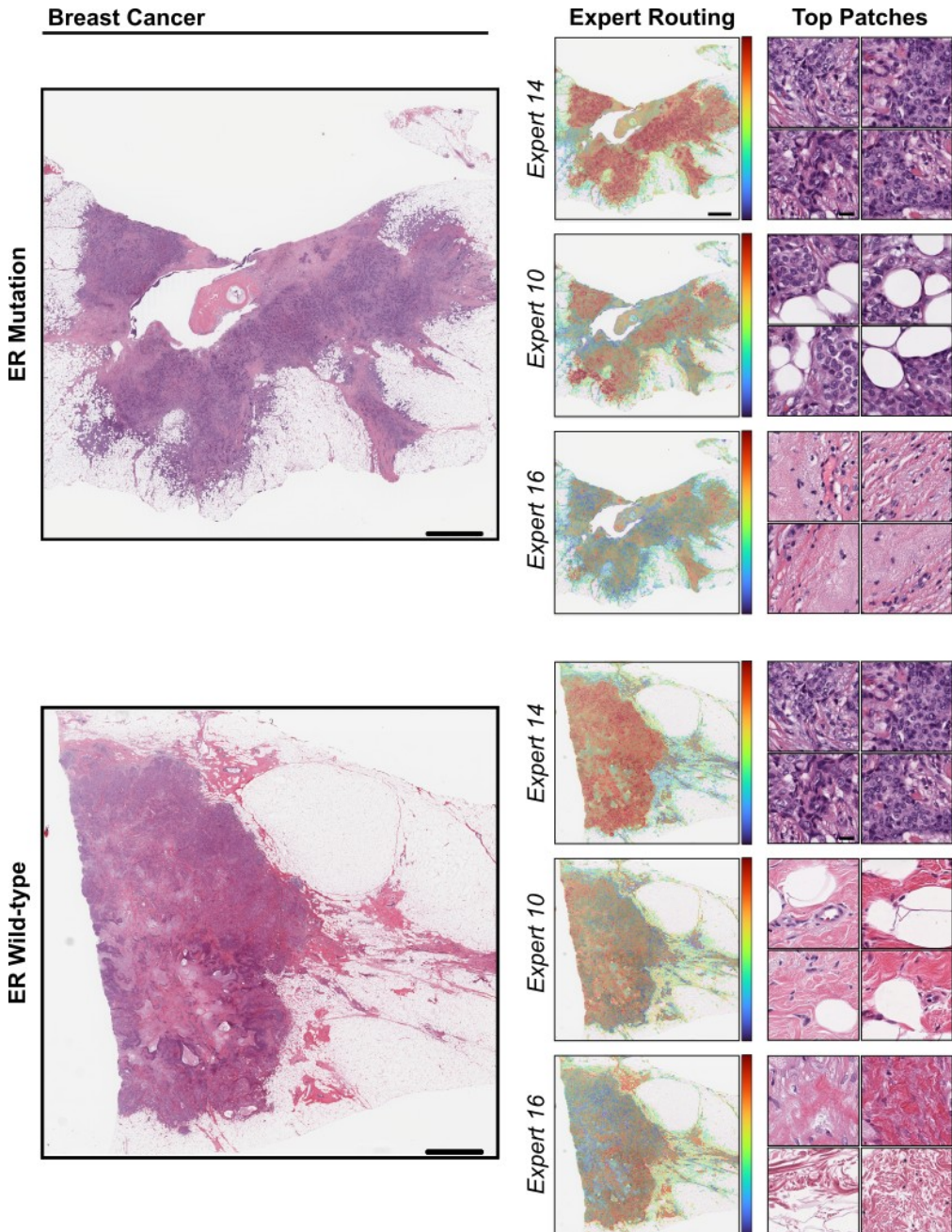
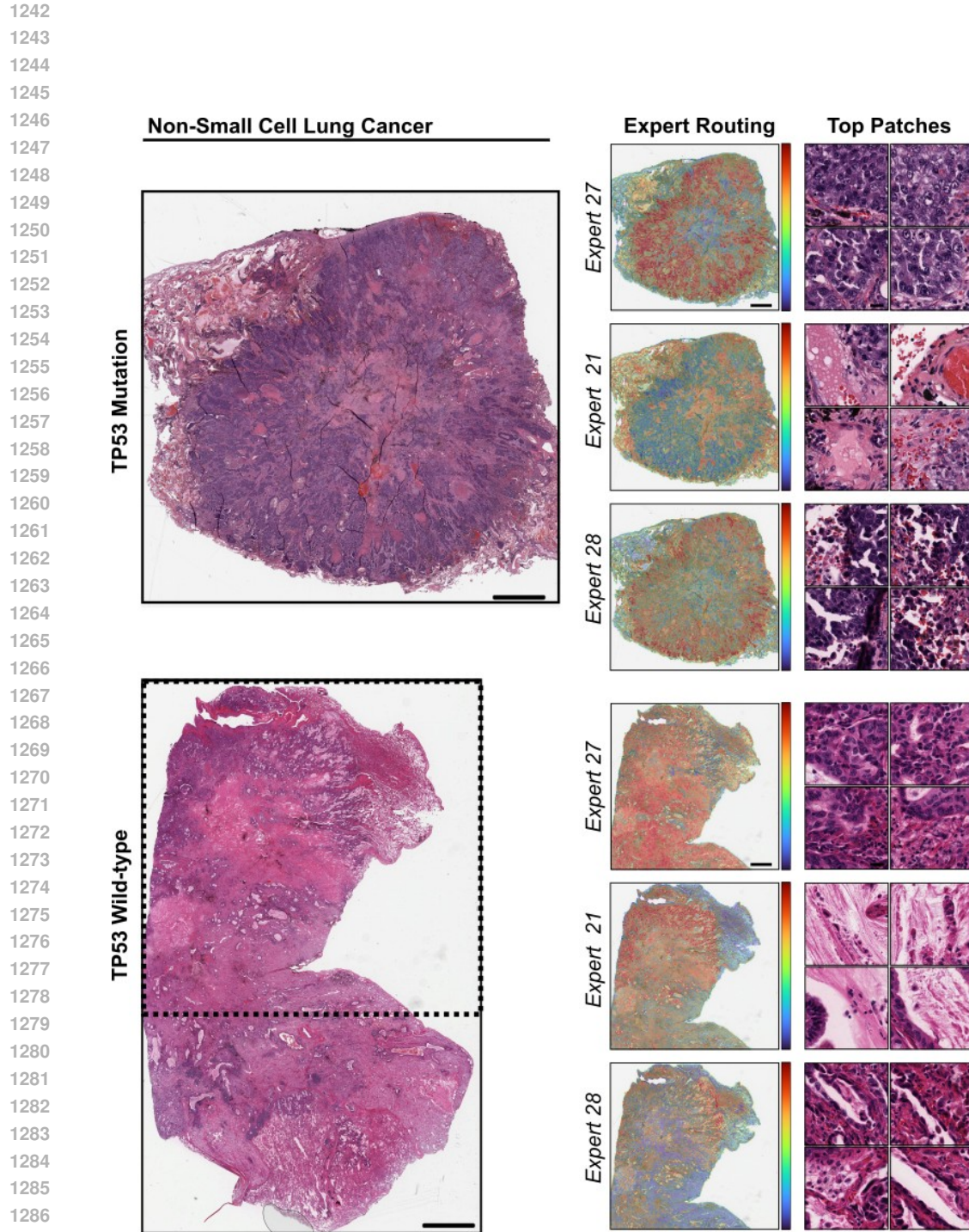
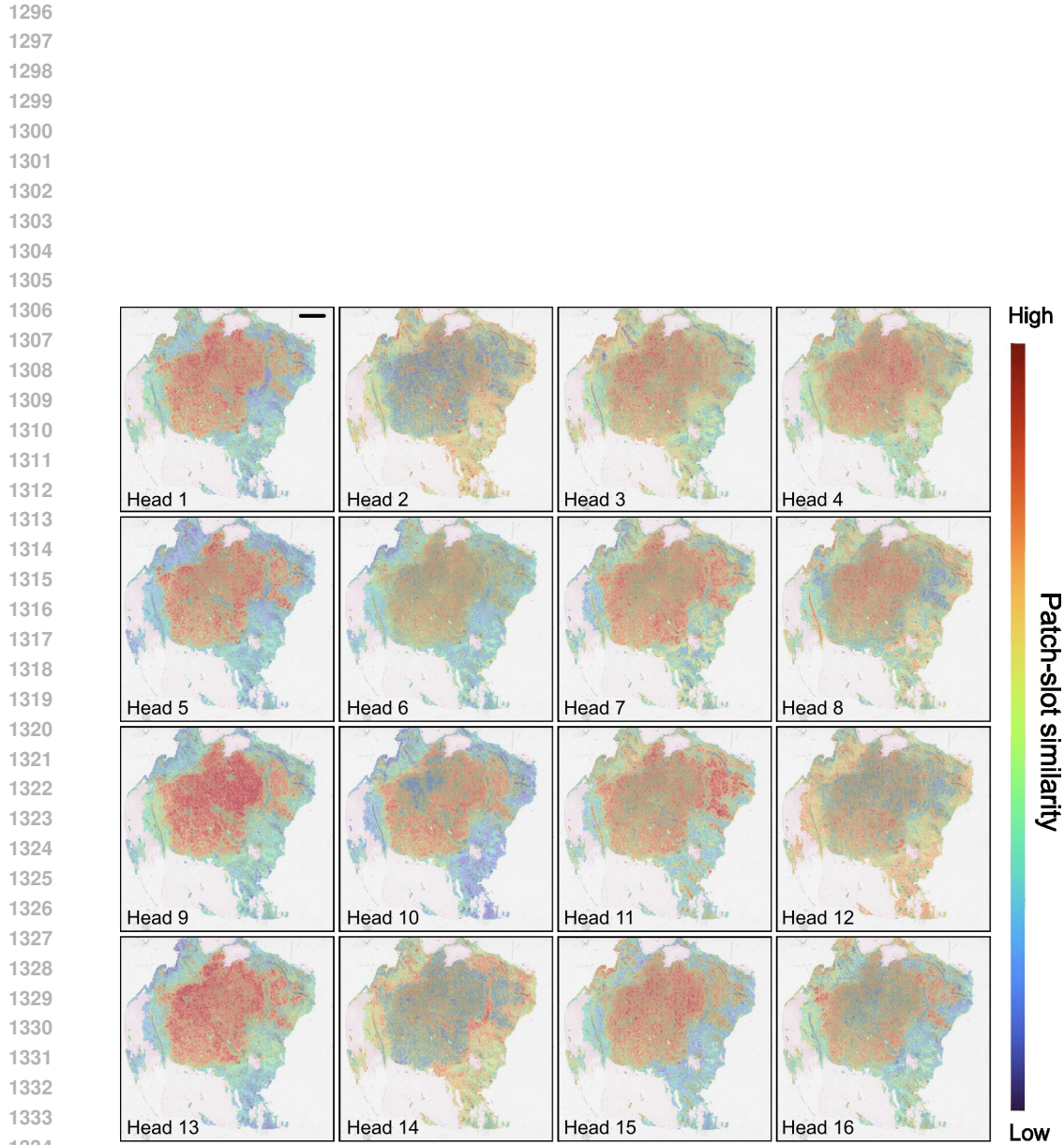


Figure A5: **Expert routing scores in BRCA ER.** Total routing scores from each patch to each expert, averaged across the slots and heads of each expert. In both mutant and wild-type IDH1 WSIs, we find that Expert 14 specializes in patches rich in tumor cells, Expert 10 specializes in adipocytes in conjunction with tumor cells, and Expert 16 specializes in connective tissue. Scale bars: WSI; 500  $\mu$ m, Expert Routing; 500  $\mu$ m, Top Patches; 10  $\mu$ m



1287 **Figure A6: Expert routing scores in LUNG TP53.** Total routing scores from each patch to each  
 1288 expert, averaged across the slots and heads of each expert. We find that Expert 27 specializes in  
 1289 processing patches rich in tumor cells. Expert 21 specializes in background structures such as blood  
 1290 vessels, lymphatics, and connective tissue. Expert 28 specializes in tumor cells around or forming  
 1291 spaces. Dashed box indicates ROI displayed in Expert Routing. Scale bars: WSI; 500  $\mu$ m, Expert  
 1292 Routing; 500  $\mu$ m, Top Patches; 10  $\mu$ m  
 1293

1294  
 1295



1335 **Figure A7: Routing scores on BRACS subtyping across heads of one slot.** Routing scores for a  
 1336 single slot (Expert 4 Slot 2) across each head of a 16-head MAMMOTH ABMIL model trained on  
 1337 BRACS coarse-grained subtyping. Each image corresponds to the routing scores within one head.  
 1338 The image shown corresponds to invasive carcinoma. We observe that while the attention scores  
 1339 are routed to the same general tumor area between different heads, the distribution of attention scores  
 1340 varies between heads, suggesting that different heads may attend to different details of the tumorous  
 1341 region. Scale bars: 500  $\mu$ m.  
 1342  
 1343  
 1344  
 1345  
 1346  
 1347  
 1348  
 1349

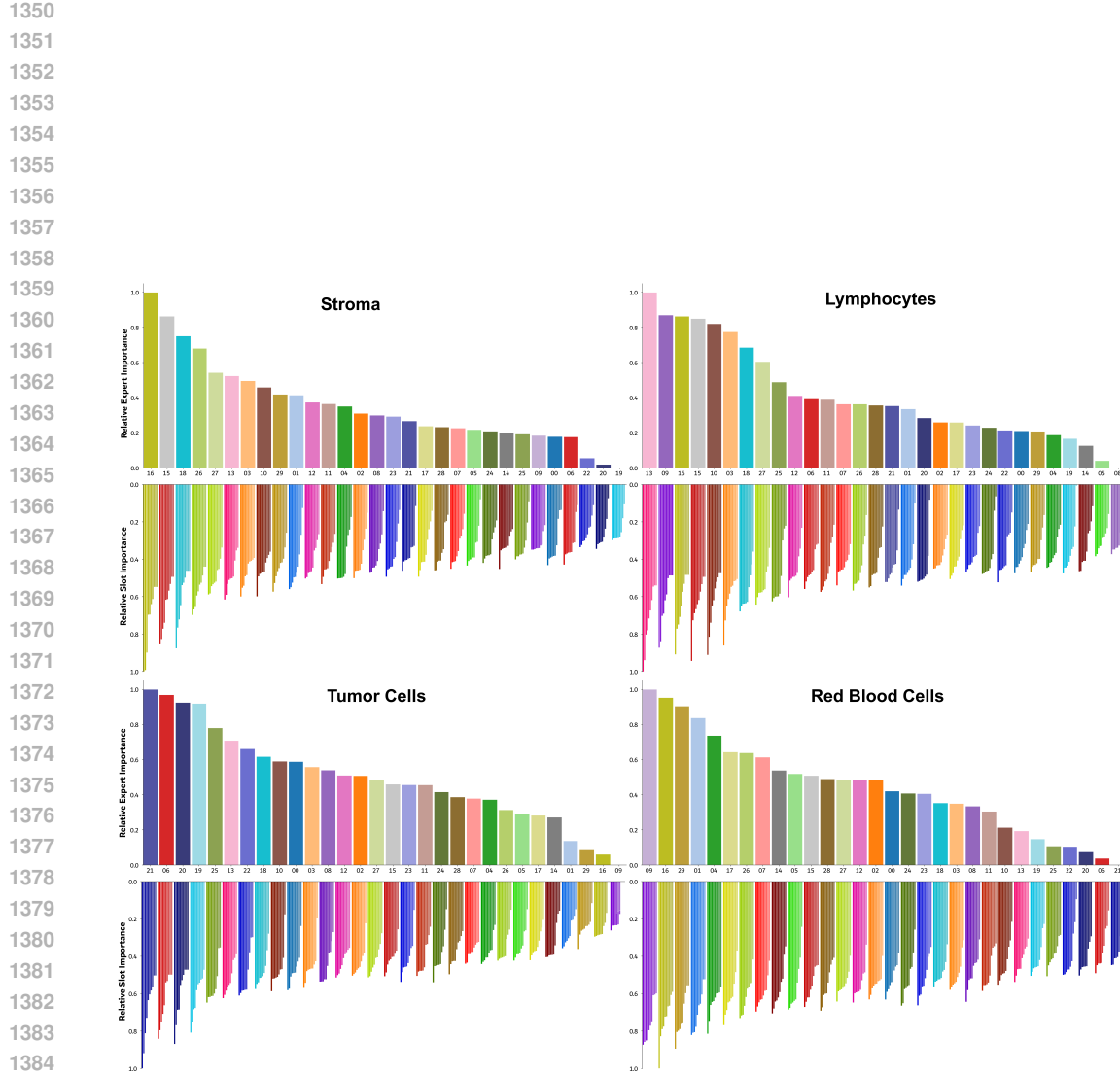


Figure A8: **Quantifying expert specialization via vision–language scoring.** To decode expert roles, we annotated all NSCLC patches with **term-relevance scores** based on the cosine similarity between image embeddings and text concepts like *stroma* or *tumor cells* using the MUSK foundation model. We then calculated the **Relative Slot Importance** for each concept by weighting these MUSK relevance scores with the slot’s own routing weights across all patches. Finally, **Relative Expert Importance** represents the aggregated importance of all slots assigned to a given expert. The distribution highlights distinct specialization: Experts 16, 13, 21, and 9 demonstrate high attention to stroma, lymphocytes, tumor cells, and red blood cells, respectively. Furthermore, slots within the same expert display highly correlated routing patterns, indicating strong intra-expert synchrony. Representative patches with the highest routing scores were validated by pathologists to confirm alignment with these histological concepts. The slot with the highest relative slot importance is selected for downstream visualization with attention heatmaps.

1397  
1398  
1399  
1400  
1401  
1402  
1403

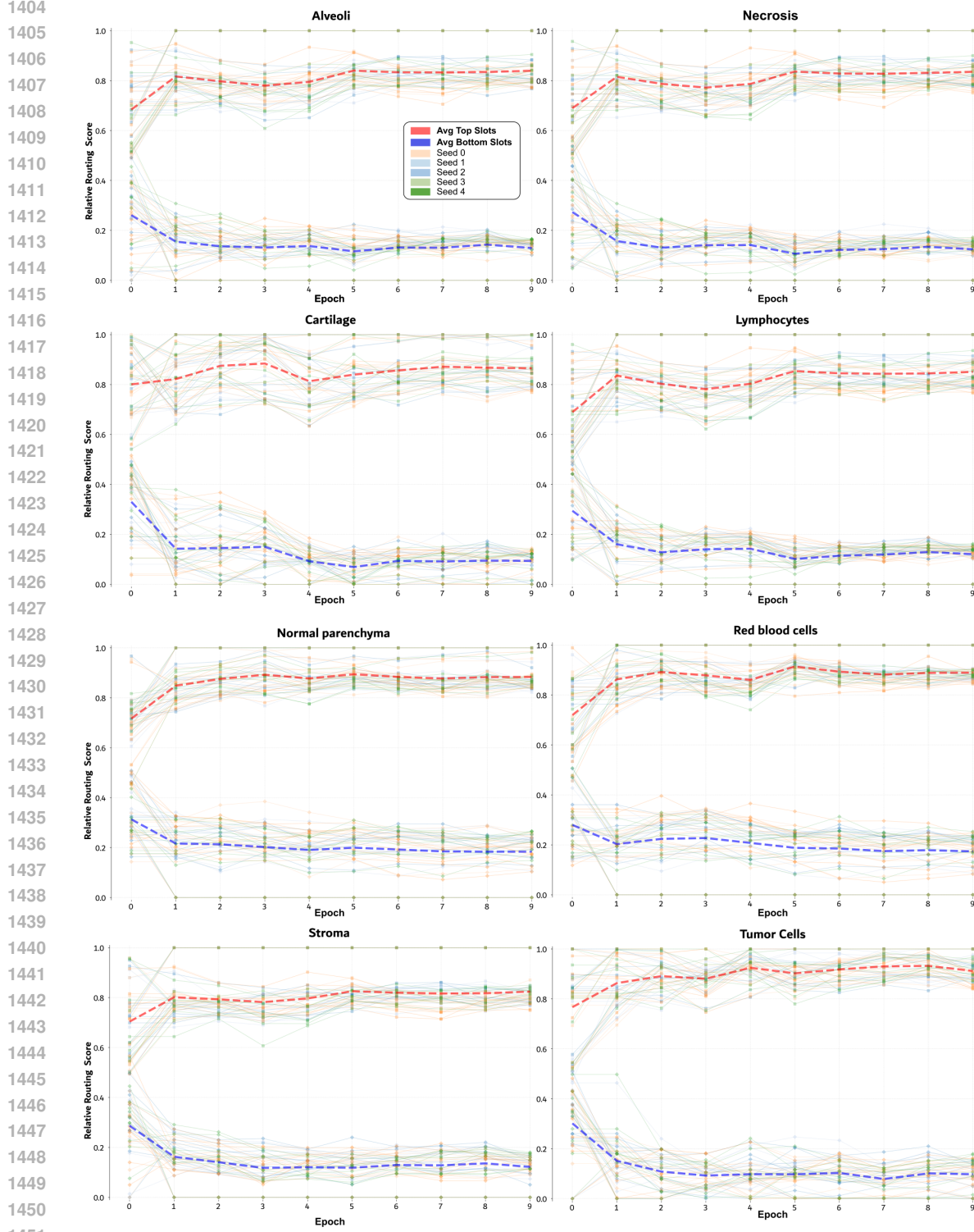


Figure A9: **Emergent specialization during training.** We tracked the **Relative Routing Scores**, derived from MUSK term-relevance scores weighted by routing probability, across training epochs of NSCLC subtyping. The plots display the trajectories of the top 10 most relevant slots (red) and least relevant slots (blue), identified at model convergence and traced back to initialization. Data is averaged over five random seeds with normalization across epochs and seeds. Dashed lines indicate group averages. We observe that **concept-aligned slots exhibit higher relative importance even at initialization** ( $t = 0$ ), followed by a sharp increase and stabilization within the first epoch. This suggests that MAMMOTH’s specialization is partly driven by differential routing at initialization, which is rapidly reinforced during early training.

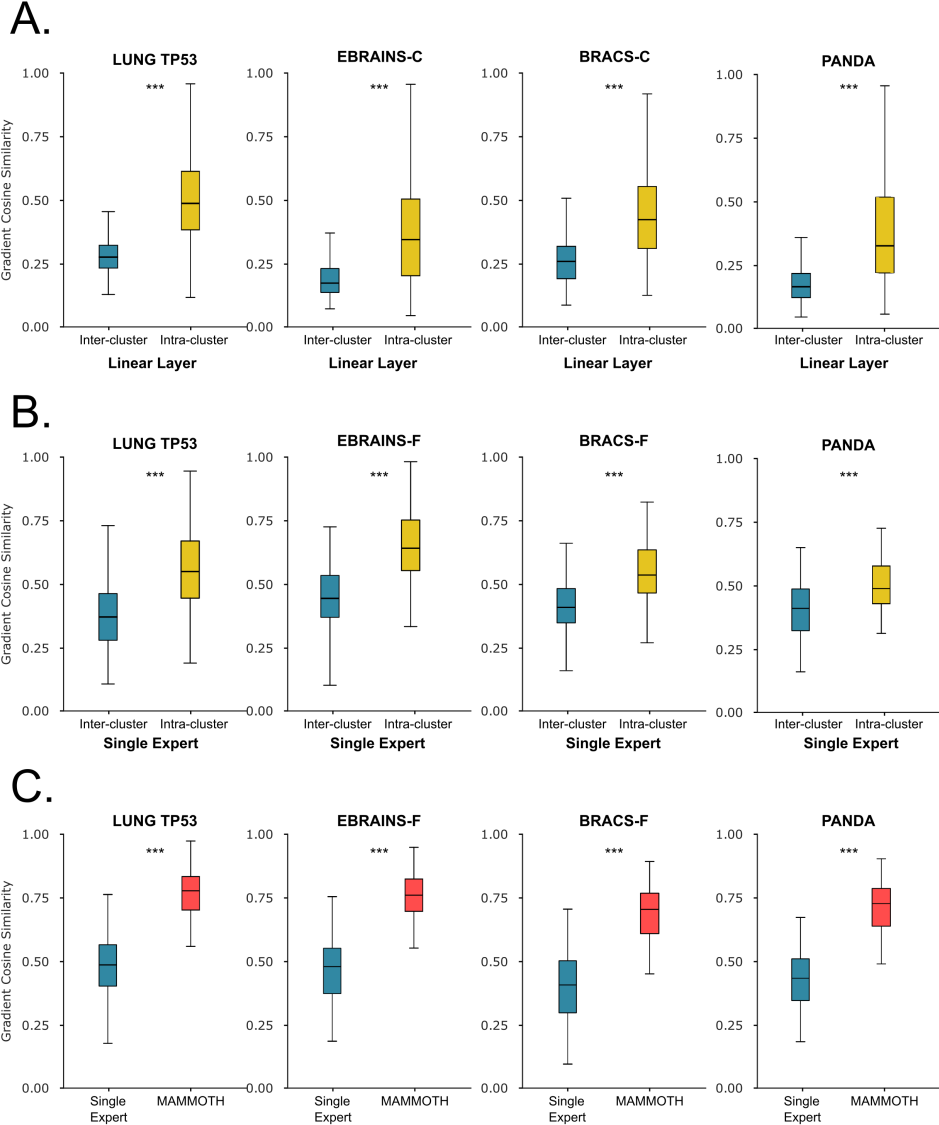
1458  
1459  
1460  
1461  
1462  
1463  
1464

Figure A10: **Similarity of gradient updates between instances for the task-specific layer.** Cosine similarity of gradient updates with respect to instances at **A.** the standard linear layer and **B.** MAMMOTH with a single expert. **Instances from different clusters consistently yield more dissimilar gradient updates compared to instances from the same cluster**, which we call *Instance Gradient Interference (IGI)*. **C.** Comparison of gradient similarity between all instances with a single expert and 30 experts (MAMMOTH). MAMMOTH with a single expert is used as a baseline to isolate the effect of using multiple experts. When instances are routed to different experts, the internal gradient updates become more homogenous compared to the single-expert baseline. Gradients were measured at epoch 1 of training across 100 slides. Significance markers indicate a one-sided t-test: \* $p < 0.05$ , \*\* $p < 0.01$ , \*\*\* $p < 0.001$

1509  
1510  
1511

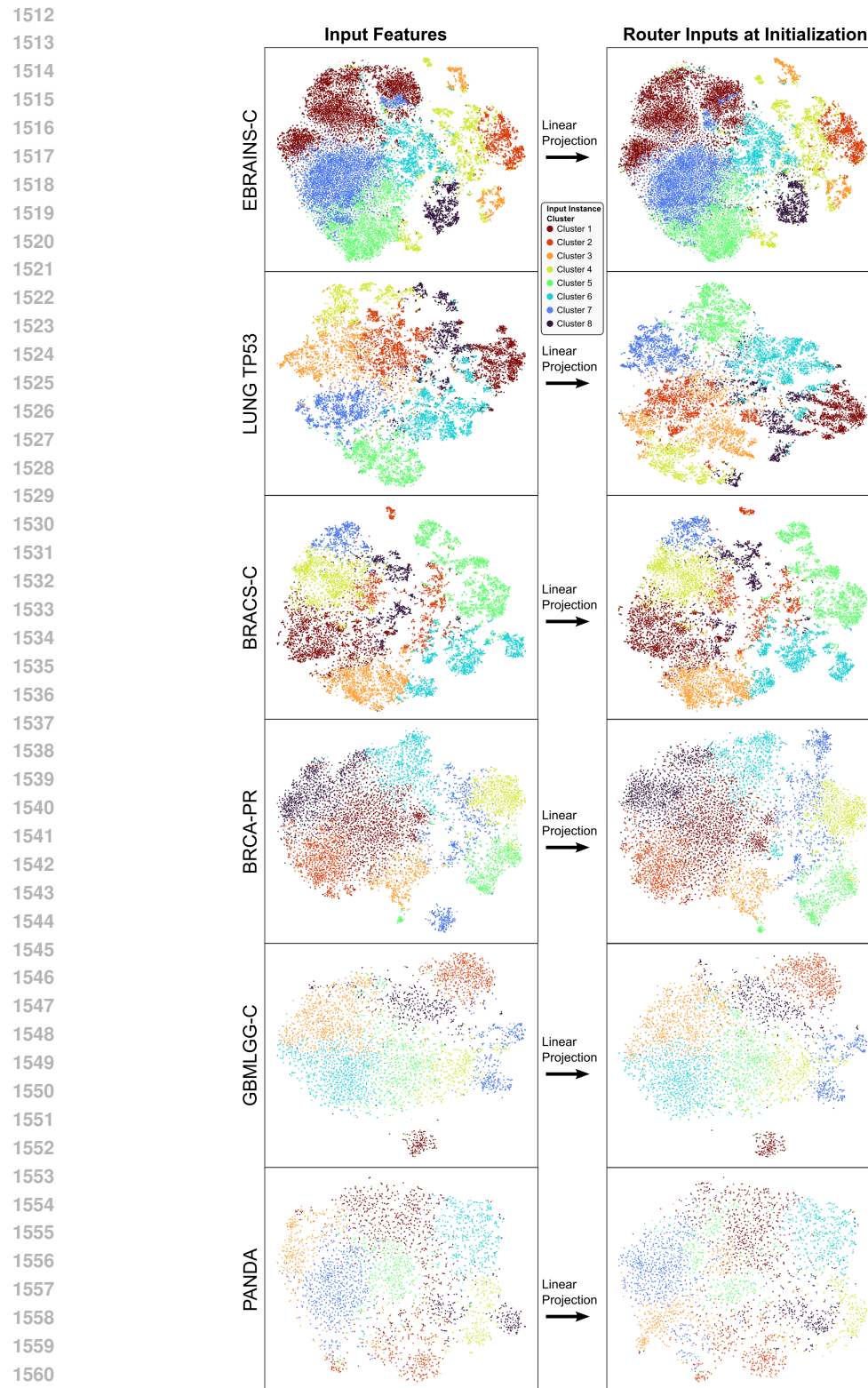


Figure A11: **Preservation of clusters after linear projection.** t-SNE of instance features at input and after MAMMOTH linear projection via  $\mathbf{W} \in \mathbb{R}^{(P \cdot H) \times D}$  at the start and end of training. Instances are colored according to K-means clustering of the *input features* with  $K = 8$ . The linear projection preserves instance clusters encoded by the pathology foundation model, both at random initialization and at model convergence.

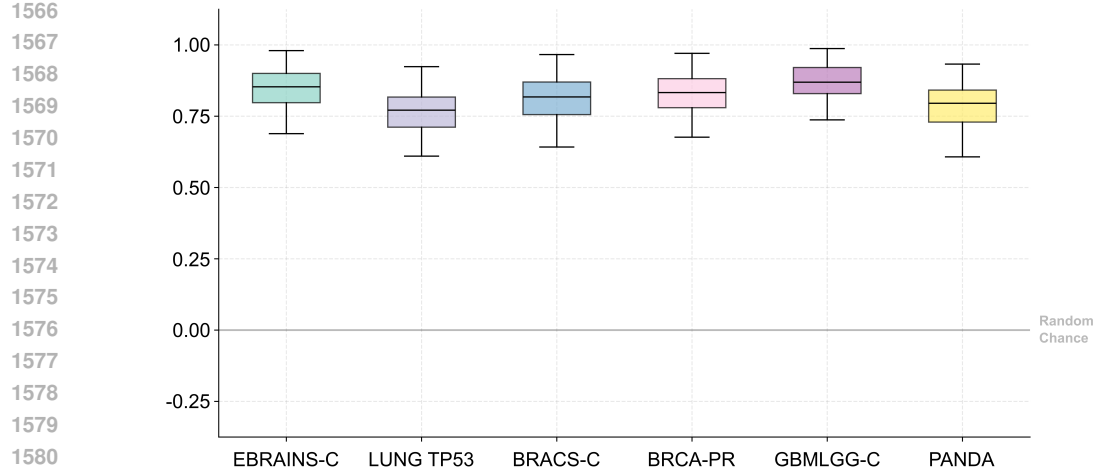


Figure A12: **Quantitative assessment of cluster preservation via Adjusted Rand Index (ARI).** We quantify instance-level similarity after randomly-initialized linear projection, utilizing K-means cluster assignments ( $K = 8$ ) of the input features as reference labels. An ARI score of 0.0 indicates random assignment. Across all 6 evaluated tasks, our method consistently achieves ARI scores exceeding 0.75, demonstrating that the randomly initialized linear projection reliably preserves semantic structure encoded by the pathology foundation model.

Table A1: **Performance on different encoders.** Performance of MIL models on different encoders. Models were trained with 30 experts, 16 heads, and 6 slots per expert. Addition of MAMMOTH consistently leads to improved performance over the original MIL models across all three encoders. Balanced accuracy is reported.

Task	State	ABMIL			CLAM			TransMIL			Max		
		GigaPath	Musk	Virchow	GigaPath	Musk	Virchow	GigaPath	Musk	Virchow	GigaPath	Musk	Virchow
EBRAINS-C	Base	85.9	85.5	83.4	87.0	79.1	83.9	87.3	80.2	85.5	83.9	82.8	83.3
	$C = 12$	83.6	84.2	87.9	89.9	88.8	87.1	87.8	82.3	86.6	87.2	82.7	83.6
	(Bal. Acc.) $\Delta$	<b>-2.3</b>	<b>-1.3</b>	<b>+4.5</b>	<b>+2.9</b>	<b>+9.7</b>	<b>+3.2</b>	<b>+0.5</b>	<b>+2.1</b>	<b>+1.1</b>	<b>+3.3</b>	<b>-0.1</b>	<b>+0.3</b>
EBRAINS-F	Base	67.9	67.1	65.5	70.5	68.3	69.8	67.6	64.7	66.7	61.1	61.0	65.5
	$C = 30$	69.7	69.5	70.9	71.6	72.1	72.3	71.8	62.9	65.5	70.6	65.7	68.0
	(Bal. Acc.) $\Delta$	<b>+1.8</b>	<b>+2.4</b>	<b>+5.4</b>	<b>+1.1</b>	<b>+3.8</b>	<b>+2.5</b>	<b>+4.2</b>	<b>-1.8</b>	<b>-1.2</b>	<b>+9.5</b>	<b>+4.7</b>	<b>+2.5</b>
BRACS-C	Base	69.4	60.9	73.5	58.9	53.7	49.3	59.3	65.5	63.3	57.5	55.5	56.3
	$C = 3$	69.2	70.7	71.8	66.9	73.0	72.3	70.5	66.6	66.9	60.4	57.0	67.2
	(Bal. Acc.) $\Delta$	<b>-0.2</b>	<b>+9.8</b>	<b>-1.7</b>	<b>+8.0</b>	<b>+19.3</b>	<b>+23.0</b>	<b>+11.2</b>	<b>+1.1</b>	<b>+3.6</b>	<b>+2.9</b>	<b>+1.5</b>	<b>+10.9</b>
BRACS-F	Base	40.2	43.6	45.6	28.6	28.9	30.2	38.7	37.7	30.2	32.7	30.4	34.8
	$C = 7$	43.6	43.6	45.7	43.7	43.5	43.1	42.6	41.7	37.5	36.1	44.3	39.7
	(Bal. Acc.) $\Delta$	<b>+3.4</b>	<b>+0.0</b>	<b>+0.1</b>	<b>+15.1</b>	<b>+14.6</b>	<b>+12.9</b>	<b>+3.9</b>	<b>+4.0</b>	<b>+7.3</b>	<b>+3.4</b>	<b>+13.9</b>	<b>+4.9</b>

1604  
1605  
1606  
1607  
1608  
1609  
1610  
1611  
1612  
1613  
1614  
1615  
1616  
1617  
1618  
1619

1620

1621

1622 **Table A2: Molecular biomarker prediction** Change in performance between baseline MIL models  
 1623 and after the addition of MAMMOTH for 13 molecular biomarker prediction tasks. All tasks are  
 1624 binary prediction, with AUROC reported, with the exception of gbmlgg fine, which is a 7 class  
 1625 histomolecular classification task with balanced accuracy as the reported metric. Performance on  
 1626 GBMLGG is averaged between the internal TCGA cohort and external EBRAINS cohort. Standard  
 1627 deviation is reported according to 1,000 bootstrapped trials.

Task	Status	ABMIL	CLAM	TransMIL	Transf.	ILRA	MeanMIL	MaxMIL	DSMIL	Average
BCNB ER	Base	90.38(0.2)	91.22(0.7)	91.08(0.4)	90.35(0.5)	89.80(0.4)	90.77(0.3)	90.07(0.6)	88.84(0.8)	90.31
	+Ours	92.25(0.1)	92.72(0.2)	92.15(0.1)	92.02(0.1)	91.58(0.2)	92.19(0.1)	91.33(0.0)	90.93(0.1)	91.90
	Δ	+1.87	+1.50	+1.06	+1.67	+1.78	+1.42	+1.26	+2.09	+1.58
BCNB HER2	Base	73.05(0.4)	73.91(0.1)	68.90(0.7)	69.24(0.3)	71.38(0.6)	73.46(0.2)	74.33(0.5)	72.09(0.5)	72.04
	+Ours	74.70(0.4)	76.64(0.1)	71.40(0.1)	75.27(0.2)	74.34(0.3)	76.35(0.3)	75.56(0.0)	73.39(0.1)	74.71
	Δ	+1.65	+2.73	+2.50	+6.02	+2.97	+2.89	+1.23	+1.30	+2.66
BCNB PR	Base	82.48(0.4)	84.16(0.3)	82.30(0.8)	81.49(0.5)	81.90(0.6)	83.83(0.1)	84.34(0.5)	82.96(0.4)	82.93
	+Ours	85.84(0.5)	85.59(0.2)	85.37(0.5)	83.92(0.3)	83.88(0.5)	84.84(0.2)	85.12(0.4)	83.88(0.2)	84.80
	Δ	+3.36	+1.42	+3.07	+2.43	+1.98	+1.02	+0.78	+0.92	+1.87
BRCA ER	Base	86.93(0.3)	86.46(0.4)	87.38(0.3)	85.61(0.9)	85.00(0.4)	86.18(0.3)	86.84(0.3)	87.46(0.3)	86.48
	+Ours	87.94(0.3)	90.06(0.3)	88.59(0.1)	88.26(0.7)	87.01(0.3)	88.27(0.3)	87.65(0.0)	86.75(0.5)	88.07
	Δ	+1.01	+3.60	+1.20	+2.65	+2.01	+2.10	+0.81	-0.72	+1.58
BRCA HER2	Base	64.35(1.1)	64.38(0.9)	61.31(1.5)	65.25(1.2)	61.80(1.4)	62.59(1.0)	63.58(2.6)	60.90(0.6)	63.02
	+Ours	68.35(0.8)	61.84(0.1)	64.71(0.8)	64.84(0.1)	63.40(1.0)	67.59(0.6)	65.42(0.4)	65.94(0.7)	65.26
	Δ	+4.01	-2.54	+3.40	-0.41	+1.60	+5.00	+1.83	+5.04	+2.24
BRCA PIK3CA	Base	60.23(0.7)	59.15(0.7)	58.79(1.9)	57.43(0.9)	58.90(1.3)	60.23(1.2)	61.67(1.1)	61.30(0.7)	59.71
	+Ours	59.55(0.5)	58.38(0.2)	61.30(0.0)	60.27(0.5)	59.22(0.9)	58.99(0.8)	60.22(0.6)	60.96(0.2)	59.86
	Δ	-0.68	-0.77	+2.50	+2.84	+0.32	-1.24	-1.45	-0.35	+0.15
BRCA PR	Base	76.37(0.3)	77.73(0.7)	78.02(1.2)	77.12(0.3)	75.91(0.8)	76.36(0.5)	77.79(0.2)	78.00(0.8)	77.16
	+Ours	78.77(0.5)	78.80(0.6)	79.07(0.8)	79.44(0.1)	77.10(0.7)	79.54(0.6)	78.21(0.2)	79.05(0.2)	78.75
	Δ	+2.39	+1.07	+1.05	+2.32	+1.19	+3.18	+0.43	+1.06	+1.59
GBMLGG-C	Base	91.82(0.4)	94.38(0.5)	94.46(0.1)	93.41(1.0)	93.72(0.4)	94.34(0.2)	95.34(1.0)	94.88(0.4)	94.04
	+Ours	96.19(0.4)	94.53(0.1)	95.74(0.3)	95.68(0.2)	93.47(0.4)	95.34(0.7)	95.54(0.3)	94.80(0.4)	95.16
	Δ	+4.37	+0.15	+1.28	+2.27	-0.25	+1.00	+0.20	-0.08	+1.12
GBMLGG-F	Base	51.89(1.3)	49.78(1.3)	52.19(1.6)	50.58(1.9)	49.57(1.4)	49.68(0.9)	50.31(0.8)	49.53(2.4)	50.44
	+Ours	52.22(1.7)	51.03(0.3)	50.28(1.4)	53.12(0.4)	52.53(0.8)	51.63(1.2)	51.71(0.6)	50.68(0.7)	51.65
	Δ	+0.33	+1.25	-1.91	+2.55	+2.97	+1.95	+1.39	+1.15	+1.21
LUNG EGFR	Base	61.27(1.2)	65.85(0.6)	63.66(1.2)	60.20(1.8)	62.00(2.7)	64.42(0.7)	65.43(4.1)	63.93(1.6)	63.35
	+Ours	63.68(1.2)	65.98(0.8)	65.30(2.3)	67.55(1.2)	62.57(1.2)	66.17(1.1)	64.12(1.3)	65.51(1.3)	65.11
	Δ	+2.42	+0.13	+1.64	+7.35	+0.57	+1.74	-1.31	+1.59	+1.77
LUNG KRAS	Base	58.06(0.7)	60.81(0.7)	60.31(1.1)	58.22(1.5)	60.10(0.9)	60.88(1.2)	56.93(0.6)	59.21(0.4)	59.31
	+Ours	59.40(1.5)	59.42(0.8)	61.20(0.1)	59.45(0.3)	61.31(0.2)	61.22(0.5)	61.35(0.4)	58.10(0.7)	60.18
	Δ	+1.34	-1.39	+0.89	+1.23	+1.21	+0.35	+4.43	-1.10	+0.87
LUNG STK11	Base	76.41(1.1)	65.75(0.9)	68.95(2.2)	71.14(0.3)	69.10(1.8)	67.35(1.0)	70.06(2.6)	65.65(1.4)	69.30
	+Ours	74.36(1.5)	70.57(0.5)	66.44(1.1)	69.39(0.6)	68.10(0.7)	74.31(0.7)	73.48(0.3)	68.61(0.4)	70.66
	Δ	-2.05	+4.81	-2.51	-1.75	-1.00	+6.96	+3.41	+2.96	+1.36
LUNG TP53	Base	72.43(1.1)	73.04(0.3)	68.07(0.7)	70.19(1.1)	69.89(0.8)	72.29(0.3)	69.57(0.9)	71.31(0.8)	70.85
	+Ours	76.20(0.7)	71.60(0.1)	70.86(0.5)	73.46(0.9)	69.29(0.6)	75.00(0.5)	70.44(0.4)	71.88(0.7)	72.34
	Δ	+3.77	-1.44	+2.79	+3.28	-0.60	+2.71	+0.87	+0.56	+1.49

1652

1653

1654

1655

1656

1657 **Table A3: Ablations for model design.** Performance of ABMIL across individual tasks as a single  
 1658 MAMMOTH component is modified. Lin., linear; Sp., Sparse; MH, multihead; sink., sinkhorn.

Ablation	Model	EBRAINS		GBMLGG		BRACS		
		C	F	C	F	C	F	
Full model	Ours	90.0	72.9	96.2	52.2	72.4	46.1	
MoE method	MAMMOTH $\Rightarrow$ Lin. layer	86.1 (-4.3%)	67.2 (-7.8%)	91.8 (-4.6%)	51.9 (-0.6%)	67.1 (-7.3%)	42.8 (-7.2%)	
	Soft	88.7 (-1.4%)	70.3 (-3.6%)	93.7 (-2.6%)	43.8 (-16.1%)	64.9 (-10.4%)	46.0 (-0.2%)	
	Sp. MH	88.1 (-2.1%)	67.5 (-7.4%)	93.6 (-2.7%)	53.7 (+2.9%)	66.0 (-8.8%)	44.6 (-3.3%)	
	Sp. soft	87.2 (-3.1%)	69.6 (-4.5%)	93.9 (-2.4%)	56.0 (+7.3%)	65.9 (-9.0%)	28.6 (-38.0%)	
Num. heads	16	1	87.8 (-2.4%)	64.1 (-12.1%)	92.1 (-4.3%)	51.0 (-2.3%)	67.2 (-7.2%)	44.3 (-3.9%)
	$\mathbf{W}_{\text{low}}^{(k)} \Phi$	$\mathbf{W}_{\text{full}}^{(k)}$	89.2 (-0.9%)	72.7 (-0.3%)	95.2 (-1.0%)	51.7 (-1.0%)	69.2 (-4.4%)	36.2 (-21.5%)
$\Phi$	Shared	$\Rightarrow$ Per-expert	89.9 (-0.1%)	70.7 (-3.0%)	95.6 (-0.6%)	49.6 (-5.0%)	76.9 (+6.2%)	41.4 (-10.2%)
$\mathbf{W}$	Learned	$\Rightarrow$ Identity	86.8 (-3.6%)	73.8 (+1.2%)	93.2 (-3.1%)	51.2 (-1.9%)	63.0 (-13.1%)	41.1 (-10.9%)
Output	Slots	$\Rightarrow$ Patches	88.5 (-1.7%)	69.6 (-4.5%)	95.3 (-0.9%)	53.8 (+3.1%)	75.3 (+4.0%)	43.9 (-4.8%)

1672

1673

1674  
 1675  
 1676  
 1677  
 1678  
 1679  
 1680  
 1681  
 1682  
 1683  
 1684  
 1685  
 1686  
 1687  
 1688  
 1689  
 1690  
 1691

1692 Table A4: **Parameter count with varying number of experts** Number of parameters across dif-  
 1693 ferent expert counts in the task-specific layer as a single MAMMOTH component is modified, where  
 1694  $D = 1024$ ,  $D' = 512$ ,  $P = 256$ . Linear layer indicates the baseline parameter count without ex-  
 1695 perts. Entries with more parameters than the linear layer are **shown in bold**. Lin., Linear; Sp.,  
 1696 Sparse; MH., Multihead.

1697  
 1698  
 1699  
 1700  
 1701  
 1702  
 1703  
 1704  
 1705  
 1706  
 1707  
 1708  
 1709  
 1710

Ablation	Model		Parameter Count (Millions)			
			5 Experts	10 Experts	20 Experts	30 Experts
<b>Full model</b>	<b>Ours</b>		0.5	0.5	0.5	0.5
MoE method	MAMMOTH	$\Rightarrow$	Lin. layer	0.5	0.5	0.5
			Soft	<b>2.6</b>	<b>5.2</b>	<b>10.4</b>
			Sp. MH	<b>2.6</b>	<b>5.2</b>	<b>10.4</b>
			Softmax	<b>2.6</b>	<b>5.2</b>	<b>10.4</b>
			Sinkhorn	<b>2.6</b>	<b>5.2</b>	<b>10.4</b>
			PaMoE	<b>2.6</b>	<b>5.2</b>	<b>10.4</b>
	Num. heads	16	$\Rightarrow$	1	0.5	0.5
	Slot transform	$\mathbf{W}_{\text{low}}^{(k)} \Phi$	$\Rightarrow$	$\mathbf{W}_{\text{full}}^{(k)}$	<b>0.92</b>	<b>1.6</b>
	$\Phi$	Shared	$\Rightarrow$	Per-expert	0.5	0.5
	$\mathbf{W}$	Learned	$\Rightarrow$	Identity	0.5	0.5
Output		Slots	$\Rightarrow$	Patches	0.5	0.5

1711  
 1712  
 1713  
 1714  
 1715  
 1716  
 1717  
 1718  
 1719  
 1720  
 1721  
 1722  
 1723  
 1724  
 1725  
 1726  
 1727

1728

1729

1730

1731

1732

1733

1734

1735

1736

**Table A5: PaMoE comparison** Results of MIL methods with PaMoE and with MAMMOTH. The number of classes is specified below each task. The evaluation metrics for each task are specified in parentheses. All models use UNI features as patch embeddings (Chen et al., 2024a). Performance on NSCLC subtyping is averaged across the internal TCGA cohort and the external NLST and CPTAC cohorts. Trans., Transformer. Standard deviation is reported according to 1,000 bootstrapped trials.

Task	Status	ABMIL	CLAM	TransMIL	Trans.	ILRA	Mean	Max	DSMIL	Average
BRACS-C	PaMoE	70.52 (1.6)	54.3 (2.3)	73.01 (3.3)	63.40 (2.8)	63.27 (1.8)	64.72 (1.3)	56.79 (1.8)	61.59 (2.6)	63.45 (5.9)
C=3	+Ours	72.70 (1.4)	73.41 (2.1)	70.52 (3.1)	71.11 (3.6)	74.05 (2.5)	72.37 (1.4)	67.21 (1.6)	68.48 (2.8)	71.23 (2.2)
(Bal. acc.)	Δ	<b>+2.18</b>	<b>+19.11</b>	<b>-2.49</b>	<b>+7.71</b>	<b>+10.78</b>	<b>+7.65</b>	<b>+10.42</b>	<b>+6.89</b>	<b>+7.78</b>
BRACS-F	PaMoE	43.29 (2.0)	34.43 (1.4)	43.82 (0.8)	35.70 (1.9)	32.65 (2.1)	34.88 (2.4)	28.34 (0.5)	28.59 (0.5)	35.21 (5.5)
C=7	+Ours	46.12 (2.4)	46.82 (1.3)	38.32 (1.0)	38.95 (2.0)	42.50 (1.4)	43.55 (2.9)	35.52 (0.5)	39.72 (0.5)	41.44 (3.7)
(Bal. acc.)	Δ	<b>+2.83</b>	<b>+12.39</b>	<b>-5.5</b>	<b>+3.25</b>	<b>+9.85</b>	<b>+8.67</b>	<b>+7.18</b>	<b>+11.13</b>	<b>+6.22</b>
EBRAINS-C	PaMoE	89.95 (0.7)	87.82 (0.8)	86.71 (1.3)	86.94 (0.6)	83.41 (1.0)	86.93 (0.9)	83.61 (0.1)	85.45 (0.2)	86.35 (2.0)
C=12	+Ours	89.98 (0.7)	91.32 (0.7)	88.23 (1.2)	90.45 (0.9)	91.68 (0.6)	89.42 (1.1)	85.14 (0.1)	89.17 (0.3)	89.42 (1.9)
(Bal. acc.)	Δ	<b>+0.03</b>	<b>+3.5</b>	<b>+1.52</b>	<b>+3.51</b>	<b>+8.27</b>	<b>+2.49</b>	<b>+1.53</b>	<b>+3.72</b>	<b>+3.07</b>
EBRAINS-F	PaMoE	66.68 (1.1)	65.83 (0.4)	67.0 (0.2)	69.07 (1.7)	64.64 (1.0)	64.87 (0.2)	54.65 (0.3)	52.13 (0.3)	63.11 (5.8)
C=30	+Ours	72.40 (1.2)	72.51 (0.4)	74.22 (0.2)	69.73 (0.1)	70.23 (0.4)	72.89 (0.2)	68.22 (0.3)	69.40 (0.4)	71.2 (1.9)
(Bal. acc.)	Δ	<b>+5.72</b>	<b>+6.68</b>	<b>+7.22</b>	<b>+0.66</b>	<b>+5.59</b>	<b>+8.02</b>	<b>+13.57</b>	<b>+17.27</b>	<b>+8.09</b>
NSCLC	PaMoE	94.68 (0.1)	91.73 (0.1)	93.90 (0.1)	94.69 (0.1)	93.25 (0.1)	91.44 (0.1)	94.86 (0.1)	94.08 (0.1)	93.58 (1.3)
C=2	+Ours	94.68 (0.1)	93.72 (0.1)	93.99 (0.1)	94.04 (0.1)	93.87 (0.1)	93.91 (0.1)	94.44 (0.1)	94.43 (0.1)	94.14 (0.3)
(AUROC)	Δ	<b>+0.0</b>	<b>+1.99</b>	<b>+0.09</b>	<b>-0.65</b>	<b>+0.62</b>	<b>+2.47</b>	<b>-0.42</b>	<b>+0.35</b>	<b>+0.56</b>
BCNB ER	PaMoE	93.04 (0.1)	90.99 (0.1)	89.77 (0.1)	90.35 (0.5)	89.80 (0.4)	92.61 (0.1)	88.61 (0.1)	90.52 (0.1)	90.71 (1.4)
C=2	+Ours	92.25 (0.1)	92.72 (0.1)	92.15 (0.1)	92.02 (0.1)	91.58 (0.1)	92.19 (0.1)	91.33 (0.1)	90.93 (0.1)	91.9 (0.5)
(AUROC)	Δ	<b>-0.79</b>	<b>+1.73</b>	<b>+2.38</b>	<b>+1.67</b>	<b>+1.78</b>	<b>-0.42</b>	<b>+2.72</b>	<b>+0.41</b>	<b>+1.19</b>
BCNB HER2	PaMoE	72.28 (0.5)	73.76 (0.2)	69.96 (0.1)	69.24 (0.3)	71.38 (0.4)	70.98 (0.2)	67.23 (0.3)	70.21 (0.1)	70.63 (1.8)
C=2	+Ours	74.70 (0.4)	76.64 (0.3)	71.40 (0.1)	75.27 (0.2)	74.34 (0.2)	76.35 (0.3)	75.56 (0.2)	73.39 (0.1)	74.71 (1.6)
(AUROC)	Δ	<b>+2.42</b>	<b>+2.88</b>	<b>+1.44</b>	<b>+6.03</b>	<b>+2.96</b>	<b>+5.37</b>	<b>+8.33</b>	<b>+3.18</b>	<b>+4.08</b>
BCNB PR	PaMoE	83.81 (0.5)	83.69 (0.3)	82.0 (0.4)	81.49 (0.5)	81.90 (0.4)	83.62 (0.2)	82.89 (0.4)	83.13 (0.2)	82.82 (0.8)
C=2	+Ours	85.84 (0.5)	85.59 (0.4)	85.37 (0.5)	83.92 (0.4)	83.88 (0.4)	84.84 (0.2)	85.12 (0.4)	83.88 (0.2)	84.8 (0.8)
(AUROC)	Δ	<b>+2.03</b>	<b>+1.9</b>	<b>+3.37</b>	<b>+2.43</b>	<b>+1.98</b>	<b>+1.22</b>	<b>+2.23</b>	<b>+0.75</b>	<b>+1.99</b>
BRCA ER	PaMoE	87.71 (0.3)	87.15 (0.3)	87.52 (0.1)	85.61 (0.9)	85.00 (0.4)	84.24 (0.3)	81.16 (0.4)	85.53 (0.5)	85.49 (2.0)
C=2	+Ours	87.94 (0.3)	90.06 (0.3)	88.59 (0.1)	88.26 (0.7)	87.01 (0.4)	88.27 (0.3)	87.65 (0.3)	86.75 (0.5)	88.07 (1.0)
(AUROC)	Δ	<b>+0.23</b>	<b>+2.91</b>	<b>+1.07</b>	<b>+2.65</b>	<b>+2.01</b>	<b>+4.03</b>	<b>+6.49</b>	<b>+1.22</b>	<b>+2.58</b>
BRCA HER2	PaMoE	61.11 (0.9)	66.94 (0.5)	61.88 (0.9)	65.25 (1.2)	61.80 (1.5)	63.5 (0.7)	57.93 (0.4)	60.38 (0.6)	62.35 (2.7)
C=2	+Ours	68.35 (0.8)	61.84 (0.6)	64.71 (0.8)	64.84 (0.1)	63.40 (0.5)	67.59 (0.6)	65.42 (0.4)	65.94 (0.7)	65.26 (2.0)
(AUROC)	Δ	<b>+7.24</b>	<b>-5.1</b>	<b>+2.83</b>	<b>-0.41</b>	<b>+1.6</b>	<b>+4.09</b>	<b>+7.49</b>	<b>+5.56</b>	<b>+2.91</b>
BRCA PIK3CA	PaMoE	59.55 (0.5)	59.11 (0.5)	58.48 (0.5)	57.43 (0.9)	58.90 (1.0)	58.52 (1.0)	54.07 (0.6)	53.64 (0.2)	57.46 (2.2)
C=2	+Ours	59.55 (0.5)	58.38 (0.5)	61.30 (0.5)	60.27 (0.5)	59.22 (0.5)	58.99 (0.8)	60.22 (0.6)	60.96 (0.2)	59.86 (0.9)
(AUROC)	Δ	<b>+0.0</b>	<b>-0.73</b>	<b>+2.82</b>	<b>+2.84</b>	<b>+0.32</b>	<b>+0.47</b>	<b>+6.15</b>	<b>+7.32</b>	<b>+2.4</b>
BRCA PR	PaMoE	76.53 (0.4)	76.5 (0.4)	75.53 (0.7)	77.12 (0.3)	75.91 (0.5)	75.05 (0.5)	72.87 (0.2)	76.26 (0.2)	75.72 (1.2)
C=2	+Ours	78.77 (0.5)	78.80 (0.4)	79.07 (0.8)	79.44 (0.1)	77.10 (0.3)	79.54 (0.6)	78.21 (0.2)	79.05 (0.2)	78.75 (0.7)
(AUROC)	Δ	<b>+2.24</b>	<b>+2.3</b>	<b>+3.54</b>	<b>+2.32</b>	<b>+1.19</b>	<b>+4.49</b>	<b>+5.34</b>	<b>+2.79</b>	<b>+3.03</b>
GBMLGG-C	PaMoE	54.15 (1.8)	52.5 (1.0)	53.94 (1.2)	50.58 (1.9)	49.57 (1.2)	53.02 (1.4)	51.19 (0.6)	51.31 (0.7)	52.03 (1.5)
C=5	+Ours	52.22 (1.7)	51.03 (1.1)	50.28 (1.4)	53.12 (0.4)	52.53 (1.0)	51.63 (1.2)	51.71 (0.6)	50.68 (0.7)	51.65 (0.9)
(AUROC)	Δ	<b>-1.93</b>	<b>-1.47</b>	<b>-3.66</b>	<b>+2.54</b>	<b>+2.96</b>	<b>-1.39</b>	<b>+0.52</b>	<b>-0.63</b>	<b>-0.38</b>
LUNG EGFR	PaMoE	67.25 (1.2)	61.41 (1.2)	62.68 (2.4)	60.20 (1.8)	62.00 (1.5)	62.45 (0.9)	65.59 (1.3)	59.78 (1.5)	62.67 (2.4)
C=2	+Ours	63.68 (1.2)	65.98 (1.4)	65.30 (2.3)	67.55 (1.2)	62.57 (1.7)	66.17 (1.1)	64.12 (1.3)	65.51 (1.3)	65.11 (1.5)
(AUROC)	Δ	<b>-3.57</b>	<b>+4.57</b>	<b>+2.62</b>	<b>+7.35</b>	<b>+0.57</b>	<b>+3.72</b>	<b>-1.47</b>	<b>+5.73</b>	<b>+2.44</b>
LUNG KRAS	PaMoE	59.52 (1.5)	59.18 (0.8)	60.41 (0.1)	58.22 (1.5)	60.10 (0.9)	62.58 (0.6)	54.73 (0.8)	51.82 (0.8)	58.32 (3.2)
C=2	+Ours	59.40 (1.5)	59.42 (0.8)	61.20 (0.1)	59.45 (0.6)	61.31 (0.8)	61.22 (0.5)	61.35 (0.7)	58.10 (0.7)	60.18 (1.2)
(AUROC)	Δ	<b>-0.12</b>	<b>+0.24</b>	<b>+0.79</b>	<b>+1.23</b>	<b>+1.21</b>	<b>-1.36</b>	<b>+6.62</b>	<b>+6.28</b>	<b>+1.86</b>
LUNG STK11	PaMoE	75.41 (1.4)	70.47 (1.0)	69.28 (1.1)	71.14 (0.3)	69.10 (1.6)	67.83 (0.8)	68.02 (0.3)	65.74 (0.4)	69.62 (2.7)
C=2	+Ours	74.36 (1.5)	70.57 (0.9)	66.44 (1.1)	69.39 (0.6)	68.10 (0.8)	74.31 (0.7)	73.48 (0.3)	68.61 (0.4)	70.66 (2.9)
(AUROC)	Δ	<b>-1.05</b>	<b>+0.1</b>	<b>-2.84</b>	<b>-1.75</b>	<b>-1.0</b>	<b>+6.48</b>	<b>+5.46</b>	<b>+2.87</b>	<b>+1.03</b>
LUNG TP53	PaMoE	70.22 (0.8)	68.22 (0.9)	69.47 (0.5)	70.19 (1.1)	69.89 (0.7)	72.46 (0.5)	70.09 (0.5)	70.7 (0.7)	70.16 (1.1)
C=2	+Ours	76.20 (0.7)	71.60 (0.8)	70.86 (0.5)	73.46 (0.9)	69.29 (0.7)	75.00 (0.5)	70.44 (0.6)	71.88 (0.7)	72.34 (2.2)
(AUROC)	Δ	<b>+5.98</b>	<b>+3.38</b>	<b>+1.39</b>	<b>+3.27</b>	<b>-0.6</b>	<b>+2.54</b>	<b>+0.35</b>	<b>+1.18</b>	<b>+2.19</b>

1774

1775

1776

1777

1778

1779

1780

1781

1782  
1783 **Table A6: Pre-Aggregation comparisons with tissue subtyping.** Performance comparison across  
1784 **MIL** methods for tissue subtyping with different plug-and-play methods. Best task-level perfor-  
1785 mance is shown in **bold**, second best underlined. Ours (MAMMOTH) consistently yields the highest  
1786 performance across all tasks and MIL methods.

	Task	Base	+Ours	+PAMoE	+RRT	+MIL Dropout	+Querent
1787 1788 1789 1790 1791 1792	BRACS C	67.10 (1.20)	<b>72.70</b> (1.40)	70.52 (1.24)	66.39 (1.29)	<u>71.60</u> (1.37)	66.49 (1.22)
	BRACS F	42.84 (2.50)	46.12 (2.40)	43.29 (2.76)	44.13 (2.65)	<u>47.09</u> (2.42)	<b>47.71</b> (2.64)
	EBRAINS C	86.10 (1.10)	<b>89.98</b> (0.70)	<u>89.95</u> (0.80)	88.70 (0.96)	<u>88.51</u> (0.90)	86.76 (0.94)
	EBRAINS F	67.20 (1.00)	<b>72.40</b> (1.20)	<u>66.68</u> (1.31)	<u>69.20</u> (1.26)	<u>68.25</u> (1.03)	67.94 (1.22)
	NSCLC	94.68 (0.10)	94.68 (0.10)	94.68 (0.10)	<u>95.42</u> (0.10)	94.33 (0.10)	<b>95.67</b> (0.10)
	PANDA	93.12 (0.20)	<b>94.28</b> (0.20)	93.36 (0.22)	93.29 (0.22)	90.35 (0.21)	90.46 (0.21)
1793 1794 1795 1796 1797 1798	<b>Average</b>	75.17	<b>78.36</b>	76.41	76.19	<u>77.69</u>	75.84
	BRACS C	56.16 (2.32)	<b>73.41</b> (2.06)	54.30 (2.03)	60.33 (2.26)	58.28 (2.12)	<u>65.04</u> (2.25)
	BRACS F	32.26 (2.91)	<b>46.82</b> (1.26)	<u>34.43</u> (1.41)	34.05 (1.96)	33.05 (2.33)	<u>34.07</u> (1.67)
	EBRAINS C	87.85 (0.91)	<b>91.32</b> (0.73)	87.82 (0.68)	<u>90.54</u> (0.83)	88.88 (0.90)	<b>86.45</b> (0.81)
	EBRAINS F	69.77 (1.37)	<b>72.51</b> (0.43)	65.83 (0.39)	<u>71.52</u> (1.02)	69.83 (0.69)	56.95 (0.97)
	NSCLC	91.73 (0.12)	<u>93.72</u> (0.10)	91.73 (0.12)	91.50 (0.12)	90.52 (0.10)	<b>96.01</b> (0.10)
1799 1800 1801 1802 1803 1804	PANDA	92.60 (0.40)	<b>93.26</b> (0.27)	93.11 (0.29)	92.59 (0.38)	88.26 (0.35)	92.14 (0.35)
	<b>Average</b>	71.73	<b>78.51</b>	71.20	73.42	72.47	71.77
	BRACS C	62.64 (2.40)	<u>68.48</u> (2.80)	61.59 (2.86)	57.65 (2.48)	<u>56.65</u> (2.78)	<b>68.84</b> (2.49)
	BRACS F	36.48 (4.20)	<u>39.72</u> (0.50)	28.59 (0.48)	<b>48.64</b> (2.59)	<u>47.64</u> (3.90)	34.75 (1.13)
	EBRAINS C	86.37 (2.00)	<b>89.17</b> (0.30)	85.45 (0.32)	84.77 (0.70)	<u>83.77</u> (1.31)	<u>87.01</u> (1.76)
	EBRAINS F	63.87 (1.70)	<u>69.40</u> (0.40)	52.13 (0.44)	68.61 (0.76)	62.91 (1.53)	<u>72.43</u> (0.77)
1805 1806 1807 1808 1809 1810	NSCLC	94.08 (0.11)	<u>94.43</u> (0.11)	94.08 (0.11)	93.53 (0.11)	92.53 (0.11)	<b>94.56</b> (0.11)
	PANDA	92.78 (0.20)	<u>92.96</u> (0.10)	91.26 (0.11)	<b>93.56</b> (0.15)	92.56 (0.16)	92.20 (0.11)
	<b>Average</b>	72.70	<b>75.69</b>	68.85	74.46	73.68	74.97
	BRACS C	63.27 (1.78)	<b>74.05</b> (2.54)	63.27 (1.78)	62.14 (2.32)	66.57 (2.31)	<u>70.74</u> (2.23)
	BRACS F	32.65 (2.10)	<u>42.50</u> (1.38)	32.65 (2.10)	36.21 (1.80)	32.85 (1.51)	<b>46.06</b> (1.48)
	EBRAINS C	83.41 (0.98)	<b>91.68</b> (0.64)	83.41 (0.98)	89.15 (0.67)	85.27 (0.81)	90.40 (0.74)
1811 1812 1813 1814 1815 1816	EBRAINS F	64.64 (0.98)	<u>70.23</u> (0.37)	64.64 (0.98)	69.13 (0.65)	61.65 (0.67)	<u>71.14</u> (0.73)
	NSCLC	93.25 (0.09)	<u>93.87</u> (0.12)	93.25 (0.09)	<b>94.36</b> (0.11)	93.42 (0.10)	93.28 (0.10)
	PANDA	91.89 (0.30)	<b>94.07</b> (0.25)	91.89 (0.30)	<u>93.47</u> (0.29)	91.65 (0.29)	92.98 (0.29)
	<b>Average</b>	71.52	<b>77.73</b>	71.52	74.07	72.90	77.43
	BRACS C	65.13 (1.70)	<b>72.37</b> (1.40)	64.72 (1.14)	57.43 (1.18)	56.43 (1.49)	<u>67.93</u> (1.37)
	BRACS F	33.68 (1.40)	<b>43.55</b> (2.90)	<u>34.88</u> (2.40)	32.31 (2.51)	31.31 (2.61)	<u>29.51</u> (2.55)
1817 1818 1819 1820 1821 1822	EBRAINS C	86.70 (0.70)	<b>89.42</b> (1.10)	<u>86.93</u> (1.06)	86.90 (0.71)	<u>85.90</u> (1.01)	82.13 (0.77)
	EBRAINS F	70.30 (1.40)	<b>72.89</b> (0.20)	64.87 (0.17)	<u>72.28</u> (0.66)	71.28 (0.84)	60.03 (1.19)
	NSCLC	91.44 (0.11)	<u>93.91</u> (0.11)	91.44 (0.11)	<u>92.27</u> (0.11)	91.27 (0.11)	<b>94.96</b> (0.11)
	PANDA	92.67 (0.30)	<b>93.52</b> (0.20)	90.64 (0.21)	92.46 (0.21)	91.46 (0.23)	92.46 (0.25)
	<b>Average</b>	73.32	<b>77.61</b>	72.25	72.27	72.27	71.17
	BRACS C	66.80 (2.70)	<u>70.52</u> (3.10)	<b>73.01</b> (2.83)	57.43 (3.01)	62.90 (3.04)	60.28 (3.03)
1823 1824 1825 1826 1827 1828	BRACS F	32.10 (2.70)	<u>38.32</u> (1.00)	43.82 (1.03)	<b>44.21</b> (2.03)	43.42 (1.63)	40.13 (2.68)
	EBRAINS C	87.86 (1.10)	<u>88.23</u> (1.20)	<u>86.71</u> (1.39)	<b>89.75</b> (1.34)	85.35 (1.29)	<u>88.96</u> (1.19)
	EBRAINS F	65.20 (0.50)	<b>74.22</b> (0.20)	67.00 (0.21)	67.67 (0.36)	<u>66.83</u> (0.35)	<u>68.48</u> (0.36)
	NSCLC	93.90 (0.08)	<u>93.99</u> (0.10)	93.90 (0.08)	<b>95.22</b> (0.09)	93.97 (0.09)	<u>94.78</u> (0.09)
	PANDA	90.75 (0.70)	<b>93.68</b> (0.30)	89.74 (0.34)	90.78 (0.34)	91.29 (0.42)	<u>92.23</u> (0.31)
	<b>Average</b>	72.77	<b>76.49</b>	75.70	74.18	74.96	74.14
1829 1830 1831 1832 1833 1834	BRACS C	63.40 (2.80)	<b>71.11</b> (3.60)	63.40 (2.80)	<u>68.70</u> (3.42)	58.78 (3.22)	60.51 (3.12)
	BRACS F	35.70 (1.90)	38.95 (2.00)	35.70 (1.90)	<b>44.21</b> (1.92)	40.45 (1.98)	<u>40.56</u> (1.92)
	EBRAINS C	86.94 (0.60)	<b>90.45</b> (0.90)	<u>86.94</u> (0.60)	85.63 (0.89)	84.03 (0.83)	83.47 (0.81)
	EBRAINS F	69.07 (1.70)	<u>69.73</u> (0.10)	69.07 (1.70)	66.74 (0.98)	67.10 (0.21)	<b>70.16</b> (0.79)
	NSCLC	94.69 (0.08)	94.04 (0.10)	<u>94.69</u> (0.08)	93.72 (0.10)	93.41 (0.09)	<b>95.35</b> (0.09)
	PANDA	91.39 (0.50)	91.90 (0.80)	91.39 (0.50)	89.97 (0.63)	88.72 (0.51)	<b>92.46</b> (0.60)
1835 1836 1837 1838 1839 1840	<b>Average</b>	73.53	<b>76.03</b>	73.53	<u>74.83</u>	73.08	73.75
	BRACS C	64.54 (2.40)	<b>67.21</b> (1.60)	56.79 (1.28)	57.88 (1.83)	63.27 (2.02)	60.91 (1.97)
	BRACS F	33.90 (2.40)	<u>35.52</u> (0.50)	28.34 (0.48)	28.40 (2.13)	33.61 (0.69)	<b>47.63</b> (0.60)
	EBRAINS C	84.55 (1.20)	<u>85.14</u> (0.10)	83.61 (0.09)	<b>87.60</b> (0.49)	81.76 (0.94)	77.98 (1.06)
	EBRAINS F	64.94 (1.00)	<b>68.22</b> (0.30)	54.65 (0.35)	<u>68.10</u> (0.78)	63.26 (0.72)	56.11 (0.95)
	NSCLC	94.86 (0.10)	94.44 (0.10)	94.86 (0.10)	<b>95.59</b> (0.10)	94.89 (0.10)	94.33 (0.10)
1841 1842	PANDA	88.79 (0.30)	<b>92.34</b> (0.20)	86.81 (0.20)	88.82 (0.24)	87.81 (0.29)	<b>90.75</b> (0.26)
	<b>Average</b>	71.93	<b>73.81</b>	67.51	71.06	71.77	71.29

1836

1837 Table A7: **MIL performance with pre-aggregation methods.** Performance comparison across  
1838 Transformer, TransMIL, ILRA, and CLAM MIL methods for molecular subtyping. Best task-level  
1839 performance is shown in **bold**, second best underlined.  
1840

	Task	Base	+Ours	+PAMoE	+RRT	+MIL Dropout	+Querent
Transformer	BCNB ER	90.35 (0.50)	<b>92.02</b> (0.09)	90.35 (0.50)	88.25 (0.32)	87.67 (0.47)	90.87 (0.24)
	BCNB HER2	69.24 (0.30)	<u>75.27</u> (0.20)	69.24 (0.30)	<u>68.58</u> (0.30)	<u>66.07</u> (0.24)	<u>74.36</u> (0.29)
	BCNB PR	81.49 (0.50)	<u>83.92</u> (0.33)	81.49 (0.50)	<u>78.78</u> (0.42)	<u>79.54</u> (0.35)	<u>83.65</u> (0.41)
	BRCA ER	85.61 (0.90)	<b>88.26</b> (0.70)	85.61 (0.90)	84.35 (0.88)	<u>87.07</u> (0.88)	86.34 (0.88)
	BRCA HER2	<b>65.25</b> (1.20)	<u>64.84</u> (0.10)	<b>65.25</b> (1.20)	57.00 (0.69)	<u>58.21</u> (0.73)	63.43 (0.14)
	BRCA PIK3CA	57.43 (0.90)	<b>60.27</b> (0.50)	57.43 (0.90)	<u>53.60</u> (0.87)	<u>52.80</u> (0.58)	<u>57.58</u> (0.55)
	BRCA PR	<u>77.12</u> (0.30)	<b>79.44</b> (0.10)	<u>77.12</u> (0.30)	75.76 (0.21)	74.49 (0.23)	75.50 (0.26)
	GBMLGG C	93.41 (1.00)	<b>95.68</b> (0.51)	93.41 (1.00)	<u>93.50</u> (0.69)	93.21 (0.99)	92.36 (0.75)
	GBMLGG F	50.58 (1.90)	<b>53.12</b> (0.40)	50.58 (1.90)	48.04 (1.45)	50.07 (0.59)	<u>51.17</u> (1.80)
	LUNG EGFR	60.20 (1.80)	<u>67.55</u> (1.20)	60.20 (1.80)	59.06 (1.39)	58.00 (1.48)	<b>68.23</b> (1.56)
	LUNG KRAS	58.22 (1.50)	<b>59.45</b> (0.78)	58.22 (1.50)	53.69 (1.26)	53.39 (1.10)	57.02 (1.27)
TransMIL	LUNG STK11	<b>71.14</b> (0.30)	69.39 (0.60)	<b>71.14</b> (0.30)	64.45 (0.47)	66.04 (0.53)	<b>69.57</b> (0.36)
	LUNG TP53	70.19 (1.10)	<b>73.46</b> (0.90)	70.19 (1.10)	68.98 (1.00)	66.36 (1.03)	69.04 (0.92)
	<b>Average</b>	71.56	<b>74.05</b>	71.56	68.77	69.69	<b>72.24</b>
	BCNB ER	91.08 (0.40)	<b>92.15</b> (0.10)	89.77 (0.11)	89.45 (0.33)	88.79 (0.25)	89.85 (0.33)
	BCNB HER2	68.90 (0.70)	71.40 (0.10)	<u>69.96</u> (0.10)	<u>72.43</u> (0.20)	71.86 (0.13)	<b>75.51</b> (0.62)
	BCNB PR	82.30 (0.80)	<b>85.37</b> (0.50)	82.00 (0.56)	82.04 (0.78)	80.75 (0.52)	<u>83.69</u> (0.53)
	BRCA ER	87.38 (0.30)	<b>88.59</b> (0.10)	<u>87.52</u> (0.09)	87.47 (0.28)	86.51 (0.13)	86.70 (0.25)
	BRCA HER2	61.31 (1.50)	<b>64.71</b> (0.80)	<u>61.88</u> (0.82)	<u>62.98</u> (1.45)	61.74 (0.98)	61.47 (1.13)
	BRCA PIK3CA	58.79 (1.90)	<b>61.30</b> (0.43)	58.48 (0.50)	<u>56.90</u> (1.53)	55.52 (1.59)	<u>59.99</u> (1.19)
	BRCA PR	78.02 (1.20)	<b>79.07</b> (0.80)	75.53 (0.76)	74.39 (0.81)	72.75 (0.95)	<u>78.17</u> (1.07)
	GBMLGG C	94.46 (0.10)	<b>95.74</b> (0.30)	<u>94.65</u> (0.35)	94.01 (0.21)	92.62 (0.35)	<u>91.56</u> (0.22)
	GBMLGG F	52.19 (1.60)	50.28 (1.40)	<b>53.94</b> (1.65)	51.03 (1.58)	<u>53.62</u> (1.54)	52.01 (1.43)
	LUNG EGFR	<u>63.66</u> (1.20)	<b>65.30</b> (2.30)	62.68 (2.35)	62.03 (1.40)	<u>61.74</u> (1.31)	61.80 (1.78)
	LUNG KRAS	<u>60.31</u> (1.10)	<b>61.20</b> (0.10)	<u>60.41</u> (0.09)	55.39 (0.66)	57.25 (0.87)	58.90 (0.10)
ILRA	LUNG STK11	68.95 (2.20)	66.44 (1.10)	<u>69.28</u> (1.31)	60.10 (1.84)	<b>69.48</b> (1.38)	67.63 (1.34)
	LUNG TP53	68.07 (0.70)	<u>70.86</u> (0.50)	69.47 (0.54)	67.64 (0.62)	68.31 (0.67)	<b>71.77</b> (0.52)
	<b>Average</b>	71.96	<b>73.26</b>	71.97	70.45	71.84	<b>72.23</b>
	BCNB ER	89.80 (0.46)	<b>91.58</b> (0.09)	89.80 (0.46)	<u>91.25</u> (0.25)	91.04 (0.13)	90.11 (0.29)
	BCNB HER2	71.38 (0.47)	<u>74.34</u> (0.26)	71.38 (0.47)	<u>73.10</u> (0.29)	73.73 (0.42)	<b>75.16</b> (0.27)
	BCNB PR	81.90 (0.51)	<u>83.88</u> (0.29)	81.90 (0.51)	<b>84.28</b> (0.50)	81.56 (0.34)	82.36 (0.50)
	BRCA ER	85.00 (0.47)	<u>87.01</u> (0.40)	85.00 (0.47)	86.50 (0.44)	85.80 (0.43)	<b>87.24</b> (0.47)
	BRCA HER2	61.80 (1.21)	<u>63.40</u> (0.51)	61.80 (1.21)	<b>63.86</b> (0.80)	62.34 (0.59)	63.40 (0.60)
	BRCA PIK3CA	58.90 (1.04)	<u>59.22</u> (0.52)	58.90 (1.04)	57.66 (0.76)	<b>59.31</b> (0.69)	57.88 (0.99)
	BRCA PR	75.91 (0.58)	<b>77.10</b> (0.33)	75.91 (0.58)	<u>77.01</u> (0.44)	70.99 (0.57)	74.86 (0.48)
	GBMLGG C	93.72 (0.52)	93.47 (0.38)	<u>93.72</u> (0.52)	93.10 (0.39)	91.85 (0.43)	<b>94.28</b> (0.43)
	GBMLGG F	49.57 (1.25)	<b>52.53</b> (1.18)	49.57 (1.25)	49.86 (1.19)	50.71 (1.25)	<u>51.95</u> (1.22)
	LUNG EGFR	62.00 (1.77)	<u>62.57</u> (1.61)	62.00 (1.77)	60.34 (1.67)	58.43 (1.64)	<b>64.11</b> (1.69)
	LUNG KRAS	60.10 (0.96)	<b>61.31</b> (0.71)	<u>60.10</u> (0.96)	54.69 (0.72)	55.95 (0.89)	57.01 (0.93)
CLAM	LUNG STK11	<b>69.10</b> (1.16)	68.10 (0.87)	<b>69.10</b> (1.16)	64.85 (0.94)	<u>68.56</u> (0.97)	66.32 (1.11)
	LUNG TP53	69.89 (0.94)	69.29 (0.66)	<u>69.89</u> (0.94)	68.05 (0.92)	68.11 (0.77)	<b>70.72</b> (0.80)
	<b>Average</b>	71.47	<b>72.60</b>	71.47	71.12	71.64	<b>71.95</b>
	BCNB ER	<u>91.22</u> (0.42)	<b>92.72</b> (0.09)	90.99 (0.09)	<u>90.59</u> (0.13)	89.56 (0.13)	88.17 (0.22)
	BCNB HER2	73.91 (0.38)	<b>76.64</b> (0.21)	<u>73.76</u> (0.24)	73.82 (0.23)	<u>72.97</u> (0.28)	<u>75.34</u> (0.34)
	BCNB PR	84.16 (0.48)	<b>85.59</b> (0.32)	83.69 (0.28)	<u>84.80</u> (0.47)	83.76 (0.30)	<u>83.15</u> (0.38)
	BRCA ER	86.46 (0.35)	<b>90.06</b> (0.35)	87.15 (0.35)	<u>86.47</u> (0.35)	85.32 (0.35)	<u>87.18</u> (0.35)
	BRCA HER2	<u>64.38</u> (1.31)	61.84 (0.58)	<b>66.94</b> (0.60)	63.88 (0.61)	63.15 (0.58)	<u>63.76</u> (1.14)
	BRCA PIK3CA	<u>59.15</u> (1.26)	58.38 (0.62)	59.11 (0.50)	<u>59.18</u> (0.62)	57.96 (0.68)	<b>59.87</b> (0.95)
	BRCA PR	77.73 (0.46)	<b>78.80</b> (0.39)	76.50 (0.46)	<u>76.32</u> (0.44)	75.27 (0.39)	<b>78.21</b> (0.45)
	GBMLGG C	94.38 (0.62)	<u>94.53</u> (0.53)	93.83 (0.55)	<b>95.17</b> (0.58)	94.17 (0.59)	92.68 (0.59)
	GBMLGG F	49.78 (1.57)	<u>51.03</u> (0.98)	<b>52.50</b> (1.15)	49.37 (1.46)	46.42 (1.20)	49.66 (1.16)
	LUNG EGFR	<u>65.85</u> (1.60)	<b>65.98</b> (1.63)	61.41 (1.34)	<u>63.44</u> (1.42)	64.33 (1.38)	65.10 (1.48)
	LUNG KRAS	<b>60.81</b> (0.97)	<u>59.42</u> (0.77)	59.18 (0.66)	<u>55.26</u> (0.75)	56.33 (0.68)	57.45 (0.73)
	LUNG STK11	65.75 (1.33)	<u>70.57</u> (0.88)	70.47 (0.99)	<u>69.19</u> (1.31)	69.85 (1.27)	<b>76.65</b> (1.27)
	LUNG TP53	<b>73.04</b> (0.67)	<u>71.60</u> (0.55)	68.22 (0.46)	<u>69.56</u> (0.58)	70.44 (0.52)	70.90 (0.61)
1889	<b>Average</b>	72.82	<b>73.63</b>	72.60	72.08	72.50	<b>72.93</b>

1890

1891

1892 Table A8: **Pre-Aggregation comparisons with molecular subtyping.** Performance comparison  
1893 across MIL methods (ABMIL, maxMIL, meanMIL, DSMIL) for molecular subtyping. Best task-  
1894 level performance is shown in **bold**, second best underlined.

1895

1896

1897

1898

1899

1900

1901

1902

1903

1904

1905

1906

1907

1908

1909

1910

1911

1912

1913

1914

1915

1916

1917

1918

1919

1920

1921

1922

1923

1924

1925

1926

1927

1928

1929

1930

1931

1932

1933

1934

1935

1936

1937

1938

1939

1940

1941

1942

1943

	Task	Base	+Ours	+PAMoE	+RRT	+MIL Dropout	+Querent
ABMIL	BCNB ER	90.38 (0.20)	<u>92.25</u> (0.10)	<b>93.04</b> (0.08)	91.71 (0.08)	91.42 (0.18)	90.07 (0.09)
	BCNB HER2	73.05 (0.40)	<u>74.70</u> (0.40)	72.28 (0.42)	<u>74.66</u> (0.42)	73.91 (0.41)	<b>76.14</b> (0.40)
	BCNB PR	82.48 (0.40)	<b>85.84</b> (0.50)	83.81 (0.45)	84.26 (0.41)	84.08 (0.46)	<u>84.29</u> (0.49)
	BRCA ER	86.93 (0.30)	<b>87.94</b> (0.30)	87.71 (0.25)	<u>87.78</u> (0.28)	87.06 (0.26)	<u>86.80</u> (0.29)
	BRCA HER2	64.35 (1.10)	<b>68.35</b> (0.80)	61.11 (0.69)	<u>67.00</u> (0.80)	66.01 (0.70)	64.33 (0.90)
	BRCA PIK3CA	60.23 (0.70)	59.55 (0.50)	<u>59.55</u> (0.58)	<u>59.52</u> (0.57)	59.63 (0.67)	<b>60.86</b> (0.68)
	BRCA PR	76.37 (0.30)	<b>78.77</b> (0.50)	76.53 (0.44)	77.26 (0.35)	<u>78.31</u> (0.31)	77.66 (0.47)
	GBMLGG C	91.82 (0.40)	<b>96.19</b> (0.40)	95.79 (0.39)	<u>95.81</u> (0.39)	<u>95.09</u> (0.40)	95.12 (0.45)
	GBMLGG F	51.89 (1.30)	<u>52.22</u> (1.70)	<b>54.15</b> (2.01)	47.98 (1.76)	43.47 (1.97)	51.94 (1.68)
	LUNG EGFR	61.27 (1.20)	<u>63.68</u> (1.20)	<u>67.25</u> (1.18)	<b>67.27</b> (1.19)	66.45 (1.18)	63.90 (1.19)
MaxMIL	LUNG KRAS	58.06 (0.70)	<u>59.40</u> (1.50)	<b>59.52</b> (1.54)	57.89 (1.44)	58.88 (1.46)	59.28 (0.81)
	LUNG STK11	<b>76.41</b> (1.10)	<u>74.36</u> (1.50)	75.41 (1.57)	<u>75.50</u> (1.17)	<u>75.54</u> (1.49)	<u>76.06</u> (1.38)
	LUNG TP53	72.43 (1.10)	<b>76.20</b> (0.70)	70.22 (0.69)	71.47 (0.73)	70.87 (0.73)	<u>70.49</u> (0.90)
	<b>Average</b>	72.74	<b>74.57</b>	73.57	73.70	73.13	<u>73.61</u>
	BCNB ER	90.07 (0.60)	<b>91.33</b> (0.12)	88.61 (0.13)	<u>90.74</u> (0.29)	90.38 (0.41)	88.61 (0.38)
	BCNB HER2	74.33 (0.50)	<u>75.56</u> (0.23)	67.23 (0.20)	<u>75.33</u> (0.34)	<b>75.97</b> (0.28)	75.00 (0.36)
	BCNB PR	<u>84.34</u> (0.50)	<b>85.12</b> (0.40)	82.89 (0.34)	83.97 (0.44)	82.65 (0.46)	83.69 (0.45)
	BRCA ER	86.84 (0.30)	<b>87.65</b> (0.36)	81.16 (0.41)	84.57 (0.40)	84.18 (0.37)	86.08 (0.38)
	BRCA HER2	63.58 (2.60)	<u>65.42</u> (0.40)	57.93 (0.44)	<u>63.57</u> (1.29)	59.20 (0.99)	<b>65.91</b> (1.66)
	BRCA PIK3CA	<b>61.67</b> (1.10)	<u>60.22</u> (0.60)	54.07 (0.57)	<u>58.57</u> (0.94)	56.76 (0.61)	58.40 (0.64)
MeanMIL	BRCA PR	77.79 (0.20)	<u>78.21</u> (0.20)	72.87 (0.16)	<b>79.34</b> (0.17)	78.06 (0.17)	77.36 (0.18)
	GBMLGG C	<u>95.34</u> (1.00)	<b>95.54</b> (0.50)	87.12 (0.53)	93.49 (0.55)	92.92 (0.67)	91.60 (0.90)
	GBMLGG F	50.31 (0.80)	<u>51.71</u> (0.60)	51.19 (0.57)	<b>55.32</b> (0.62)	49.49 (0.69)	48.43 (0.63)
	LUNG EGFR	65.43 (4.10)	<u>64.12</u> (1.30)	<u>65.59</u> (1.30)	<b>66.44</b> (1.76)	60.62 (2.89)	63.74 (3.29)
	LUNG KRAS	56.93 (0.60)	<b>61.35</b> (0.71)	<u>54.73</u> (0.74)	56.23 (0.70)	56.79 (0.74)	<u>60.51</u> (0.72)
	LUNG STK11	70.06 (2.60)	<b>73.48</b> (0.30)	68.02 (0.30)	69.47 (0.73)	73.13 (1.79)	<u>68.02</u> (1.78)
	LUNG TP53	69.57 (0.90)	70.44 (0.55)	70.09 (0.63)	<u>70.79</u> (0.61)	<b>75.62</b> (0.79)	67.63 (0.89)
	<b>Average</b>	72.79	<b>73.86</b>	69.35	72.91	72.98	71.92
	BCNB ER	90.77 (0.53)	<u>92.19</u> (0.10)	<b>92.61</b> (0.09)	90.63 (0.20)	89.63 (0.26)	89.53 (0.18)
	BCNB HER2	73.46 (0.20)	<u>76.35</u> (0.30)	70.98 (0.27)	<u>74.50</u> (0.25)	73.50 (0.23)	<b>76.59</b> (0.24)
Mean	BCNB PR	83.83 (0.10)	<b>84.84</b> (0.20)	83.62 (0.20)	<u>84.17</u> (0.10)	83.17 (0.12)	84.00 (0.18)
	BRCA ER	86.18 (0.30)	<u>88.27</u> (0.30)	84.24 (0.35)	<u>84.78</u> (0.32)	83.78 (0.33)	85.07 (0.30)
	BRCA HER2	62.59 (1.00)	<b>67.59</b> (0.60)	63.50 (0.62)	63.97 (0.85)	62.97 (0.73)	<u>66.03</u> (0.84)
	BRCA PIK3CA	60.23 (1.20)	58.99 (0.80)	58.52 (0.65)	<u>60.53</u> (0.98)	59.53 (0.76)	<b>62.04</b> (1.08)
	BRCA PR	76.36 (0.50)	<b>79.54</b> (0.60)	75.05 (0.51)	<u>76.75</u> (0.51)	75.75 (0.59)	<u>78.16</u> (0.54)
	GBMLGG C	94.34 (0.20)	<b>95.34</b> (0.70)	93.59 (0.71)	93.47 (0.28)	92.47 (0.41)	92.79 (0.52)
	GBMLGG F	49.68 (0.90)	<u>51.63</u> (1.20)	<b>53.02</b> (1.42)	48.44 (0.95)	47.44 (1.40)	50.32 (1.19)
	LUNG EGFR	64.42 (0.70)	<b>66.17</b> (1.10)	62.45 (1.22)	60.94 (1.12)	61.94 (1.09)	<u>65.14</u> (0.99)
	LUNG KRAS	60.88 (1.20)	<u>61.22</u> (0.50)	<b>62.58</b> (0.47)	58.33 (0.82)	59.33 (0.62)	61.03 (1.04)
	LUNG STK11	67.35 (1.00)	<u>74.31</u> (0.70)	67.83 (0.57)	<u>66.95</u> (0.69)	67.95 (0.79)	<b>75.09</b> (0.72)
DSMIL	LUNG TP53	72.29 (0.30)	<b>75.00</b> (0.50)	<u>72.46</u> (0.46)	69.81 (0.39)	70.81 (0.49)	69.55 (0.49)
	<b>Average</b>	72.49	<b>74.73</b>	72.34	71.79	72.41	<u>73.49</u>
	BCNB ER	88.84 (0.80)	<u>90.93</u> (0.11)	<b>90.52</b> (0.10)	<b>91.91</b> (0.58)	90.91 (0.78)	<u>90.55</u> (0.63)
	BCNB HER2	72.09 (0.50)	<u>73.39</u> (0.10)	70.21 (0.11)	<b>75.60</b> (0.42)	74.60 (0.15)	<u>75.03</u> (0.35)
	BCNB PR	82.96 (0.40)	<u>83.88</u> (0.20)	83.13 (0.23)	<u>84.45</u> (0.27)	83.45 (0.39)	<b>84.68</b> (0.37)
	BRCA ER	<u>87.46</u> (0.30)	<u>86.75</u> (0.50)	85.53 (0.41)	<b>88.05</b> (0.44)	87.05 (0.47)	86.23 (0.47)
	BRCA HER2	60.90 (0.60)	<b>65.94</b> (0.70)	60.38 (0.74)	64.36 (0.71)	63.36 (0.71)	<u>64.76</u> (0.73)
	BRCA PIK3CA	<b>61.30</b> (0.70)	60.96 (0.20)	53.64 (0.21)	<u>60.54</u> (0.56)	59.54 (0.56)	<u>60.57</u> (0.51)
	BRCA PR	78.00 (0.80)	<b>79.05</b> (0.20)	76.26 (0.17)	<u>78.33</u> (0.80)	77.33 (0.63)	<u>75.76</u> (0.21)
	GBMLGG C	<b>94.88</b> (0.40)	<u>94.80</u> (0.47)	89.13 (0.40)	<u>92.76</u> (0.41)	91.76 (0.44)	92.82 (0.45)
DSMIL	GBMLGG F	49.53 (2.40)	<u>50.68</u> (0.70)	51.31 (0.73)	<b>53.84</b> (2.30)	52.84 (1.31)	51.22 (1.56)
	LUNG EGFR	63.93 (1.60)	<b>65.51</b> (1.30)	59.78 (1.32)	63.39 (1.47)	64.39 (1.57)	<u>65.39</u> (1.33)
	LUNG KRAS	<b>59.21</b> (0.40)	58.10 (0.70)	51.82 (0.61)	<u>55.59</u> (0.61)	56.59 (0.65)	<u>59.14</u> (0.57)
	LUNG STK11	65.65 (1.40)	68.61 (0.40)	65.74 (0.37)	<u>71.66</u> (0.55)	<b>72.66</b> (1.29)	70.37 (0.38)
	LUNG TP53	71.31 (0.80)	<b>71.88</b> (0.70)	70.70 (0.74)	67.29 (0.79)	68.29 (0.77)	71.06 (0.78)
	<b>Average</b>	72.00	<u>73.11</u>	69.86	72.91	<b>73.52</b>	72.89

1944  
 1945  
 1946  
 1947  
 1948  
 1949  
 1950  
 1951  
 1952  
 1953  
 1954  
 1955  
 1956  
 1957  
 1958  
 1959  
 1960  
 1961

Table A9: **Performance comparison between pathology-specific MoE methods.** M4 has a distinct MoE-based architecture, while MAMMOTH (+Ours) and PaMoE are added on top of ABMIL. Best performance is shown in **bold**, second best is underlined

		ABMIL Base	ABMIL + Ours	ABMIL + PaMoE	M4 Base
Tissue	BRACS C	67.10 <small>(1.20)</small>	<b>72.70</b> <small>(1.40)</small>	<u>70.52</u> <small>(1.42)</small>	62.27 <small>(1.32)</small>
	BRACS F	42.84 <small>(2.50)</small>	46.12 <small>(2.40)</small>	<u>43.29</u> <small>(2.27)</small>	<u>44.92</u> <small>(2.71)</small>
	EBRAINS C	86.10 <small>(1.10)</small>	<b>89.98</b> <small>(0.70)</small>	<u>89.95</u> <small>(0.62)</small>	86.09 <small>(0.91)</small>
	EBRAINS F	67.20 <small>(1.00)</small>	<b>72.40</b> <small>(1.20)</small>	<u>66.68</u> <small>(1.19)</small>	65.86 <small>(1.34)</small>
	NSCLC	94.68 <small>(0.10)</small>	94.68 <small>(0.10)</small>	94.68 <small>(0.10)</small>	94.54 <small>(0.12)</small>
	PANDA	93.12 <small>(0.20)</small>	<b>94.28</b> <small>(0.20)</small>	91.40 <small>(0.22)</small>	91.48 <small>(0.25)</small>
Average		75.17	<b>78.36</b>	76.09	74.19
Molecular	BCNB ER	90.38 <small>(0.20)</small>	<u>92.25</u> <small>(0.10)</small>	<b>93.04</b> <small>(0.08)</small>	90.23 <small>(3.76)</small>
	BCNB HER2	73.05 <small>(0.40)</small>	<u>74.70</u> <small>(0.40)</small>	72.28 <small>(0.47)</small>	74.48 <small>(3.68)</small>
	BCNB PR	82.48 <small>(0.40)</small>	<b>85.84</b> <small>(0.50)</small>	83.81 <small>(0.54)</small>	83.97 <small>(3.61)</small>
	BRCA ER	86.93 <small>(0.30)</small>	<b>87.94</b> <small>(0.30)</small>	87.71 <small>(0.35)</small>	87.04 <small>(4.66)</small>
	BRCA HER2	64.35 <small>(1.10)</small>	<b>68.35</b> <small>(0.80)</small>	61.11 <small>(0.88)</small>	66.32 <small>(4.27)</small>
	BRCA PIK3CA	60.23 <small>(0.70)</small>	59.55 <small>(0.50)</small>	<u>59.55</u> <small>(0.44)</small>	<b>61.38</b> <small>(2.81)</small>
	BRCA PR	76.37 <small>(0.30)</small>	<u>78.77</u> <small>(0.50)</small>	76.53 <small>(0.57)</small>	78.31 <small>(4.92)</small>
	GBMLGG C	91.82 <small>(0.40)</small>	<b>96.19</b> <small>(0.40)</small>	95.79 <small>(0.46)</small>	92.46 <small>(0.51)</small>
	GBMLGG F	51.89 <small>(1.30)</small>	52.22 <small>(1.70)</small>	<b>54.15</b> <small>(1.59)</small>	<u>53.01</u> <small>(1.88)</small>
	LUNG EGFR	61.27 <small>(1.20)</small>	63.68 <small>(1.20)</small>	<u>67.25</u> <small>(1.37)</small>	<u>65.03</u> <small>(3.36)</small>
	LUNG KRAS	58.06 <small>(0.70)</small>	59.40 <small>(1.50)</small>	<u>59.52</u> <small>(1.60)</small>	59.24 <small>(3.61)</small>
	LUNG STK11	76.41 <small>(1.10)</small>	74.36 <small>(1.50)</small>	<u>75.41</u> <small>(1.65)</small>	74.13 <small>(7.44)</small>
	LUNG TP53	72.43 <small>(1.10)</small>	<b>76.20</b> <small>(0.70)</small>	70.22 <small>(0.61)</small>	73.26 <small>(6.04)</small>
Average		72.74	<b>74.57</b>	73.57	73.76

1984  
 1985  
 1986  
 1987  
 1988  
 1989  
 1990  
 1991  
 1992  
 1993  
 1994  
 1995  
 1996  
 1997